THE MEASUREMENT AND ANALYSIS OF FROST ACCUMULATION ON A FLAT PLATE WITH FORCED CONVECTION

A Thesis

submitted to the College of Graduate Studies and Research

in Partial Fulfilment of the Requirements for

the Degree of

Master of Science

in

the Department of Mechanical Engineering

University of Saskatchewan

by

Yanhui Mao

Saskatoon, Saskatchewan

September 1991

COPYRIGHT

ABSTRACT

Frost fouling of heat exchanger surfaces is a common problem in many industrial, commercial and domestic applications. In this study the frost formation process on a flat plate with forced convection was experimentally investigated. A flat plate heat exchanger test loop was designed, built and tested. Air from the room passed over the cold test plate. Test conditions were limited to a test surface temperature range from -15 to -5 ^{o}C, air humidity ratio range from 0.004 to 0.01 kg/kg, supply air temperature range from 15 to 23 ^{o}C, and inlet airflow Reynolds number range from 3000 to 7000 (i.e. air velocity from 1.15 to 2.67 m/s).

An innovative new method, using a laser-beam and light-meter for the measurement of frost thickness, was designed and calibrated with an accuracy of 0.025 mm. Also, a newly designed method of measuring the local frost mass concentration (mass per unit area) was developed and tested. A calibrated heat-flux meter was used to measure the local heat flux along the test plate.

Typical frost thickness, mass concentration and heat flux data are presented as a function of distance from the leading edge, humidity ratio of the inlet air, test surface temperature, inlet velocity (or Reynolds number), and time. Frost property data from more than 50 test runs are correlated against the five independent test variables using dimensionless variables. The coefficients of tolerance range from 0.91 to 0.96 for the independent variables over the range of test conditions. These data and correlations are discussed and compared with other available data in the literature.

ACKNOWLEDGEMENTS

The author expresses her appreciation and sincere gratitude to her supervisor, Professor R.W. Besant who gave freely of his time and expertise to guide the author through an academically profitable Master's program, and who provided much advice and impetus for this project. The author also thanks her co-supervisor, Dr. K.S. Rezkallah for his helpful comments to correct this thesis.

The acknowledgement is extended to Mr. D. Deutscher. His valuable suggestions and ideas on designing and mounting the experimental apparatus and instrumentation helped immensely. The author also like to thank Mr. J. Falk for his assistance with the laser optics and Dr. Y-X. Tao for his assistance with the heat-flux meter calibration.

The author is thankful the personal financial support provided by NSERC grants to Professor R.W. Besant during her graduate program.

Special thanks are given to the author's all the family members in China for their continuous support and encouragement, especially the author's parents who gave so much moral support.

This thesis is dedicated to the author's grandfather and grandmother, Qingqi Mao and Fengying Du.

Table of Contents

List of Figures

List of Tables

List of Symbols

a_1, a_2 Empirical constants

c_p Specific heat at constant pressure (J/kg K)

D_{AB} Binary diffusion coefficient for water vapor in air at the film temperature (m^2/s)

D_h Hydraulic diameter at inlet of the test section, D_h=0.0375 m.

F_o Fourier number, $F_o=\frac{\alpha_a \cdot t}{(D_h)^2}$

h Heat transfer coefficient ($W/m^2 \cdot K$)

h_a Heat transfer coefficient of air ($W/m^2 \cdot K$), $h_a=Nu_x \frac{k_a}{X}$

h_f Heat transfer coefficient under frost formation condition, defined by $h_f=\frac{1}{R_{sum}-R_f}$ ($W/m^2 \cdot K$)

h_{fa} Heat transfer coefficient with frosting ($W/m^2 \cdot K$)

h_m Mass transfer coefficient (m/s)

h_{mf} Mass transfer coefficient with frost formation, defined by $h_{mf}=\frac{\dot{m}_f}{\Delta W}$ ($kg/m^2 \cdot K$)

h_{sg} Latent heat of sublimation for water vapor from gas to solid (J/kg)

k Thermal conductivity ($W/m \cdot K$), $k=\alpha \rho c_p$

k_a Thermal conductivity of air at the film temperature ($W/m \cdot K$)

k_{eff} The effective frost thermal conductivity ($W/m \cdot K$)

k_f Frost thermal conductivity ($W/m \cdot K$)

$\frac{k_f}{k_i}$ Dimensionless frost thermal conductivity

k_i Thermal conductivity of ice, 1.88 ($W/m \cdot K$) at 0^oC

L Characteristic length (i.e. the length of a flat plate), (m)

Le Lewis number, $Le=\frac{\alpha}{D_{AB}}=\frac{Pr}{Sc}$

M Mass of frost (gm)

ΔM Measurement uncertainty of frost mass (gm)

m_f Frost mass concentration (kg/m^2)

Δm_f Measurement uncertainty of frost mass concentration (kg/m^2)

$\dot{m}_f$ The time rate of change of frost mass concentration ($kg/m^2 \cdot s$)

Nu Nusselt number, $Nu=\frac{hL}{k}$

Nu_f Local Nusselt number under frost formation condition, $Nu_f=\frac{h_f X}{k_a}$

Nu_{fa} Apparent Nusselt number with frosting

Nu_{fo} Overall frost Nusselt number

Pr Prandtl number, $Pr=\frac{\nu}{\alpha}$

q'' Total heat flux (W/m^2)

q''_f The total heat flux through the frost layer (W/m^2)

q''_{fa} Heat flux from air to frost (W/m^2)

R Radius of disk (16 mm).

ΔR Measurement uncertainty of frost sample radius on disk (mm)

R_{ed} Inlet Reynolds number based on the hydraulic diameter, $R_{ed}=\frac{V_a \cdot D_h}{\nu_a}$

R_f Frost thermal resistance, defined by $R_f=\frac{\delta_f}{k_f}$ ($m^2 \cdot K/w$)

R_{sum} Total heat transfer thermal resistance, defined by $R_{sum}=\frac{T_a-T_{ts}}{q''}$ ($m^2 \cdot K/w$)

S Thermal conductance of polyethylene sheet ($W/m^2 \cdot K$)

Sc Mass transfer Schmidt number, $Sc=\frac{\nu}{D_{AB}}$

Sh Sherwood number, $Sh=\frac{h_m L}{D_{AB}}$

Sh_f Sherwood number with frost formation, defined by $Sh_f=\frac{h_{mf} X}{D_{AB}}$

St_m Mass transfer Stanton number, $St_m=\frac{Sh}{ReSc}$

St Heat transfer Stanton number, $St=\frac{Nu}{RePr}$

T Average temperature at the top and bottom surface of polyethylene sheet (^oC)

t Time (s)

T_a Air temperature at the test section inlet (^oC)

T^* Dimensionless temperature, $T^*=\frac{T_{tp}-T_{ts}}{T_a-T_{ts}}$

T_{tp} Triple point temperature, 0 ^oC

T_{ts} Local test surface temperature (^oC) (For a given test, this temperature varies with distance from leading edge.)

V_a Air velocity at the test section inlet (m/s)

W Air humidity ratio at the test section inlet (kg/kg)

ΔW The humidity ratio difference between the inlet air and the saturated air at 0^oC (kg/kg) (i.e. on the surface of the frost)

X^* Dimensionless position, $X^*=\frac{x}{D_h}$

x Distance from the leading edge of test plate (m)

α	Thermal diffusivity (m^2/s)
α_a	Thermal diffusivity of air, at the film temperature (m^2/s)
δ_f	Frost thickness (mm) or (m) in correlations
$\Delta\delta_f$	Measurement uncertainty of frost thickness (mm)
$\frac{\delta_f}{\delta_i}$	Dimensionless frost thickness
δ_i	Ice thickness, $\delta_i=\frac{m_f}{\rho_i}$ (m)
ε_a	Volume fraction of air in frost, $\varepsilon_a=1-\varepsilon_i$
ε_i	Average volume fraction of ice in the frost layer, $\varepsilon_i=\frac{\rho_f}{\rho_i}$
ν	Kinematic viscosity (m^2/s)
ν_a	Kinematic viscosity of air, at the film temperature (m^2/s)
ρ	Mass density (kg/m^3)
ρ_f	Frost density (kg/m^3)
$\Delta\rho_f$	Measurement uncertainty of frost density (kg/m^3)
$\frac{\rho_f}{\rho_i}$	Dimensionless frost density or volume fraction of ice crystals
ρ_i	Ice density, 920 (kg/m^3) at 0°C

Chapter 1

INTRODUCTION

1.1. Introduction

When warm, moist air passes over a surface at a temperature less than 0 °C, some of its water vapor content will be deposited on the surface in the form of water, ice or, a porous structure of ice crystals. The latter deposition process is known as frost formation.

Frost often accumulates on cold heat exchanger surfaces in refrigerators, air conditioners, heat recovery systems for ventilation air and ambient-air-source heat pumps. For example, in food storage systems, perishable food is stored in refrigerated spaces where warm humid air, due to door openings, is brought in contact with heat exchanger surfaces at -10 to -20 °C. Air conditioners for space cooling in buildings experience similar problems in cooling warm indoor air at high relative humidities using cold heat exchanger surfaces. Heat exchangers are also used in heat recovery systems using exhaust air from buildings to warm the incoming cold supply air during cold winter days. Frost often occurs on ambient-air-source heat pumps. Such devices are sometimes used to heat indoor spaces during cold weather conditions. As long as the temperature is well below 0 °C, frost on these various heat transfer surfaces will continue to grow. This frost accumulation will adversely affect the performance of each of these systems.

The accumulation of frost on heat exchanger surfaces affects the thermal performance of heat exchangers in a variety of ways; examples are:

1. **Decreasing the airflow rate through narrow heat exchanger passages:** The resistance to airflow increases with increasing frost layer thicknesses in narrow heat exchanger passages, resulting in an increase in the air pressure drop. Using a fixed blade fan, the airflow rate through the heat exchanger will decrease with increasing frost growth.

2. **Decreasing the cooling capacity of a system due to fouling of heat exchanger surface:** A thick layer of frost on a heat exchanger surface acts as a thermal insulator, reducing the heat transfer rate for a given temperature difference and airflow rate. As a result, there will be a decline of the overall heat transfer coefficient for the cooling surface. Often the cooling capacity for the heat exchanger will decrease with increasing frost thickness.

3. **The need for a defrost cycle:** Frost accumulation must be removed to insure continuous satisfactory performance of heat exchanger surfaces. During a defrost cycle, the cooling equipment undergoes a discontinuous operation in which additional heat is supplied in the loop. A test result [Niederer (1976)], shown on Figure 1.1, indicates that the total energy input for defrosting a coil could be as high as 26713 kJ, with 4126 kJ being carried out of the room with the condensate. That is, only 15% to 20% of the total defrosting heat actually appears in the condensate. The rest of the defrosting heat input appears as temperature increases in the air surrounding the unit and the metal of the coil and cabinet of the air cooler.

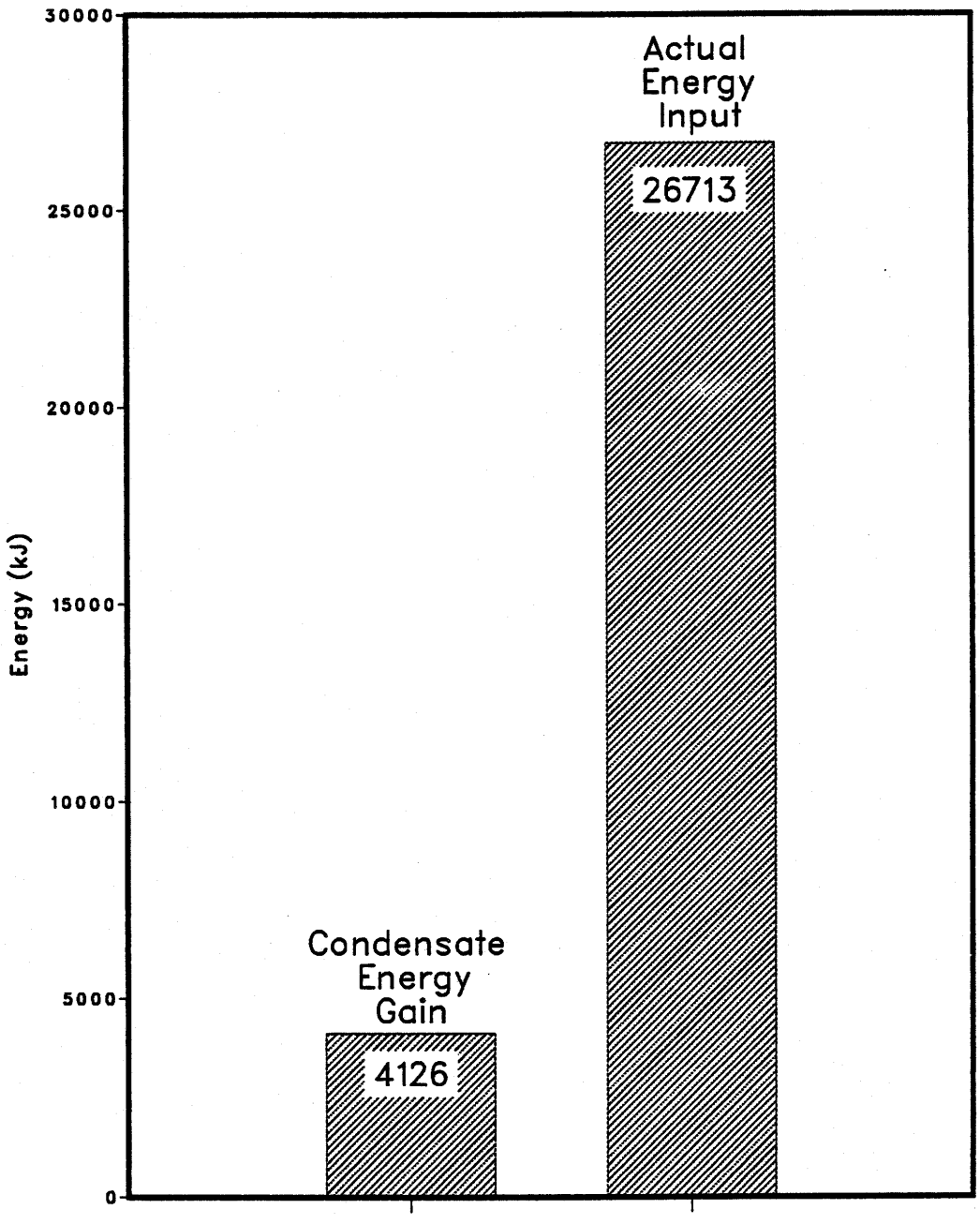

Figure 1.1 Energy required for defrosting cycle in a typical heat-exchanger coil (Niederer,1976)

> It has been estimated that reliability and performance considerations due to frost accumulation make it necessary to oversize the capacity of refrigeration equipment by about 50% while the average performance is only 75% of the same system with no frost accumulation.

Some researchers have considered frost formation to be a problem with a moving boundary or interface with both heat and mass transfer processes occur between the air stream and the deposit interface. It cannot be treated readily as a growth of a uniform material such as ice because frost layers are comprised of air trapped in a porous matrix of ice crystals. Heat is transferred to the cooled frost-air interface by convection where it is conducted through the frost layer to the cold heat exchanger surface. Concurrently sublimation, or the phase change of water from a vapour to ice crystals, occurs within the frost layer as well as at the frost-air interface. This phase change releases the latent heat of sublimation which is also conducted through the frost layer to the cold heat exchanger surface. The air in the boundary layer is cooled by convection to the frost-air interface and dehumidified by diffusion of water vapour across the frost-air interface. In general, air velocity, dry-bulb temperature and other air properties will influence the convective heat transfer. The phase change heat transfer depends on the air moisture content, air velocity, test surface temperature and the ability of the water vapour to diffuse through the boundary layer and the frost layer to the cold wall. There are a variety of frost densities that may form on a cold surface from light and fluffy to very dense, like ice. The type of frost formed on a cold surface depends on the history of the air flow and its temperature and psychrometric properties. Also radiant heat transfer, and distance from the leading edge in a boundary layer can change the frost growth. In addition, surface finish, type of material on the surface, existence of liquids on the surface, and airflow turbulence can influence the frost accumulation.

The initial formation of frost is a complicated transient process. Simple microscopic observations provide us an understanding of frost accumulation. When a cold surface is first exposed to warm moist air, small scattered liquid droplets form at nucleation sites and randomly adhere to the substrate by molecular forces similar to adsorption of water vapour on a surface. These water droplets are cooled by heat conduction to the cold surface and often supercooled below the freezing point of water. They all, within a short time, change phase to ice clumps. As time progresses, these clumps provide sites for the growth of ice columns normal to the surface. Tokura et al. (1983) referred to this initial phase of frost column growth as a one dimensional frost growth period. At a transition time, these microscopic ice columns start to accumulate ice crystals on their sides which further blocks the flow of air through the ice columns. If the surface is very rough, the mechanical interlocking of ice crystals with the rough surface may add to the strength of the bond when the frost layer is subjected to a shear force. At the transition time between the ice column and the frost layer growth, typically 5 minutes after starting the frosting process, the frost resembles a forest of trees without branches [Hayashi et al. (1977)]. Next, the tops of the ice columns change their shape by the generation of ice crystal branches around the top of the columns. A meshed and more uniform surface then forms, until the frost surface is nearly flat. The ice crystal canopy at the top of the ice columns impedes the flow of air through the ice columns so that the water vapour is transferred by mass diffusion into the frost layer where it adds to the ice crystals in the frost layer. Tokura et al. (1983) referred to this second period of frost growth as a three dimensional frost growth period. During this period, which may start after a few minutes and last several hours, the frost layer grows and increases in internal density while the frost-air interface temperature gradually increases towards 0 ^{o}C. This frost layer retains its structure and continues to grow until the increasing frost thermal resistance permits the

frost-air interface temperature to attain 0 °C. At this time, or third period of frost growth, the frost surface may, with slight fluctuations in the air or surface temperature, begin to melt with the liquid soaking into the pores of the frost layer and freezing onto the ice layer. This melting at the frost-air interface and freezing process causes a further increase in the frost layer density and a decrease in its thermal resistance. As the frost-air interface temperature randomly, both temporally and spatially, rises above the ice triple point, the transferred vapour deposits become liquid water at the interface and is drawn into the colder frost layer by surface tension which increases with decreasing temperature. This water, exposed to sub-zero temperature, again forms more ice crystals inside the frost layer. Successive melting and frost depositions will continue until the frost layer has within it a solid sheet of ice lense and is unable to incorporate more melt. This last period of frost growth might by referred to as the 0 °C frost-air interface temperature frost growth period, a period characterized by increasing frost density and the eventual formation of large ice lenses in the frost layer, usually near the frost-air interface. Beyond this time the ice layer in the frost continues to grow.

1.2. Objectives

The literature on frost growth over the past 50 years is primarily concerned with the second, or three dimensional, period of frost growth since this is the typical operation condition of most heat exchangers undergoing frosting. Researchers have reported data and some empirical correlations for average thickness, density and thermal conductivity (see Chapter 2). Local values of these properties, however, are sparse or not available within the boundary layer of the air flow. Some of the existing correlations for frost properties use non-standard dimensional parameters while dimensionless parameters

might better characterize the physical phenomenon. Some of the experimental data were not collected under well controlled testing conditions so the results from one research group occasionally disagreed with those of other groups. Various research groups selected ranges of operating conditions typical of particular applications such as refrigerators or heat pumps. Very little data has been collected under conditions that might be typical of ventilation air heat recovery systems operating during cold weather. Finally the accuracy of the experimental data, due to instrumentation and experimental techniques used, often has been less than satisfactory.

It is the purpose of this study of frost growth on cold surfaces with adjacent air flow to overcome such shortcomings. The objectives of this study are:

1. To devise new and more accurate techniques to measure the frost thickness, mass concentration (mass per unit area), and heat flux at several locations of a cooled flat plate subjected to warm moist airflow.

2. To monitor and measure local frost thickness, mass concentration and heat flux with time over a range of operating conditions for the cold plate temperature, inlet air temperature, humidity ratio, and air speed or Reynolds number under turbulent flow conditions.

3. To correlate the collected data using general dimensionless groups for frost thickness, density, and apparent thermal conductivity, apparent Nusselt number, and apparent Sherwood number as a function of the independent non-dimensional parameters.

In order to meet these objectives a test apparatus was designed, constructed, and

instrumented to measure the frost thickness, mass concentration and heat transfer rates over a wide range of flow condition. A detailed description of this test apparatus is presented in Chapter 3.

A new frost thickness measurement system was designed, assembled and calibrated using a low power laser beam and a sensitive light meter; this method is described in more detail in Chapter 4.

Also, in Chapter 4, a new method of measuring local mass concentration of frost was developed and tested. This method employs the use of fourteen thin small disks, which are thermally bonded to the cold plate to collect the frost samples.

Chapter 5 presents the experimental procedure used to collect a range of experimental data and the procedure used to reduce these data to some general correlations. The accuracy of these correlations is also discussed.

In Chapters 6 and 7 the correlations developed are compared with those available in literature. Finally, the achievements and findings of this study are summarized and additional studies that need to be done are suggested.

Chapter 2

LITERATURE REVIEW

2.1. Introduction

Many studies have been carried out over the past 50 years to better understand the frosting process. Most of the research papers have been concerned with the overall frost layer averaged over a large surface and the effects of different ambient air conditions. Cremers and Mehra (1982) reviewed the literature of frost growth under free convection conditions. O'Neal and Tree (1985) reviewed the literature on frost growth under forced convection conditions. More recently, Padki et al. (1989) listed 109 papers, reports and theses that have been written on frost since 1933. In this thesis, the more recent literature was reviewed, especially frost growing under forced convection. A number of attempts have been made to explain the physical phenomena of frost growth and to formulate mathematical models to describe the process of frost accumulation. The more recent literature on heat and mass transfer with frost formation on a surface are summrized in Table 2.1. In this table, the surface geometry, experimental conditions and measured frost properties are given. All but three of these studies were for forced convection.

Table 2.1 A Summary of Selected Frost Growth Literature

First Author	Date	Geom.	Air	T_w (°C)	T_a (°C)	$W \times 10^3$ (kg/kg)	V_a (m/s)	δ_f (mm)	ρ_f (kg/m^3)
Abdel-wahed	1984	F.P.	F.C.	-18	14 to 18	5.6 to 7.6	3.5 to 6	2 to 10	N/A
Beatty	1951	A.	F.C.	-12 to -7	14 to 24	4 to 12	3.8 to 18.5	0.5 to 6.6	N/A
Biguria	1970	F.P.	F.C.	-99.5 to -29	25.5 to 31.5	5 to 13.6	2.7 to 12	0.5 to 3	20 to 70
Brian	1970	P.P.	F.C.	-24 to -9.4	1 to 34	3 to 3.4	2.6 to 11	1.8 to 8.9	67 to 90
Chung	1958	C.	F.C.	-23 to -12	15 to 21	4 to 8	1.4 to 5.6	3.81	200 to 500
Cremers	1982	C.	N.C.	-20	24	6.6 to 17.8	N/A	2 to 15	N/A
Hayashi	1977	F.P.	F.C.	-25 to 0	15 to 30	4.5 to 10	1 to 6	N/A	40 to 520
Hosoda	1967	F.P.	F.C.	-23 to -13	0 to 2	4.7 to 5.8	0.5 to 5	0.5 to 5	200 to 500
Jones	1975	F.P.	F.C.	-34 to -15	23	6 to 14.1	1.26 to 7.62	0.5 to 5	N/A
Kamei	1952	A.	F.C.	-30 to -24	7	5.5 to 5.9	2.7 to 14.6	1 to 4	20 to 170
Loper	1960	C.	F.C.	-183	27.8	11 to 17.6	2.5 to 7.5	8	N/A
O'Neal	1984	P.P.	F.C.	-12 to -5	5 to 12	3.8 to 5.1	2.2 to 16.4	0.5 to 4	200 to 430
Sanders	1974	C.	F.C.	-20 to -15	-10 to -1	2.2 to 2.8	3 to 8	0.5 to 3	N/A
Schneider	1978	C.	F.C.	-30 to 5	5 to 15	5 to 15	1.2 to 10	2 to 10	N/A

Continued

Table 2.1 A Selected Summary of Frost Growth Literature (Continued)

First Author	Date	Geom.	Air	T_w (°C)	T_a (°C)	$W \times 10^3$ (kg/kg)	V_a (m/s)	δ_f (mm)	ρ_f (kg/m^3)
Schulte	1982	F.P.	F.C.	-30.6	-18 to 29	10.2 to 24	1 to 5.1	2.4 to 5.8	N/A
Stoecker	1960	A.	N.C.	-26.7	-13.9	0.85	N/A	24.1	184 to 320
Thigpen	1964	F.P.	F.C.	-54 to -5	18 to 34	2.3 to 19.9	1.5 to 12	0.3 to 6.1	24 to 344
Tokura	1988	F.P.	F.C.	-16 to -11	20	6.8 to 9.6	2 to 4	0.4 to 4	N/A
Wijeysundera	1984	C.	N.C.	-13.6 to -12.6	19.8 to 21.3	9.4 to 12.6	N/A	5	80 to 220
Yamakawa	1972	P.P.	F.C.	-20	11	4.9 to 8.5	1.6 to 7.3	1 to 4	100 to 420
Yonko	1967	F.P.	F.C.	-28 to -5	21 to 23	7.5 to 16.1	1.3 to 5.25	5.1	N/A

Geom.= Geometry of heat exchanger

T_w = Wall temperature

T_a = Air temperature

W = Humidity ratio

V_a = Air velocity

δ_f = Frost thickness

ρ_f = Frost density

F.P. = Flat Plate

P.P. = Parallel Plates

A. = Annulus

C. = Cylinder

F.C. = Forced Air Convection

N.C. = Natural Air Convection

N/A = Not Available

2.2. Frost Growth Background

The major variables affecting frost growth on a heat exchanger surface appear to be the psychrometric conditions of the air, the cold surface temperature, the distance from the upsteam, and the air velocity (or inlet Reynolds number).

Many of the previous studies reported an increase in the frost thickness due to a decrease in the surface temperature of the heat exchanger. There was also similar agreement with regard to the effect of air humidity on the frost growth; as the air humidity increased the frost thickness increased.

The frost growth results and the literature data were not always in agreement on the effect of air velocity. Tokura et al.(1988), Schneider (1978), Trammel et al.(1968), and Yonko et al.(1967) found that the air velocity has no significant influence on the frost growth rate. On the other hand, the data of Adbel-wahed et al.(1984), Sanders et al.(1974), Yamakawa et al.(1972), Brian et al.(1970), and Hosoda et al.(1967) suggested that frost growth was dependent on the air velocity. Careful examination of the data, however, shows that after a certain start up time period, the slower growth rates are associated with higher air velocities [Sanders et al.(1974)]. Also, O'Neal et al.(1984) reported that "The results here seem to indicate that above some critical Reynolds number, frost growth is independent of Reynolds number. Below that critical Reynolds number, frost growth increases with increasing Reynolds number.", and they found that the critical Reynolds number was 15900 in the range of Reynolds number from 4400 to 32400 on a vertical plate in a parallel flow geometry. Their conclusion is not in agreement with other data (e.g. Abdel-wahed et al. 1984). The latter took their data in the range of Reynolds number from 30000 to 140000 for air flowing over a horizontal plate.

Experimental data for the effect of air temperature on the frost growth rate were reported by Sanders et al.(1974). They found that increasing the air temperature from -10 ^{o}C to -1 ^{o}C resulted in a decrease in the frost growth rate by 50% at the end of 3 hours for air flow over a cylinder geometry. For a plate, O'Neal et al. (1984) concluded that there was no difference in frost thickness at the end of 3 hours for air temperature increasing from 7.4 ^{o}C to 11.9 ^{o}C. Unfortunately, the literature does not include any other data on the influence of changing the air temperature on the frost growth rate over a wide range of air temperatures.

Another potential factor influencing the frost growth is the location on the heat exchanger surface. For a flat plate and air velocity in the range of 2 to 4 m/s, Tokura et al.(1988) found that "no significant difference in the thickness of frost could be recognized as depending on the distance measured from the leading edge of the plate." Using a similar geometry and the same air velocity, Hayashi et al.(1977) reported that "the frost layer grows faster in the upstream than the downstream of the plate even for the same conditions and each period appears gradually from the front to the rear of the plate. This means that the time required for each period varies not only with the frost formation conditions but also with the frost deposit positions." O'Neal et al.(1984) reported also similar trends. Their conclusion was that "For Reynolds number below 10000, the frost grew faster toward the front of the plate than toward the rear. However, at higher Reynolds numbers, the frost was nearly independent of position." Thus, there appears to be some dependency of frost thickness as a function of distance from the leading edge, but no investigators have adequately quantified these results.

Several investigators have attempted to model the frost growth process. For the

case of natural convection on vertical cylinders, Cremers et al.(1982) showed the best fit of their data was given by a dimensional equation,

$$\delta_f = 0.2t(T_f - T_w)^{0.4} \tag{2.1}$$

where:

δ_f Frost thickness (mm)
T_f Frost surface temperature (K)
T_w Wall temperature (K)
t Time (min.)

This simple model correlated well for relative humidities higher than 65% and t>60 minutes.

For forced convection on a cylinder, Schneider (1978) developed the following non-dimensional correlation:

$$\delta_f = 0.465\left[\frac{k_i}{\Delta h_i \rho_i} t(T_f - T_w)\right]^{0.5}\left(\frac{\tau}{1h}\right)^{-0.03}\left(\frac{T_f - T_w}{1K}\right)^{-0.01}\pi^{0.25}F_t \tag{2.2}$$

where:

k_i Thermal conductivity of water-ice (kW/m K)
Δh_i Specific latent heat of sublimation of water-ice (kJ/kg)
ρ_i Density of water-ice (kg/m^3)
τ Time (hr)
π Correction term from air supersaturation, $\pi = \frac{p - p'_f}{p' - p'_f}$
p Partial vapor pressure of the air
p'_f Partial pressure of saturated vapor at frost surface temperature
p' Partial vapor pressure of saturated air
F_t Empirical correction term for air temperature, $F_t = 1 + 0.025\frac{T_a - T_m}{T_m - T_w}$
T_a Air temperature (K)
T_m Melting point temperature of water-ice (273 K)

This equation satisfied the measured values with a maximum error of ±10% in the

range of $1<\tau<8$ hr. This agrees with the observations of Biguria et al.(1970) who studied frost on a flat plate.

The correlations reported by O'Neal et al.(1985) for frost growth were developed for a parallel plate geometry. For low Reynolds number (below 15900), the best fit to their data was given by :

$$\delta_f=0.015Re^{0.393}t^{0.663}(T_o-T_p)^{0.705}(W_a-W_o)^{0.098} \tag{2.3}$$

where:

Re	Reynolds number
T_o	Freezing temperature of water (K)
T_p	Plate temperature (K)
W_o	Humidity of saturated air at 0 ^oC (kg/kg)
W_a	Inlet air humidity ratio (kg/kg)

For Reynolds number greater than 15900 in a parallel flow geometry, the correlation for frost thickness was given as:

$$\delta_f=0.712t^{0.582}(T_o-T_p)^{0.705}(W_a-W_o)^{0.098} \tag{2.4}$$

2.3. Frost Density and Thermal Conductivity

Two important properties for heat transfer and frost growth calculations are the frost density and thermal conductivity.

2.3.1. Frost Density

The frost density of a frost layer in a heat exchanger varies with time, air velocity, cooling surface temperature and local deposit position within the boundary layer.

An increase in the frost density with time was reported by many investigators, such as Yamakawa et al. (1952), Sanders (1974), Jones et al. (1975) and O'Neal et al. (1984). Also Hayashi et al. (1977) reported that "the increase in frost density is approximately parabolic with time", however, Tokura et al. (1983) indicated that "the density of the entire frost layer is high and nearly constant for a long period of time".

Frost density increases with air velocity [Schneider (1972) and O'Neal et al. (1984)], and decreases with decreasing the cooling surface temperature [Tokura et al. (1988)]. Hosoda et al. (1967) presented an empirical equation for frost density, given by:

$$\rho_f = 340|T_p|^{-0.445} + 85V_a \tag{2.5}$$

where:

ρ_f Frost density (kg/m^3)
$|T_p|$ Absolute value of cooling surface temperature (^{o}C)
V_a Air velocity (m/s)

Frost density varies with position on the heat exchanger surface, as Cremers et al. (1978) pointed out "any analytical treatment of it must recognize that density is a function of space as well as time". An interesting result that was observed by O'Neal et al. (1984) is "the frost density was also a function of position on the plate. The front half of the plate yielded denser frost than the rear half". Also, Biguria et al. (1970) measured the local frost density at 25.4, 101.6 and 203.2 mm from the leading edge of a plate 635 mm long. An empirical correlation was obtained based on their study; this is given by:

$$\begin{aligned} ln(\rho_f) = & -11.952096 + 0.024217706 T_p + 35.5498949 W_a \\ & -0.03553795 V_a + 1.2062987 \times 10^{-4} T_p V_a \\ & -0.038382644 BL + 13.160559 \tau_{fs} \\ & -0.021328733 T_p \tau_{fs} - 81.955 W_a \tau_{fs} \\ & + lnf(x) \end{aligned} \tag{2.6}$$

where:

$\ln(\rho_f)$	Natural logarithm of frost density (lb/ft^3)
T_p	Plate average temperature (^oF)
W_a	Humidity of air (lb H_2O/lb dry air)
V_a	Air velocity (ft/s)
BL	Boundary layer tripped or untripped, +1 or -1.
τ_{fs}	Dimensionless temperature parameter, $\tau_{fs} = \frac{T_s - T_p}{T_m - T_p}$
T_s	Frost surface temperature at frost-air interface (^oF)
T_m	Melting point temperature of water (^oF)
x	Distance from leading edge of cold plate (inches)
	Laminar flow $f(x) = x^{-0.270}$, Turbulent flow $f(x) = x^{-0.073}$.
x_o	Length from leading edge of cold plate(inches)

As seen from the above equation, the Biguria correlation for frost density includes many of the parameters influencing the frost density but there is no time dependency in Eq. (2.6).

2.3.2. Frost Thermal Conductivity

Many investigators reported the higher the air velocity and humidity, the greater the frost thermal conductivity. Yonko et al. (1967) showed that the frost thermal conductivity increased as the cooling surface temperature decreased. Another factor influencing the frost thermal conductivity is "the eddy generated by the roughness of frost surface". As Hayashi et al. (1977) indicated "the eddy due to the roughness of frost surface makes the thermal conductivity apparently increase".

Similar to the frost density, Biguria et al. (1970) obtained an empirical correlation for the frost thermal conductivity, this is given by:

$$k_f = -0.23376438 + 1.0342876\times10^{-4}(T_p)^{1.3} + 18.007637W_a + 3.5719847\times10^{-4}V_a + 6.2047771\times10^{-4}t - 8.9475394\times10^{-5}t^2 + 1.0182528\times10^{-7}t^3 + 2.6084586\times10^{-8}t^4 - 4.2023418W_aT_p + 0.11349924tW_a + 1.0859212\times10^{-2}BL + 2.1232614\times10^{-5}V_at - 2.6856724\times10^{-5}BLT_p \quad (2.7)$$

where: k_f is the average frost thermal conductivity (Btu/hr ft ^oF) and t is time (minutes). All other variables were defined in Eq. (2.6).

2.3.3. The Relationship Between Frost Density and Thermal Conductivity

From the above equations, it can be seen that both frost density and thermal conductivity include similar parameters. Therefore, a change in one frost property implies a change in the other. A number of studies reported the relationship between the frost density and the frost thermal conductivity. Despite the fact that the correlations differed slightly, all showed the same trend, as density increased, there was a corresponding increase in the thermal conductivity.

Yonko et al. (1967) compared their results with the literature correlations for frost thermal conductivity, k_f, and density, ρ_f. Their results showed the same trend as mentioned above, but there was a considerable variation in the values of k_f for a given value of ρ_f. They concluded that k_f was a function of more than ρ_f. Based on an experimental investigation, they obtained the following empirical correlation relating k_f to ρ_f:

$$k_f = 0.014 + 0.00668\rho_f + 0.00175(\rho_f)^2 \quad (2.8)$$

Where ρ_f was in lb/ft^3 and k_f was in Btu/(hr tf ^oF). Eq. (2.8) was applicable for wall temperature in the range -10 to -30 ^oC and air temperature from 20 to 25 ^oC.

Sanders (1974) measured ρ_f and k_f for frost forming on a flat plate. The range of operating conditions for that experiment was: wall temperature from -22 to +11 ^oC, air temperature from -10 to 0 ^oC, and air velocity from 4 to 9 m/s. The data was reported in a graphical form. A curve that fits his data was given by:

$$k_f=1.202\times10^{-3}(\rho_f)^{0.963} \tag{2.9}$$

Where ρ_f was in kg/m^3 and k_f was in W/m K. The maximum limit of applicability for ρ_f in Eq. (2.9) was 500 kg/m^3.

In a study of frost formation for temperature ranging from -137 to -7 ^oC, Brian et al. (1969) correlated k_f as a function of both ρ_f and average frost temperature, $\overline{T}_f$. For $\overline{T}_f$ above -18 ^oC. Their correlation was:

$$k_f=8.49\times10^{-17}(\overline{T}_f)^{5.44}+6.86\times10^{-14}(\rho_f)^{-0.025}(\overline{T}_f)^{4.84} \tag{2.10}$$

Where $\overline{T}_f$ is in ^oR, ρ_f in lb/ft^3, and k_f in Btu/(hr ft ^oR). Eq. (2.10) was developed from data for densities from 25 to 130 kg/m^3. This correlation should not be expected to yield accurate results outside of this range. The small density range severely restricted its applicability. For a model of frost growth, Eq. (2.10) could only be applied during the early stages of frost growth.

Marinyuk (1980) correlated k_f with ρ_f, frost surface temperature, T_s, and plate temperature, T_p, in the following expression:

$$k_f=1.3(T_s-T_p)(0.156e^{0.0137T_s}-e^{0.0137T_p}) +5.59\times10^{-5}\rho_f(e^{0.0214T_s}-e^{0.0214T_p}) \quad (2.11)$$

Where k_f is in W/m K, ρ_f in kg/m^3 and T_p and T_s in K. Eq. (2.11) was limited to frost densities up to 300 kg/m^3.

The general rule for the relationships between the thermal conductivity and density appears to be, exercise a great deal of caution when using them. If these data are to be used for air or plate temperatures outside the experimental range then it is quite possible that the actual values will vary widely from those reported here. Equations (2.10) and (2.11) should be used with extreme caution for the temperature ranges usually encountered in heat pumps or normal freezing applications (above -15 °C). The data used to develop these equations were taken at very low temperatures and are probably valid only at densities less than 300 kg/m^3.

2.4. Techniques for Measuring Frost Thickness, Density and Mass Concentration

2.4.1. Frost Thickness

The physical nature of frost deposits on a surface makes the measurement of frost thickness inherently difficult. The frost layer is often rough due to its crystalline structure, fragile under very small mechanical forces in the outer region, but very tough near the surface, where its density is closer to that of ice, and sensitive to slight changes in temperature and humidity. Frost layers, which may be less than one millimeter or more than several centimeters thick, tend to grow or diminish and almost never stay steady

since slight changes in the surface temperature, radiant heat transfer, air temperature, humidity, and velocity distribution can change the frost growth. Even surface finish, type of material on the surface, liquids on the surface, and airflow turbulence can influence the frost deposition. The physical nature of frost on surfaces makes the calibration of any frost thickness measuring system very difficult if high accuracy is sought. Furthermore, with all the independent variables listed above, repeatability of the experiments is often a problem.

Previous attempts to measure frost thickness are numerous. Mechanical probes, micrometers, and direct observations were used by Beatty et al. (1951), Kamei et al. (1952), Stoecker (1960), Schulte and Howell (1982), O'Neal and Tree (1984), and Sherif et al. (1988). Precisions, which are somewhat dependent on the skill of the experimenter, between 1 mm and 0.13 mm may be realized with these mechanical probes. Thigpen et al. (1964), using light reflected from frosted surfaces, claimed a repeatability of 0.10 mm (0.004 in.) in their measurements of frost thickness. A precision of 0.13 mm (0.005 in.) was reported by Yonko and Sepsy (1967), who used a mechanical probe illuminated by a light which cast a shadow on the frost. Using a narrow slit light beam and a micrometer gauge, Sanders (1974) obtained a precision of 0.05 mm and an estimated inaccuracy of 0.1 mm (0.004 in.) while measuring frost thickness.

2.4.2. Frost Density and Mass Concentration

Frost density, ρ_f, is usually defined as the ratio of frost mass to its volume. The volume is the product of the frost thickness, δ_f, and the area occupied by the frost. Physically, frost density varies with distance normal to the surface in the frost layer, Z, as well as with location on the surface, X and Y, and time, t.

Another property of frost that is presented in the literature has been given various names including the "frost amount" by Senshu et al. (1990), "frost mass" by Tokura et al. (1988), "the quantity of frost accumulated" by Abdel-wahed et al.(1984). The frost mass concentration, m_f, is defined as the frost mass per unit area on the surface measured at some time. These frost characteristics may be averaged over the surface area and, for the density, ρ_f, over the frost thickness. It is these integrated and averaged values that are most frequently reported in the literature.

The method most often reported for measuring frost mass concentration and density, is to weigh the frost scraped off a surface while the frost volume is obtained by multiplying the plate surface area by the average frost height. This method, was used by O'Neal et al. (1984), Yamakawa et al. (1972), and Thibaut Brian et.al (1970) among others. No estimate of density precision was given except for O'Neal who estimated a $\pm 3\%$ uncertainty in density for a thickness of 2.3 mm. In a slightly different method, the total weight of test section of the heat exchanger was measured with and without frost to determine the weight of frost so that the average density of frost could be calculated [Senshu et al. (1990), and Yonko et al. (1967)]. Only Yonko reported an error within ± 6.8 gm (± 0.015 lb) (yielding an uncertainty of about $\pm 4.3\%$).

A radioactive source and a counter tube was used to measure the average mass concentration of frost by Thigpen et al. (1964) and Sanders (1974) (a β-radioactive source). Two radiation sources were used in Sanders' experiments to cover a wider range of the absorption curve of the source. The estimated maximum inaccuracy of the measured average mass concentration was claimed to be 2% only. The frost density versus time were also given by Wijeysundera et al. (1984) and Cremers et al. (1982), for

frost accumulation on a vertical tube in free convection. They measured the frost density at various radial distances by using a Gamma-Ray attenuation technique. In this case, the discrepancy between the Gamma-Ray data and weight measured mass was 22%. Unforturately, these experimental data were not confirmed for a horizontal flat plate under forced convection conditions.

Frost density versus position of a flat plate, 635 mm long, was reported by Biguria et al. (1970). The frost density was measured at 25.4, 101.6, and 203.2 mm (1, 4 and 8 inches) from the leading edge of the plate. The technique used and the accuracy of the density measurement were not mentioned in their report.

Finally, some characteristics of average frost density were discussed and developed by Tokura et al. (1988), Abdel-wahed et al. (1984), and Hayashi et al. (1977) among others, but the methods of measuring frost density were not presented.

2.5. Heat and Mass Transfer

In examining the literature on frost growth, it appears that the frost-to-air heat transfer coefficient, h_f, is the most common calculated variable for the researchers developing a detailed model of frost growth and heat transfer. The h_f is usually defined as the heat flux through the cold surface divided by the temperature difference between the air flowing over the surface and the cold surface.

It should be noted that h_f is not a function of frost thickness only; it is a function of geometry, the frost and air properties and the flow rate of the air flowing through a heat exchanger. As such, the complexity of the problem is apparent.

The results from Gates et al. (1967), who did their tests for a finned tube heat exchanger, showed that, over the tested range at constant velocity, an increase in the humidity ratio causes a decrease in the average h_f. For a constant difference in humidity ratio, an increase in velocity caused an increase in the average h_f. For the same geometry, Kondepudi et al. (1989) showed that conditions which led to increased heat transfer and h_f include higher humidity, higher air temperature and smaller fin spacing. For flat plate geometry, Yamakawa et al. (1972) found out that "h_f in the frosting process does not vary appreciably and shows an almost constant value with time".

When modelling the heat transfer under frosting conditions, many investigators used the Chilton-Colburn analogy. The Chilton-Colburn analogy relates the heat and mass transfer coefficient to each other by the equation:

$$\frac{St_m}{St}=\left(\frac{Pr}{Sc}\right)^{2/3}=Le^{2/3} \tag{2.12}$$

If the heat transfer coefficient can be measured during an experiment, it will be possible to infer the mass transfer coefficient from such measurements or vice versa.

For the turbulent, fully developed internal flow on a smooth surface with the Reynolds number, R_{ed}, larger than 10000, a widely used correlation for the average heat transfer without frost, called the Colburn equation, is (Incropera and Dewitt (1987)):

$$Nu=St\cdot Re\cdot Pr=0.023R_{ed}^{4/5}Pr^{1/3} \tag{2.13}$$

The average heat transfer coefficient for heat flux from air to a frost surface, for the air Reynolds number, R_{ed}, ranging from 11.8×10^4 to 77×10^4 in a flat plate geometry, was given by (Thigpen et al. 1964):

$$Nu=0.036R_{ed}^{4/5}Pr^{1/3} \tag{2.14}$$

For the same geometry, and at Reynolds number ranging from 2.3×10^4 to 11.5×10^4, Hosoda et al. (1967) found the correlation to be:

$$Nu=0.116R_{ed}^{4/5}Pr^{1/3} \tag{2.15}$$

Another correlation presented by O'Neal (1982) and Yamakawa et al. (1972) for the parallel plate geometry is:

$$Nu=0.03R_{ed}^{4/5} \tag{2.16}$$

The above correlation is recommended for Reynolds number, R_{ed}, between 6×10^3 to 50×10^3.

The heat transfer coefficient for turbulent air flow in a concentric annulus, with the inner tube being cooled, can be calculated using the following correlation (Kamei et al. 1952):

$$Nu=0.018R_{ed}^{4/5} \tag{2.17}$$

This correlation has been tested over the Reynolds number, R_{ed}, range from 6.8×10^3 to 37×10^3.

It has been observed that the heat transfer diminishes with time during transient operations, therefore the following expression, developed by O'Neal et al. (1985) for transient heat transfer, could be applicable:

$$Nu_t/Nu_{ss}=1+0.23e^{-(t/\tau_o)} \tag{2.18}$$

where Nu_t and Nu_{ss} are the Nusselt number at time t and steady-state condition, respectively.

Since both heat and mass transfer processes occur simultaneously during frost growth, the heat and mass transfer coefficients are often obtained using the Chilton-Colburn analogy:

$$\frac{h}{h_m}=\rho c_p(\frac{\alpha}{D_{AB}})^{2/3}=\rho c_p Le^{2/3} \tag{2.19}$$

For water vapor, the Lewis number, Le, equal to 1.0 was recommended by Sami et al. (1989). That is, the temperature and concentration profiles will be similar (Holman 1981). Consequently, the mass transfer coefficient is obtained from:

$$h_m=\frac{h}{\rho c_p} \tag{2.20}$$

Therefore, the mass transfer coefficient can be determined with prior knowledge of the heat transfer.

2.6. Summary

Considering the literature currently available, with test conditions summrized in Table 2.1, the following observations can be made:

1. No investigators have adequately quantified frost thickness as a function of distance from the leading edge. No researcher claimed a precision, less than

0.05 mm, for measuring frost thickness. Most techniques used to measure frost thickness employed mechanical probes which touch the frost. In correlating the frost thickness for natural convection a dimensional equation, Eq. (2.1), was given by Cremers et al. (1982), and a dimensionless equation (it was not shown in this literature review) was given by Tokura et al. (1983). In case of forced convection a dimensionless correlation, Eq. (2.2), was given by Schneider (1978), and a dimensional correlation, (2.3), was given by O'Neal et al. (1985).

2. The dimensional correlations of average frost density were reported by Hosoda et al. (1967), Eq. (2.5); Hayashi et al. (1977) (equation was not shown in this review); and Bigura et al. (1970), Eq. (2.6). For this last correlation the density variation with position was presented but the method of measuring local frost density was not reported.

3. A dimensional correlation of average frost thermal conductivity as a function of a number of test variables was given by Biguria et al. (1970), Eq. (2.7). Some researchers found that the frost thermal conductivity is a function of frost density alone, as shown by Eq. (2.8) (Yonko et al. 1967), and Eq. (2.9) (Sanders 1974). Other researchers reported that the frost thermal conductivity is not just a function of density, see Eq. (2.10) (Brian et al. 1969), and Eq. (2.11) (Marinyuk 1980). Therefore, there is some disagreement on the relation between frost thermal conductivity and frost density.

4. The heat transfer Nusselt number with frosting was considered as a function of Reynolds number and Prandlt number or Reynolds number alone in

some reported papers. Some authers used the relationship between heat and mass transfer with frosting through the Chilton-Colburn analogy.

Chapter 3

EXPERIMENTAL APPARATUS

3.1. Design Consideration

A common heat exchanger available on the market is the plate-finned heat-exchanger coil, in which air flows past the fins while refrigerant or aqueous glycol flows through the coil. Typically, thin aluminium fins comprise 85% to 95% of the heat exchanger surface area on the air side. The fins are oriented parallel with each other and perpendicular to the coil tubes carrying the refrigerant. Often warm moist air is forced, using fans, through the parallel passages formed by fins to warm up a cold refrigerant. Because a flat plate geometry is similar to that found in plate finned heat exchangers, it was the geometry used in the experimental apparatus.

In this study, the velocity, temperature and humidity ranges of the air stream travelling through the heat exchanger and the plate temperature were chosen to include some of the range of these variables found in commercially available heat exchangers. For air cooling applications, a typical plate temperature for heat exchanger fins ranges from -20 ^{o}C to 10 ^{o}C, and the air relative humidities from 20% to 60% with coil face velocities from 1.0 to 5.0 m/s. For typical fin spacings, these velocities translated to an

inlet Reynolds number range from 430 to 2100. Although these Reynolds numbers appear to be too low to maintain good heat transfer coefficients, the complexity of the airflow passages is such that turbulence is used to enhance the heat transfer coefficients throughout the airflow passages. In addition to the turbulence created by air flow over the coil tubes, the fins on these tubes are usually manufactured with a wavy pattern to enhance the heat transfer. The airflow onto the coil face is usually quite turbulent, however, many coils are now made with leading edge vortex generators on each fin which are designed to enhance the heat transfer coefficients right from the leading edge. In this study, the typical plate temperature of the heat exchanger ranged from -5 ^{o}C to -15 ^{o}C, and the air relative humidity was from 30% to 60% with the average air velocities from 1.1 to 2.7 m/s. For a 20 mm air channel, these velocities gave an inlet Reynolds number range of 3000 to 7000, i.e. a turbulent airflow existed at the inlet to the test section. In this study, the surface of the test section is smooth and flat.

3.2. Description of the Test Loop

A brief description of the heat exchanger test loop is presented here while a more complete discussion of the individual components in the test loop follows this introduction. A schematic drawing of the experimental test loop is shown in Figure 3.1. A photograph of the experimental apparatus is shown in Figure 3.2. The test loop is located in the heat transfer laboratory of the Mechanical Engineering Department. An environmental chamber in the laboratory is used to condition the supply air (both temperature and humidity) for the range of boundary conditions in the experiments.

Pre-conditioned air from the environmental chamber room was supplied to a

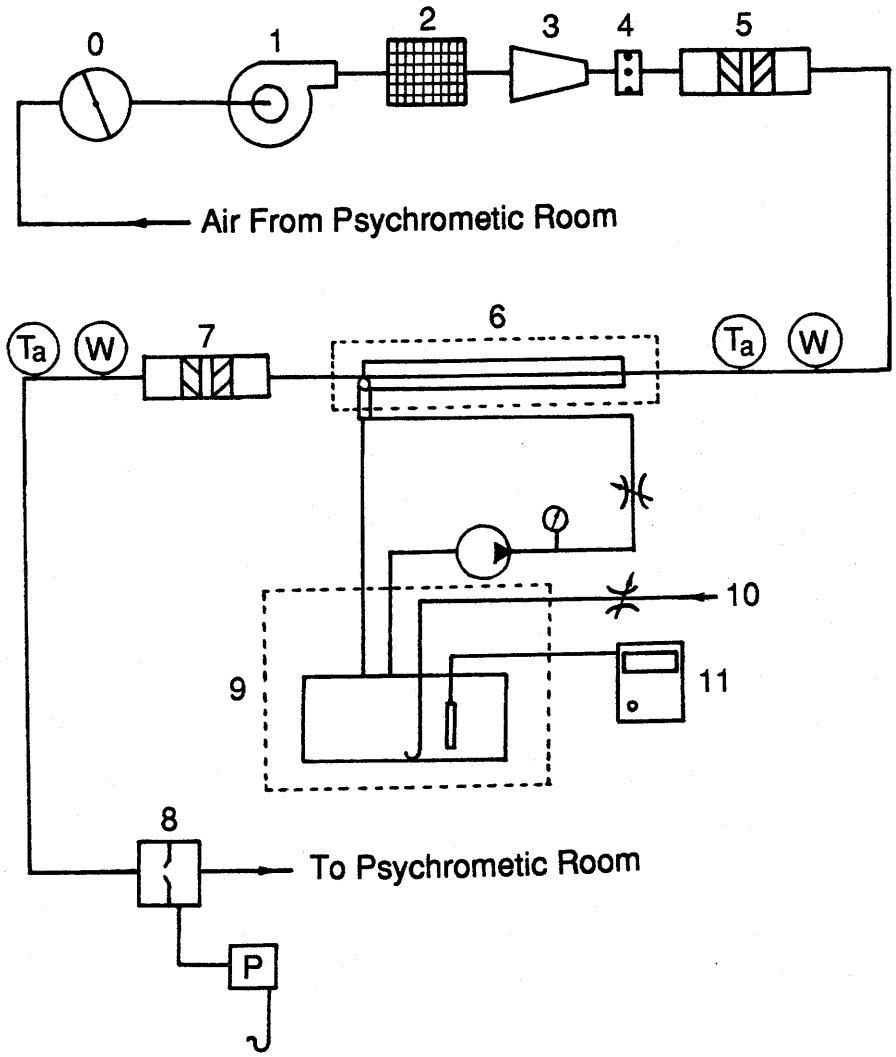

0, Damper
1, Fan
2, Screen
3, Converging Section
4, Turbulent Trip Wires
5, Upstream Turbulent Mixing and Flow Development Section
6, Test Section
7, Downstream Mixing Section
8, Orifice Meter Section
9, Environment Chamber
10, 50% Aqueous Glycol Coolant
11, Temperature Controller

Figure 3.1 A schematic diagram of the test loop

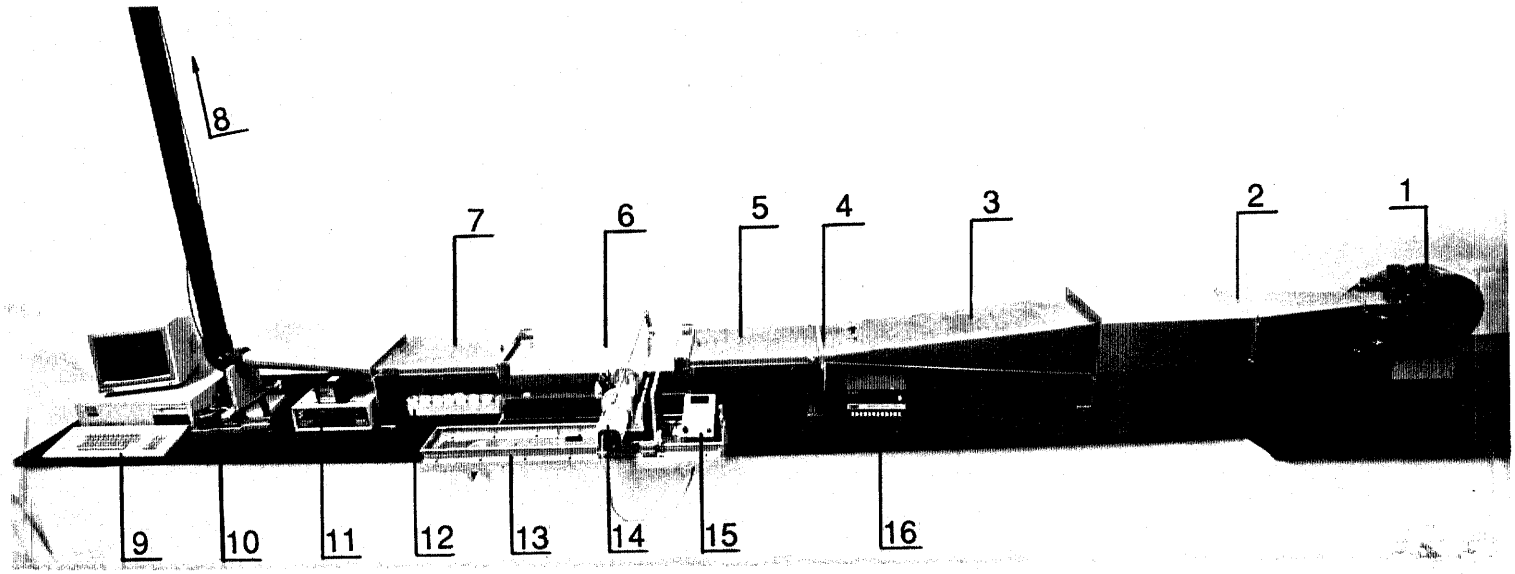

1, Fan
2, Screen
3, Converging Section
4, Turbulent Trip Wires
5, Upstream Turbulent Mixing and Flow Development Section
6, Test Section
7, Downstream Mixing Section
8, Orifice Meter Section
9, Micro-computer
10, Inclined Manometer
11, Data Acquisition System
12, Frost Sample Containers
13, Laser Beam Bed
14, Laser
15, Light Meter
16, Temperature Indicator

Figure 3.2 A photograph of the experimental apparatus assembly

converging and flow-development section by a centrifugal blower (see Figures 3.1 and 3.2). This section provides an additional means of controlling the airflow rate and supplying a uniform fully developed turbulent flow to the test section.

Following the flow development section, the flow is brought into the test section, which is a flat plate heat exchanger, 600 mm long, 280 mm wide with a 20 mm high air channel. Provisions are made in this section to measure the local heat transfer at twenty-one locations on the plate plus the overall change in temperature and humidity of the air as it passes through the heat exchanger. Distributed over the plate surface area, there are also fourteen locations for measuring the frost mass concentration (or mass per unit area). The frost thickness can be measured at any location along the test surface. After leaving the test section, the air flows through a downstream mixing section and into an airflow orifice metering section (tube ID 77.3 mm, orifice ID 40.37 mm). Details of each of the above mentioned components of the test loop are given in the following section. The number next to each component corresponds to that shown in Figures 3.1 and 3.2.

3.2.1. Conditioning Section

The entrance duct to the converging section downstream of the blower, which includes the screen (2), is 2 m long with a cross section of 300 mm by 200 mm. The converging section (3) connected to this duct, smoothly reduces the flow area down to 300 by 20 mm. Following the converging section is a 500 mm long 300 mm by 20 mm final flow development section (5). This is added to insure a fully developed turbulent duct flow. At the exit of the flow converging section, turbulent trip wires (4) are placed on the top and bottom surfaces as well as at the center of the section. The purpose of

these trip wires is to generate turbulence in the flow before it reaches the test section as the turbulence level is very low at the exit from the converging section. There is a series of baffles at the entrance to the final flow development section to insure adequate mixing of the humid air. A humidity sensor located downstream of the baffles is connected to the data acquisition system. In addition, a small rate of air sampling is drawn off to a hygrometer with a chilled mirror sensor. These sensors are used to measure the dewpoint of the air which enters the test section. Five thermocouples are placed 10 cm upstream of the test section to obtain an average air temperature at that point.

3.2.2. Test Section

A schematic diagram of a cross section profile of the test section is shown in Figure 3.3. The test section is mainly a "sandwich" construction which is 600 mm long and has an air channel cross section 300 mm wide and 20 mm high. (see Appendix A for a discussion of the design considerations and methods.)

The air channel is enclosed by two vertical thermal windows, a Plexiglas (acrylic plastic) cover, and the aluminium test surface. The thermal windows allow for direct measurement of the frost thickness using a laser beam method (see Chapter 4) as well as viewing of frost as it forms on the test surface. The radiation exchange between the frost surface and the acrylic plastic cover was minimized by placing aluminium foil on the inner wall of the Plexiglas cover. Figure 3.4 shows a typical fully developed air velocity profile at the inlet to the test section which was obtained using a hot wire anemometer.

The "sandwich" construction of the test section is 600 mm long and 280 mm wide and consists of an aluminium test surface, 3 mm thick (see Appendix A), a polyethylene

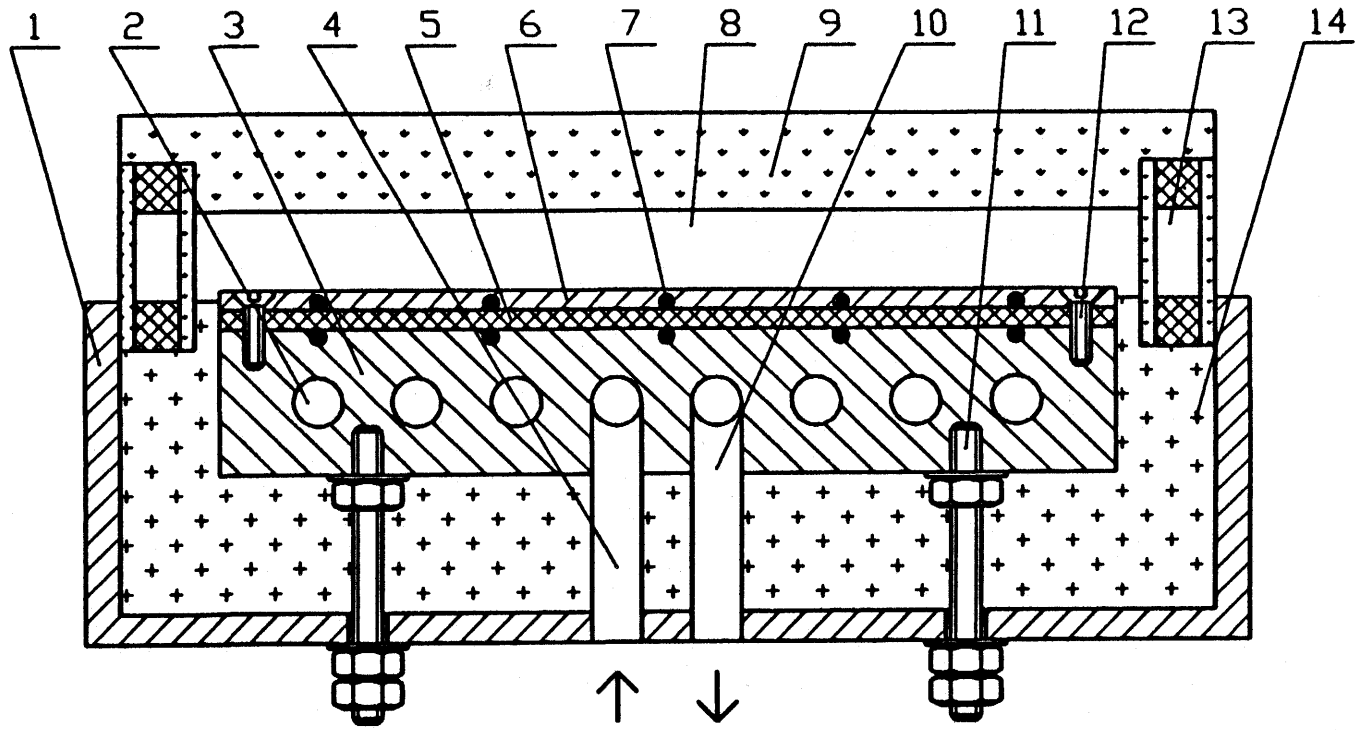

1, Aluminum Frame
2, Aqueous Glycol Coolant Passage
3, Aluminum Cooling Block
4, Coolant Inlet
5, Polyethylene Thermal Resistance Sheet
6, Aluminum Test Surface
7, Thermocouple Pair
8, Airflow Channel
9, Acrylic Plastic Cover Plate
10, Coolant Outlet
11, Nylon Bolt
12, Nylon Bolt
13, Glass Dual Paned Window
14, Extruded Polystyrene

Figure 3.3 A cross section profile of the test section

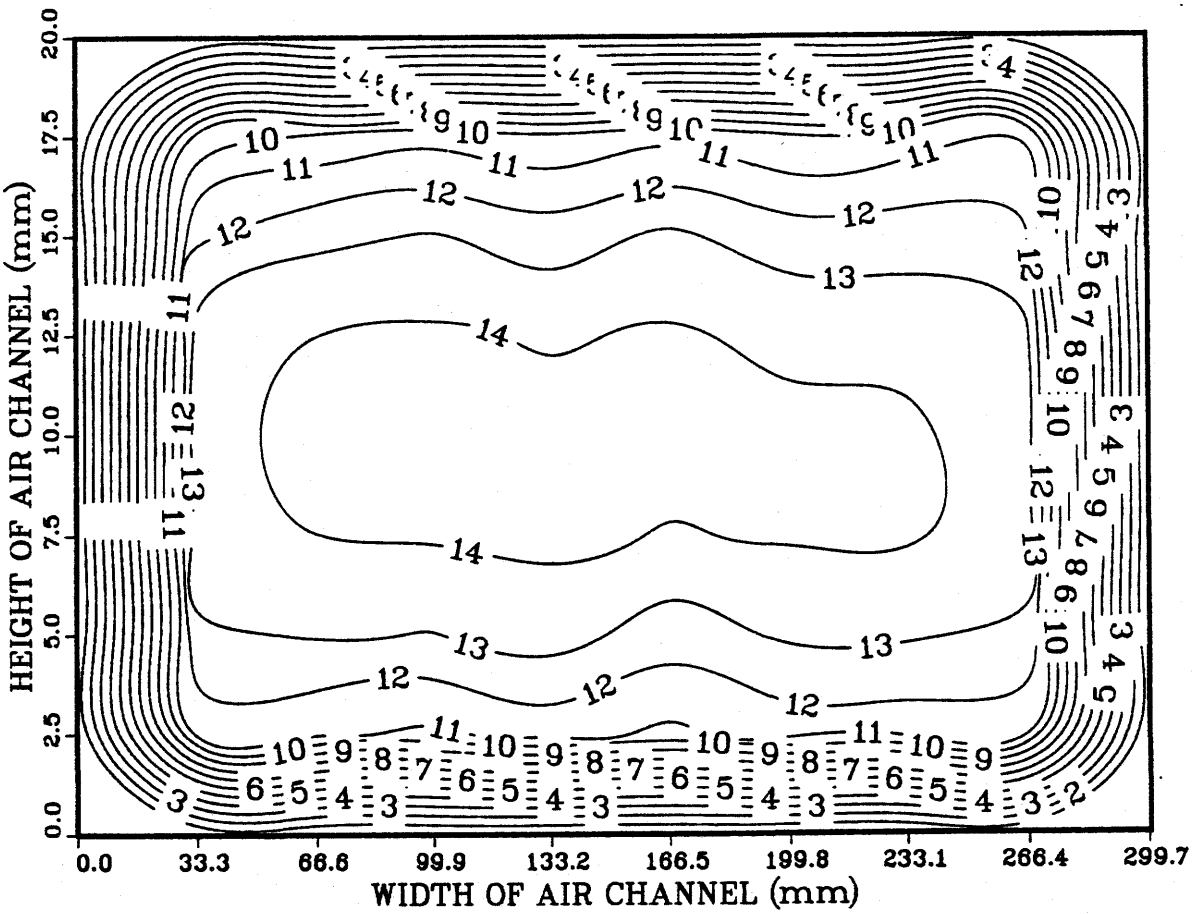

Figure 3.4 The velocity contours in the test section (m/s)

thermal resistance plate (or heat flux meter), 3.25 mm thick and an aluminium heat exchanger cooling block. The polyethylene thermal resistance plate is placed directly underneath the aluminium surface. The air side of the test surface plate was carefully polished, with an average measured roughness of 0.36 μm, to provide a smooth frost deposit surface. The frost mass concentration is obtained at fourteen locations using a flush-mounted disks method (see Chapter 4). The locations of the disks are shown in Figure 3.5. Aluminium was selected as the test surface because it is generally used for the fins of commercial heat exchangers. As well, its high thermal conductivity tends to reduce any surface temperature variations and surface deformations caused by temperature variations on the surface. Figure 3.6 shows the test surface profile under different temperatures, which indicates that there is little or no deformation with a change in the surface temperature.

The heat-flux meter is composed of a high thermal resistance polyethylene sheet with a thermal conductivity of 0.2177 W/m·K, as given by the manufacturer. The polyethylene sheet is sandwiched between the aluminium test plate and cooling block. Thermocouples were embedded in the lower surface of the test plate and the upper surface of the cold block. The gaps between the sheet and the plates in contact were filled with a very thin layer of a thermal paste (Thermal Compound, part No. 120-8 with a thermal resistance of 0.06 $^{o}C \cdot m^2/W$) to minimize contact resistance between the surfaces. The heat-flux meter was calibrated (see Appendix B) to indicate a heat flux for a given steady temperature difference across the high thermal resistance plastic sheet. The local heat flux on the polyethylene sheet was measured at twenty-one locations using forty-two thermocouples mounted in pairs at the locations shown in Figure 3.7.

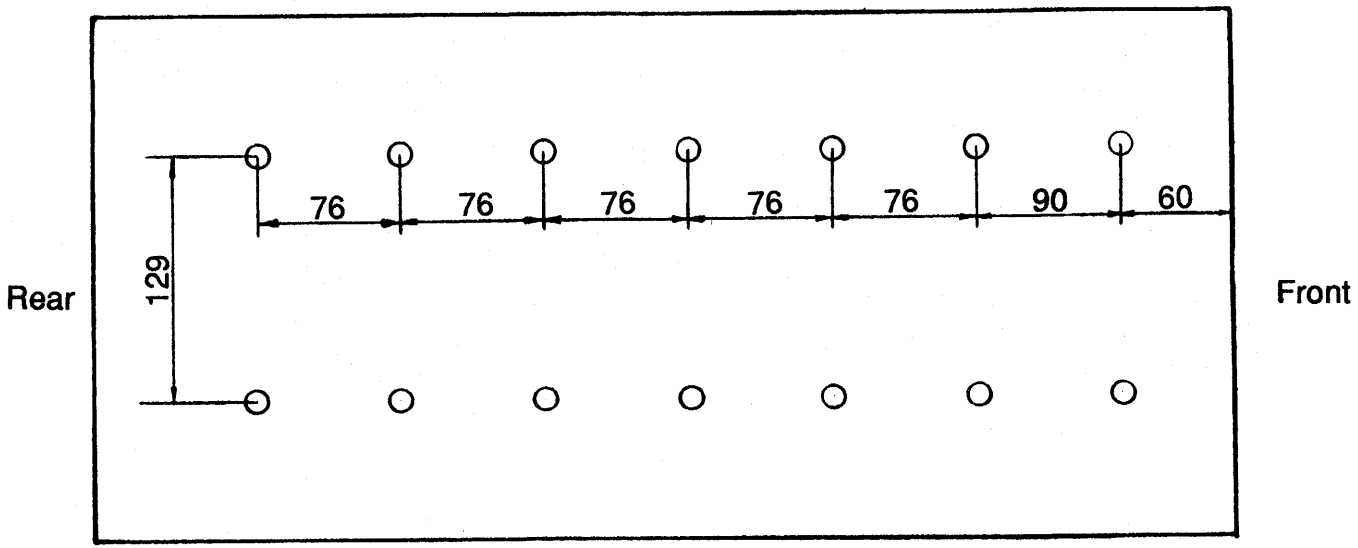

Figure 3.5 Frost mass concentration measurement locations on the test plate (in mm)

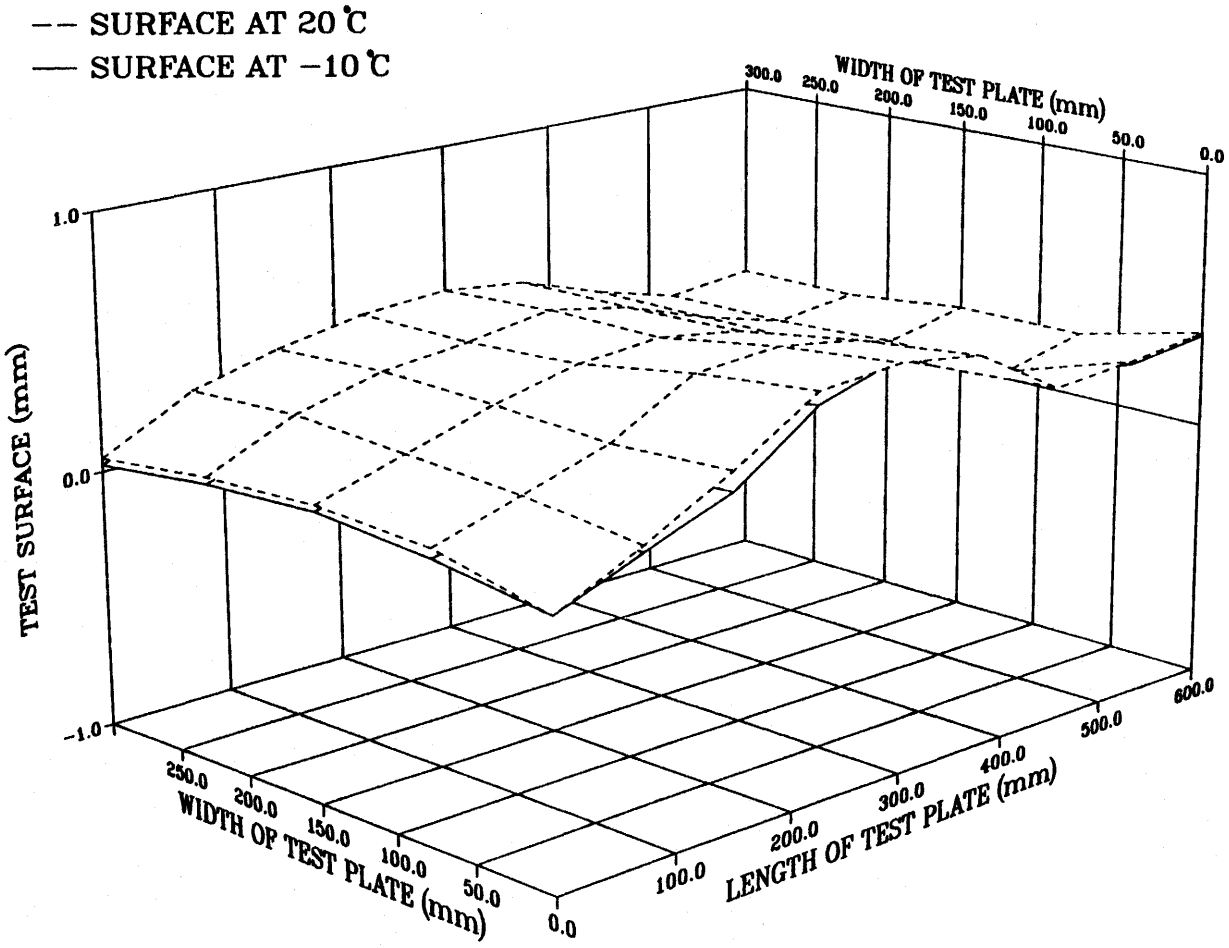

Figure 3.6 The test surface elevation profiles at two different test surface Temperatures (measured using a knife edge on the surface and a laser beam height measuring system, see Chapter 4)

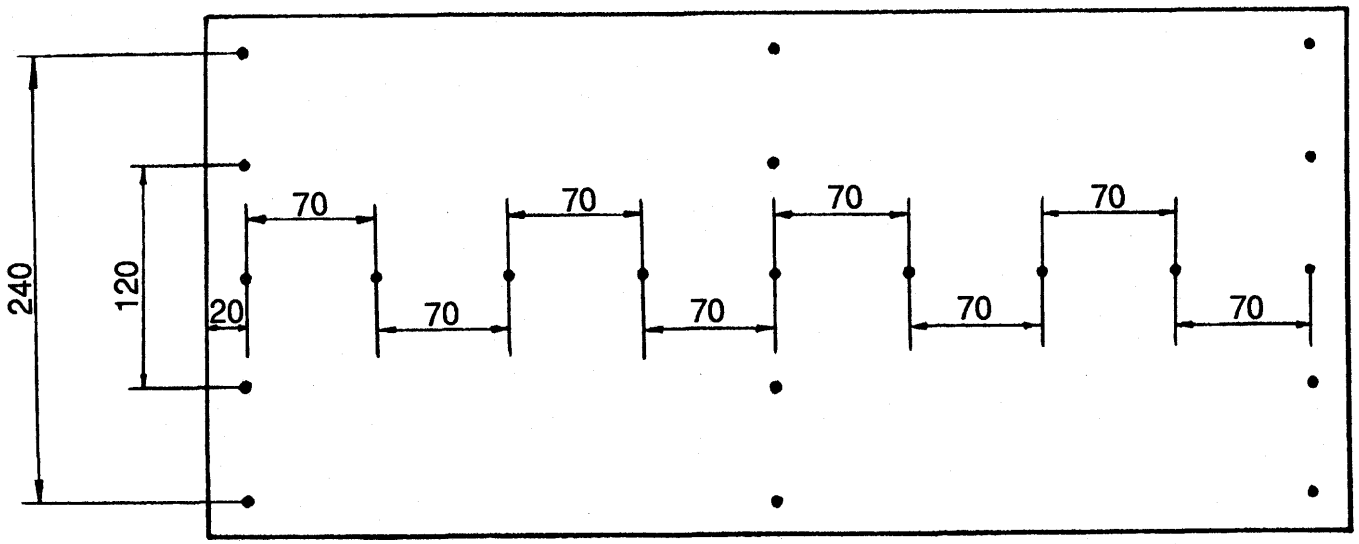

Figure 3.7 Heat flux thermalcouple pair locations on the test plate (in mm)

The temperature differential across the polyethylene sheet was measured at those locations, and knowing the thermal conductivity of the plate, the local heat flux was obtained. A calibration was done for the thermal conductance of this heat-flux meter (see Appendix B) and it was found to be:

$$S=44.4-0.553T \tag{3.1}$$

where S is the thermal conductance ($W/m^2 \cdot K$) and T is the average of the top and bottom surface temperatures of the polyethylene sheet (^oC). In the temperature range of the test runs, the uncertainty in heat flux was estimated at 6%. This equation was used in all the subsequent heat transfer calculations.

The cooling liquid was pumped through 19.05 mm ID circular tubes, which were machined in the aluminium cold block as shown in Figure 3.8. The thickness of the cold block is 35 mm. A chilled 50% glycol-water (by weight) solution is circulated through the tubes cooling the aluminium block, and consequently the test surface, to a desired temperature for the experimental runs. The temperature of the coolant solution was adjusted in the environmental chamber and was constantly monitored at the inlet and exit of the cooling block using two thermocouples. The temperature difference was found to be less than 1 ^oC during all tests. The spacing between the grooves is 16 mm.

The test plate, the heat-flux meter, and the cold block are held together with 10 low thermal conductivity nylon bolts along the edge of the plate as shown in Figure 3.3. The whole section is insulated using extruded polystyrene to minimize any heat transfer from the surroundings. Figure 3.9 shows a typical temperature profile along the test plate and cold block surfaces. As shown in the figure, the test plate is typically warmer at the leading edge. Variations between the front edge and center test plate temperature were

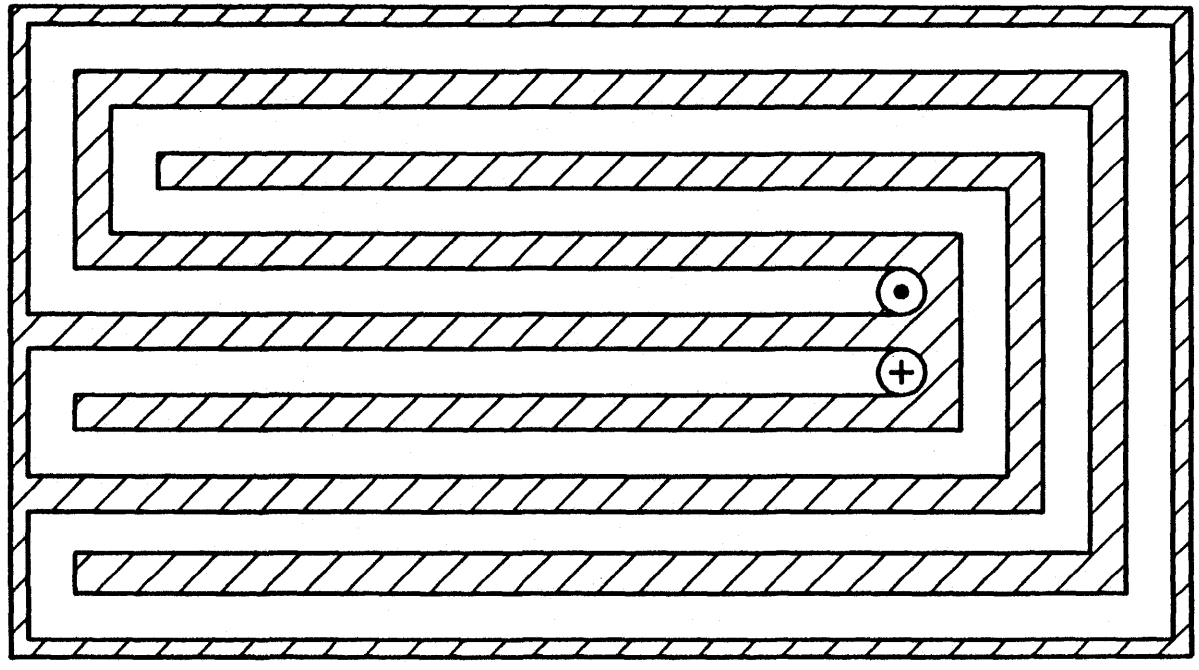

Figure 3.8 A schematic plan view of the cold aluminum block showing the flow path of the aqueous glycol coolant

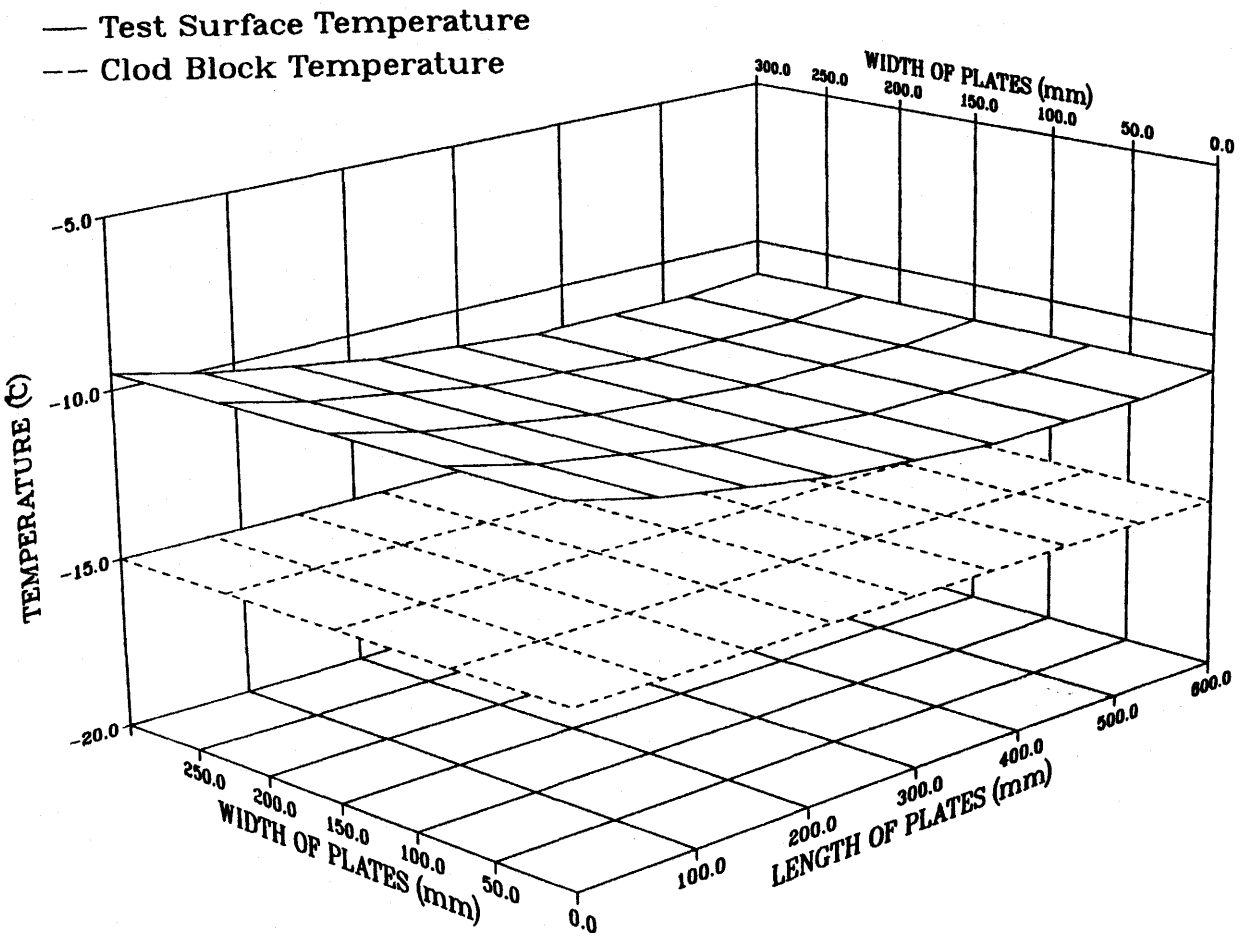

Figure 3.9 A typical temperature distribution on the test plate and the cold block surfaces during frosting

measured to be less than 1.5 °C. This temperature variation is apparently caused by the higher frost mass concentration and convection heat transfer from the warm air at the entrance of the test section near the leading edge. The test surface temperature distribution at any instant in time was fitted to a parabolic curve as a function of the distance from the leading edge with a RMS (root mean square) deviation of 0.1 °C and a coefficient of tolerance of 0.997. This correlated temperature distribution on the test plate was used to correct the measured local heat flux. This gave the corrected heat flux as a function of distance from the leading edge.

All the thermocouples used in the experiments were calibrated using the Ectron Model 1100 Thermocouple Simulation Calibrator system. The temperature errors in the thermocouple readings were found to be less than ±0.1 °C. A typical calibration result is shown in Figure 3.10.

3.2.3. Metering Section

Downstream of the test section, a series of baffles (7) is used in the downstream mixing section to insure good mixing of the air flow. This in turn will allow the measurement of a well mixed bulk air temperature and relative humidity using five thermocouples and a humidity sensor downstream of the baffles. This downstream mixing section is 500 mm long with a cross sectional area of 300 by 20 mm. A transition section was connected to the duct which smoothly converged the flow area into a 72 mm diameter pipe. Then the airflow makes a 90 degree turn and enters a 77.3 mm diameter pipe, 2.4 m long. At the end of this pipe, an orifice meter is located. Pressure taps are located before and after the orifice at one diameter and half diameter, respectively. The orifice meter was designed according to ASHRAE Standard No.41.7-78 and the

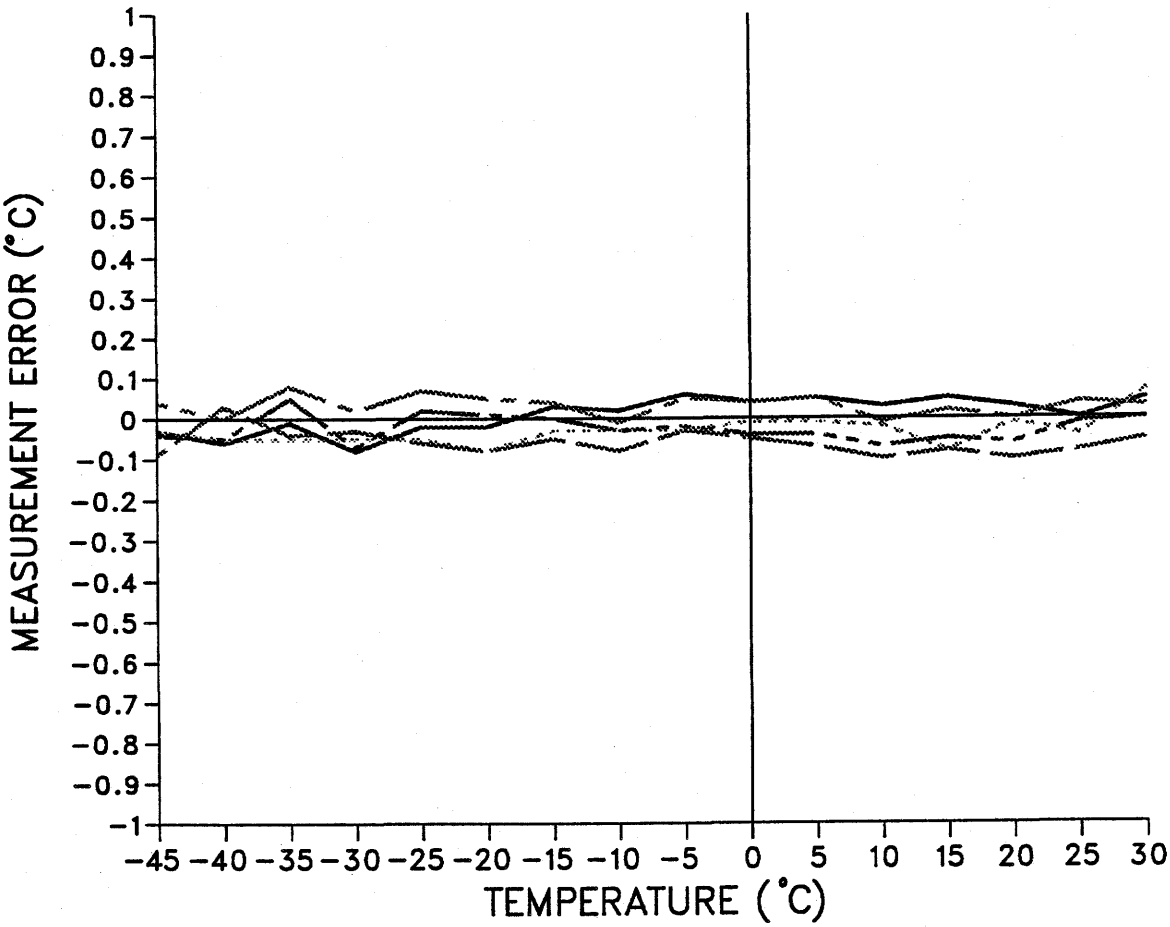

Figure 3.10 Typical calibration result for several thermocouples

International Standard ISO No. 5167-1980(E). Pressure drop measurements across the orifice plate were taken with a Lambreoht inclined manometer, which has an operational range of 0 to 20 cm of oil (SG 0.786).

3.2.4. Data Acquisition

All the data from the thermocouples and the humidity sensor were read using an Electronic Measurement System Model 8082A which was connected to a Commodore PC10 microcomputer (see Figure 3.2). Up to 60 temperature and humidity measurement readings were taken every 20 seconds, averaged and recorded on a floppy disk every 5 to 10 minutes, depending on the duration of the test run. The temperature and humidity readings and histograms were also shown on the computer screen. Once a test was completed, the data from the microcomputer was directly transferred from the floppy disk to the VAX/VMS computer where further analysis of the data was done.

Chapter 4

MEASUREMENT OF FROST THICKNESS AND DENSITY

4.1. Measurement of Frost Thickness Using a Laser Beam and Light Meter

In this section a laser beam method of measuring the thickness of frost on a surface is presented. Figure 4.1 shows the preliminary study of this method (see Besant et al. 1990). The apparatus used to measure the frost thickness, shown in Figure 4.1, consists of a 5 mW helium-neon laser beam light source, a light attenuating filter, and a precision light meter. The laser beam is aligned to pass parallel to the frost surface in such a manner that part of the beam is occluded by the frost on the surface, as shown in Figure 4.2. In this picture, the crystalline frost on the surface has scattered the laser beam into a wide irregular band. A micrometer, shown in Figure 4.1, is used to adjust the position of the test surface due to any variations in the light meter readings. The surface which was used in the preliminary test of frost accumulation is cast aluminium (78 mm by 149 mm) and ground and lap finished to an average roughness of 0.42 μm. The surface was cooled by dry ice (solid CO_2) contained in the aluminium box attached to the back of the test surface.

Figure 4.1 Preliminary experimental set-up:
(a) neon laser, (b) attenuator,
(c) micrometers, (d) cold-plate,
and (e) light meter

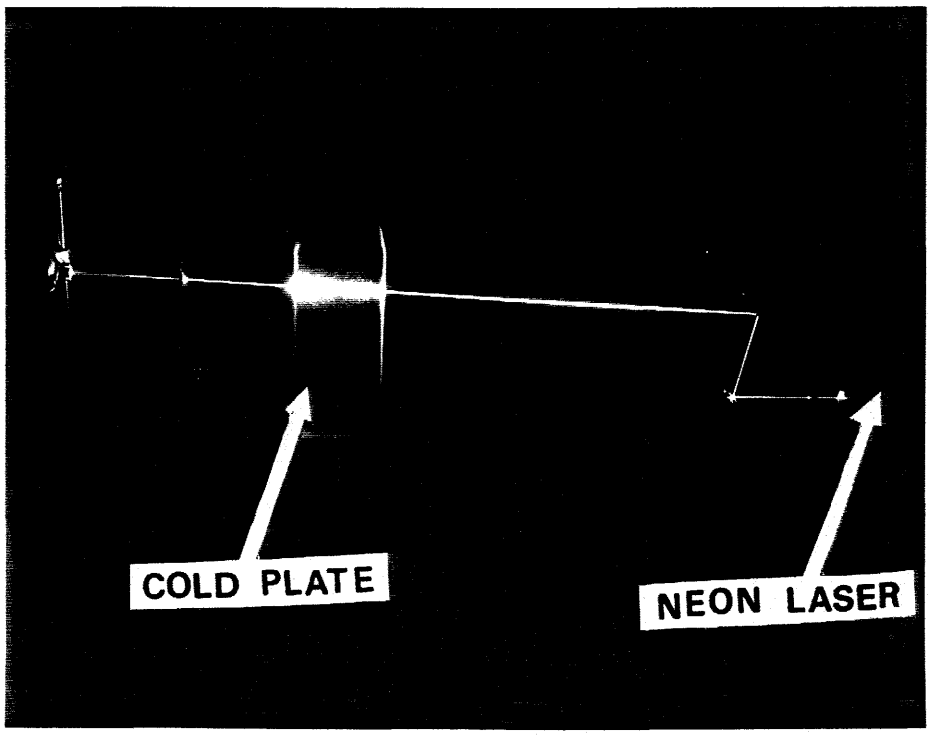

Figure 4.2 Picture showing the laser beam as it passes parallel to the frosted surface and illuminates the crystalline frost, the picture was taken with the room in complete darkness while smoke from a generator was scattering the laser beam

Calibration of this measurement system was provided by substituting a knife edge for the frosted surface and adjusting the micrometer over the width of the laser beam. The results of this measurement calibration, shown in Figure 4.3, indicate that a precision of 0.025 mm was obtained over about a 1 mm range of knife-edge positions. (It is also noted that the diameter of the laser beam is about 2 mm.)

As a further test of this measurement method, a wooden block was machined into a smooth contoured surface and mounted in place of the frosted surface (Figure 4.1). The readings from the laser beam method were compared to the reading from a micrometer, while the surface is moved in the vertical direction using a screw drive. A comparison of the laser beam readings and the dial gauge readings is shown in Figure 4.4. These results indicate maximum discrepancy between the readings of slightly more than 0.025 mm, which is equal to the inaccuracy of the dial gauge.

Finally, a series of five tests were used to measure the growth of frost on the surface shown in Figures 4.1 and 4.2. Each of these tests lasted approximately 20 minutes and the frost was scraped off between each test. The average height of frost and the range of frost thickness measurements are shown at each instant of time in Figure 4.5. The smallest range of data for repeated tests at one time was 0.1 mm. Uncertainties in the initial starting time of about 10 seconds and slight variations in the experimental technique have contributed to the wide scatter of data near time zero in Figure 4.5. Other variations in the range of data were due to random variations in the many independent variables, such as temperature of the surroundings, and to the precision associated with moving the laser beam vertically so that each reading gave a light intensity of 500 μW, as shown in Figure 4.2. The correction due to beam refraction, as it passes through the thermal boundary layer near the test surface, is estimated to be approximately 13 μm.

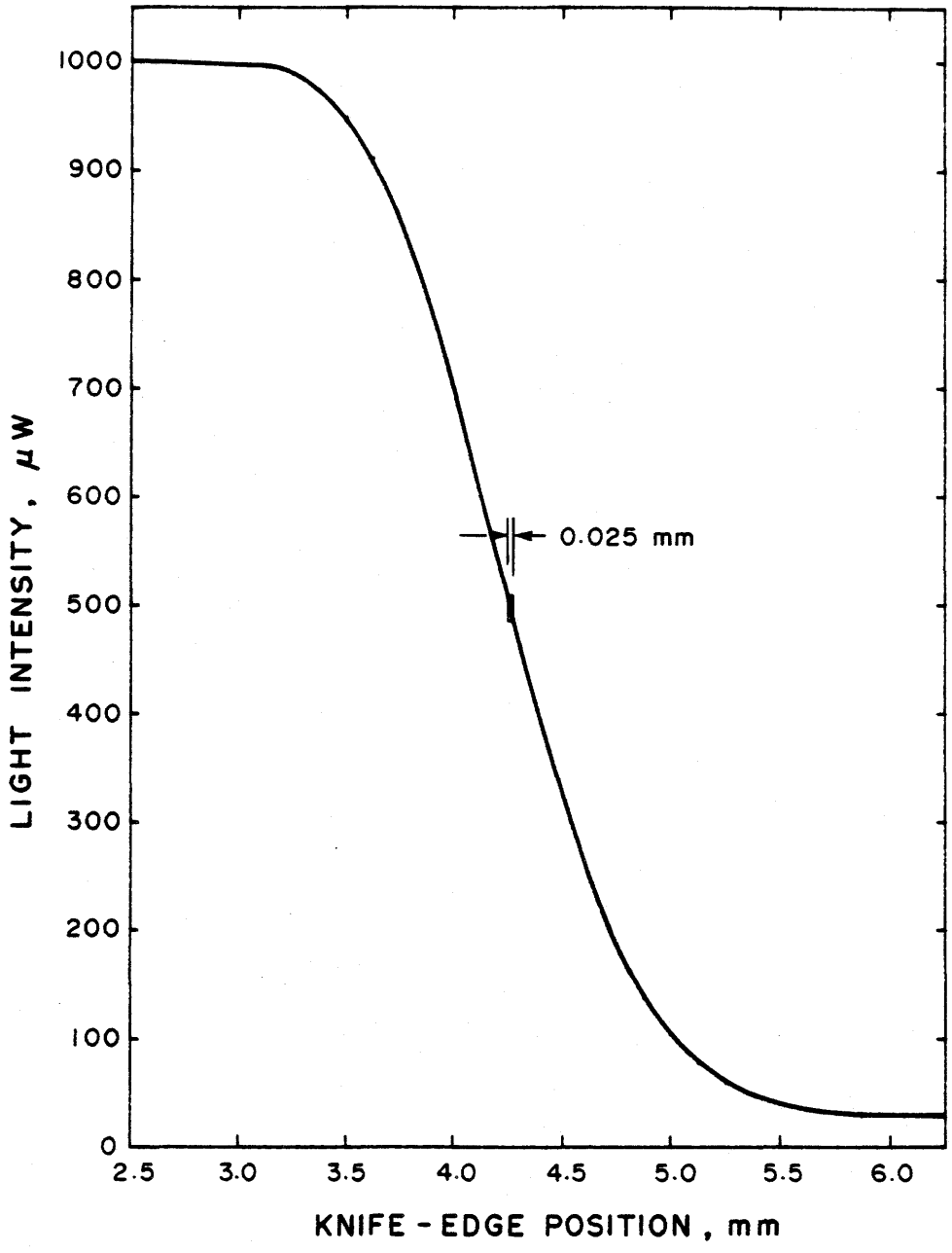

Figure 4.3 Distribution of light intensity with the knife-edge position

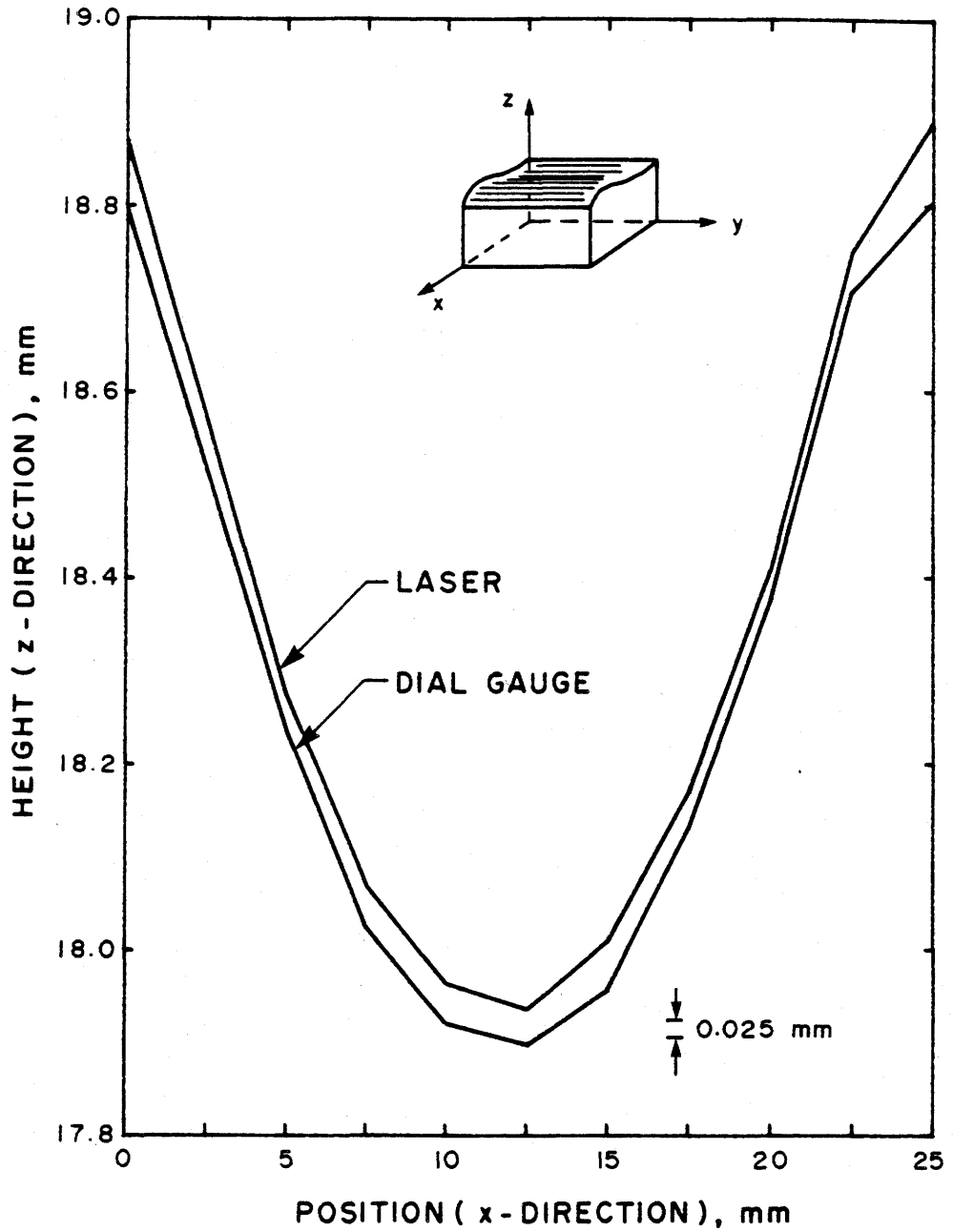

Figure 4.4 Comparison of measurements taken with the laser beam as it passes over the surface contours of a wooden block with micrometer readings

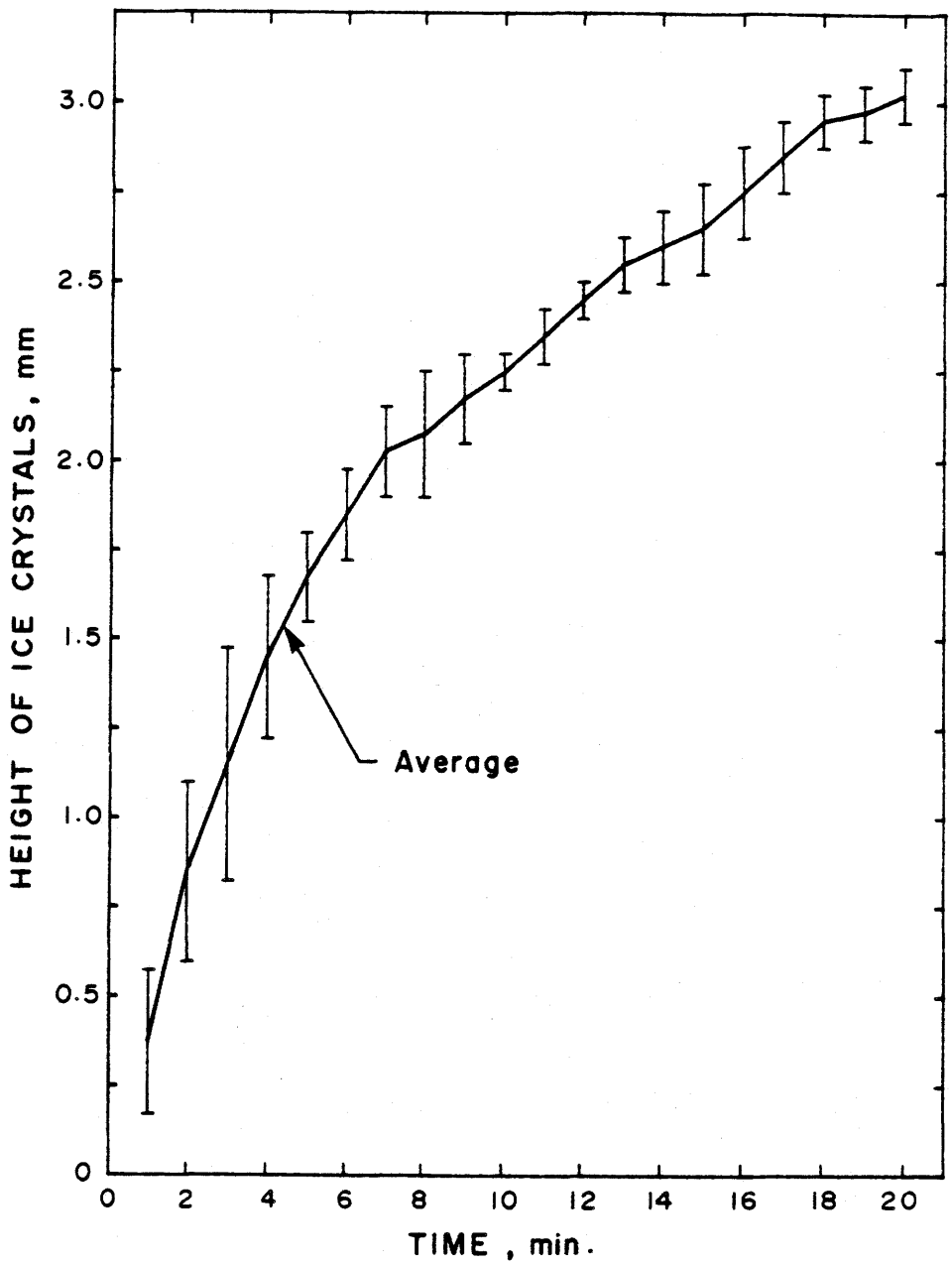

Figure 4.5 Results showing the growth of frost on the cold plate; solid line represents the average height of frost, while the range of frost thickness measurements is given by a vertical band at each point

Figure 4.6 shows the development of frost on the surface and the adjacent laser beam during one test when the surface and the laser beam are fixed. This figure also shows the nature of this particular frost growth pattern on the aluminium surface while it is exposed to room air with natural convection on the surface. Over the first 5 minutes, a thin, uniform smooth velvet layer of ice and frost formed and the laser beam illuminated a single uniform band on this smooth layer of frost. At 7 minutes, the first large crystals of frost can be seen at a few nucleation points. Furthermore, as can be observed by light scattering, the 2-mm-wide laser beam is only partly blocked by a single nucleation crystal located one-third of the distance across the plate. Therefore, this method is best suited to measuring the height of large numbers of crystals that were approximately the same height. At 10 minutes, these nucleation sites are much more numerous and the laser beam is occluded primarily at the leading edge. The growth of the large frost crystals continued and, finally, at 21 minutes, the laser beam is completely blocked and the large crystals completely covered the surface in a uniform, but rough, finish.

A precision of 0.025 mm is obtained for this technique, It is estimated that the inaccuracy of measuring frost thickness may be as small as 0.05 mm with this method since small random variations in the test conditions and in the frost nucleation sites are thought to give rise to the measured variations in frost thickness.

The apparatus used to measure the thickness of frost in the experiments, shown in Figure 4.7, consists of the 5 mW helium-neon laser beam light source, a light sensor, and a precision light meter. The laser beam is aligned to pass parallel to the test surface. The laser beam source and the light sensor are mounted on a plate which is attached to two precision traversing rods with tight fitting linear bearings. The laser and the light sensor

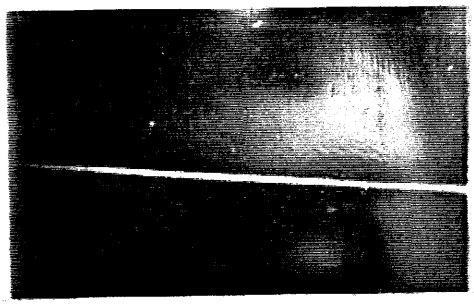

(a) t = 0

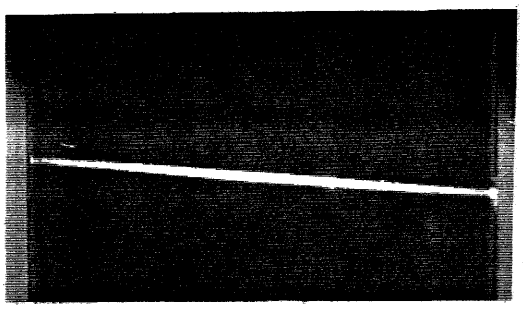

(b) t = 5 minutes

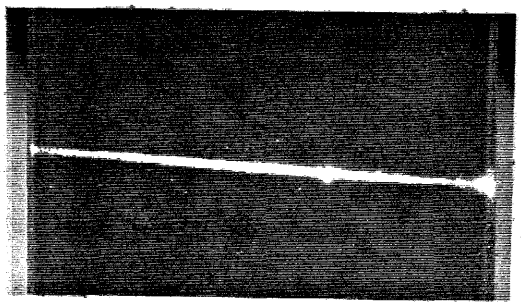

(c) t = 7 minutes

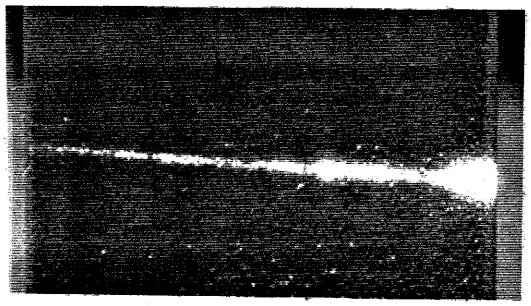

(d) t = 10 minutes

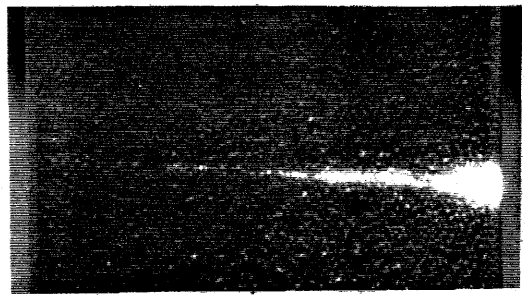

(e) t = 12 minutes

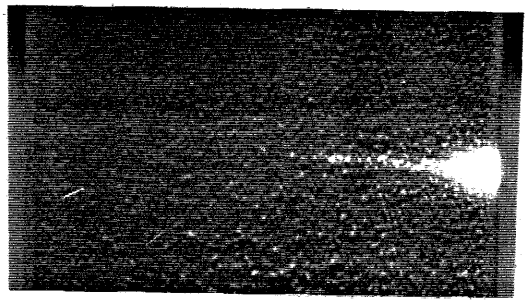

(f) t = 14 minutes

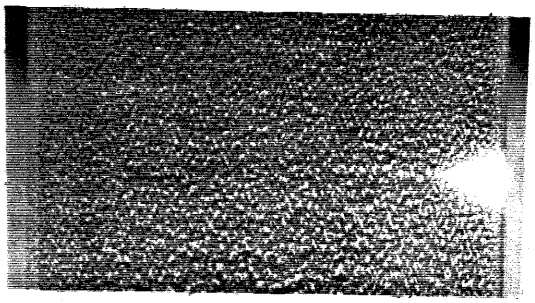

(g) t = 17 minutes

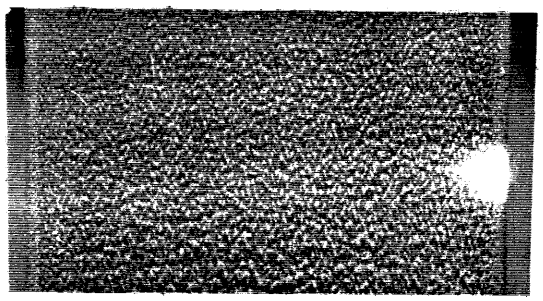

(h) t = 21 minutes

Figure 4.6 Pictures showing the development of ice crystals on a cold plate. Notice how the laser beam illuminated the first occurrence of a crystal peak (c). With further accumulation of crystals, the illuminated area grows in width and in brightness.

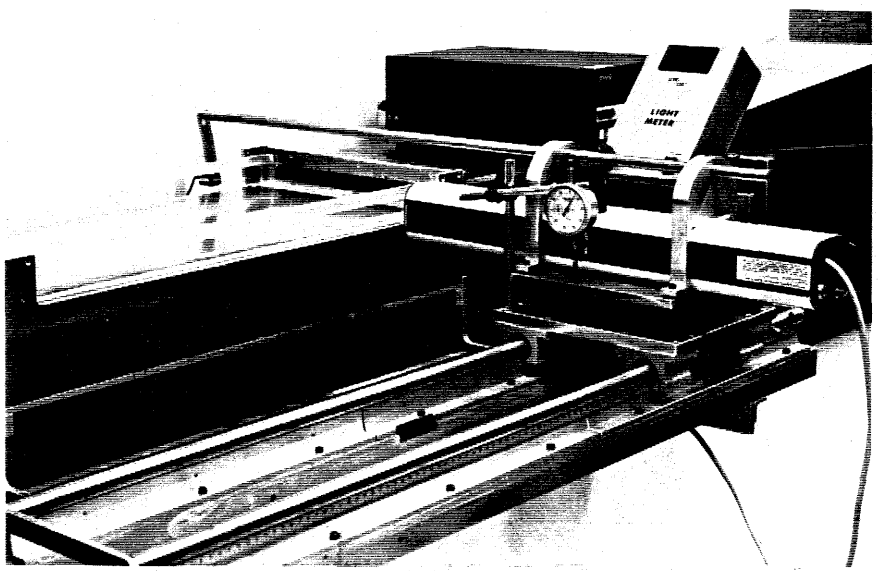

Figure 4.7 Frost thickness measurement experimental set-up

can be positioned at any location along the test surface using this traversing system. A turning screw drive is used to adjust the laser beam moving along a vertical track normal to the test surface, shown in Figure 4.7, to provide adjustments to the light meter readings. The dial gage, shown in Figure 4.7, will give the vertical displacement of the laser beam. The steps to measure the frost thickness are as follows: before the frost grows on the test surface, the laser beam is adjusted vertically to a position such that part of the beam is blocked by the test surface, the light intensity on the light meter and the reading on the dial gage at this position are recorded. This position was called the "no frost" position. As the frost grows, the light intensity measured by the sensor decreases and eventually the laser beam is completely blocked by the frost. To measure the frost thickness at this point, the laser beam is moved vertically until the recorded light intensity returns again to the "no frost" position. Reading the vertical displacement on the dial gage indicates the thickness of frost.

4.2. Measurement of Frost Mass Concentration and Density Using Flush-Mounted Removable Disks

It is clear from the literature review (Chapter 2) on the frost mass concentration and density that there is often uncertainty about the exact measurement techniques used and more uncertainty about the accuracy of the data. Most of the frost density data has been obtained for frost thickness greater than one and often several millimetres thick. Since fin spacing on forced flow heat exchanger coils tends to vary between 1 to 3 mm, there is a need to collect more frost data for thin frost layers which are less than 1 mm thick as the characteristics of frost height on a surface differs significantly with distance from the metal surface. Obtaining accurate data for very thin layers of frost presents a challenge

that has not yet been discussed in the literature. Finally, frost density, like frost thickness, is expected to be a function of the distance downstream from the leading edge as well as time for any given frost accumulation experiment.

A new method of measuring frost density is described hereafter (see Mao et al. 1991 (a)).The frost density is measured at 14 specified locations, uniformly distributed on the large aluminium surface (280 × 600 mm, described earlier in Chapter 3). Air is supplied from a rectangular duct (300 × 20 mm) at one end of the test plate, as shown in Figure 4.8. In these tests, the frost local density was determined by collecting frost on the surface over a period of time (typically 15 to 120 minutes), measuring the frost thickness [Besant et al. (1990)], and removing and weighing the frosted aluminium disks (32mm dia. × 0.5mm thick). These disks were flush-mounted on the test surface by machining the surface to accommodate each disk while high-conductivity thermal paste between each disk and the test surface reduced the contact resistance to a minimum. The average surface roughness of both the disks and the surface was measured to be 0.36 μm.

The procedure used to remove each disk is illustrated in Figures 4.9 to 4.12. These photos show first, the scratching of the frost around the disk using a needle (Figure 4.9) to create a weakened line in the frost around the edge of the disk; second, the lifting of the frosted disk by the small needle (Figure 4.10); third, the removal of the frosted disk by tweezers (Figure 4.11); and finally, the placing of the frosted disk in a plastic container with a tight screw lid (Figure 4.12). This sealed container with the frosted disk enclosed is weighted and then the lid is removed to allow the water from the frost to evaporate before the container and lid with the disk inside is weighed again. This procedure of obtaining first the frost height and then the mass of frost on each disk permits the calculation of the local frost density and mass concentration.

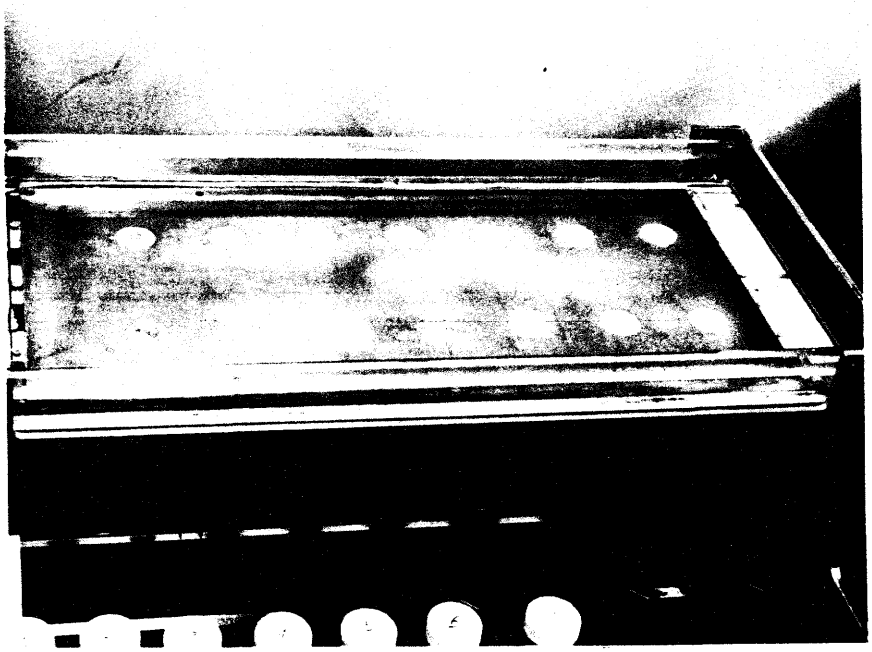

Figure 4.8 Seven flush-mounted removable disks inserted in the test surface on the left and seven disks removed on the right.

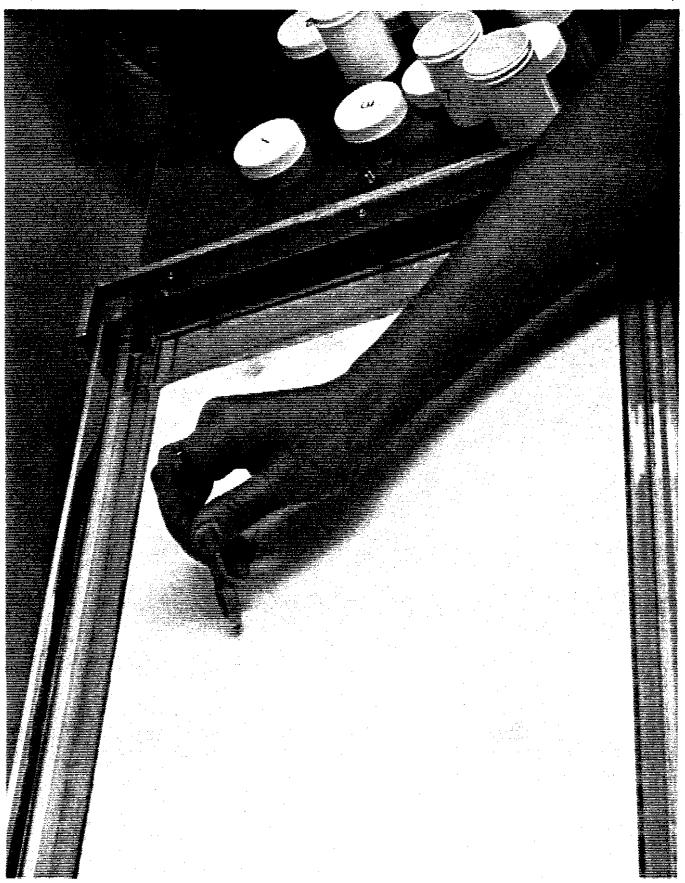

Figure 4.9 The scratching of the frost around the disk using a needle.

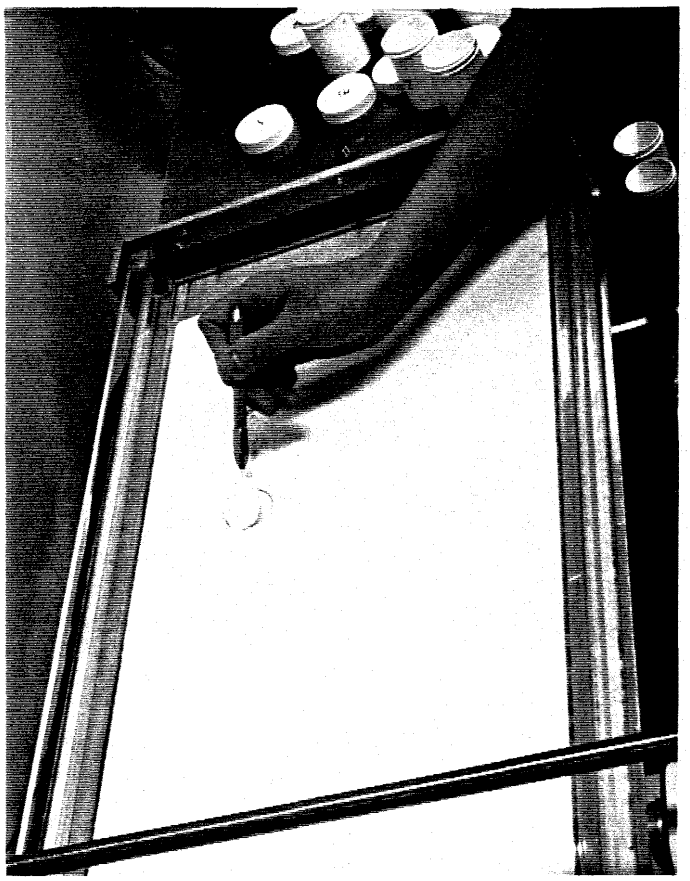

Figure 4.10 The lifting of the frosted disk by the small needle.

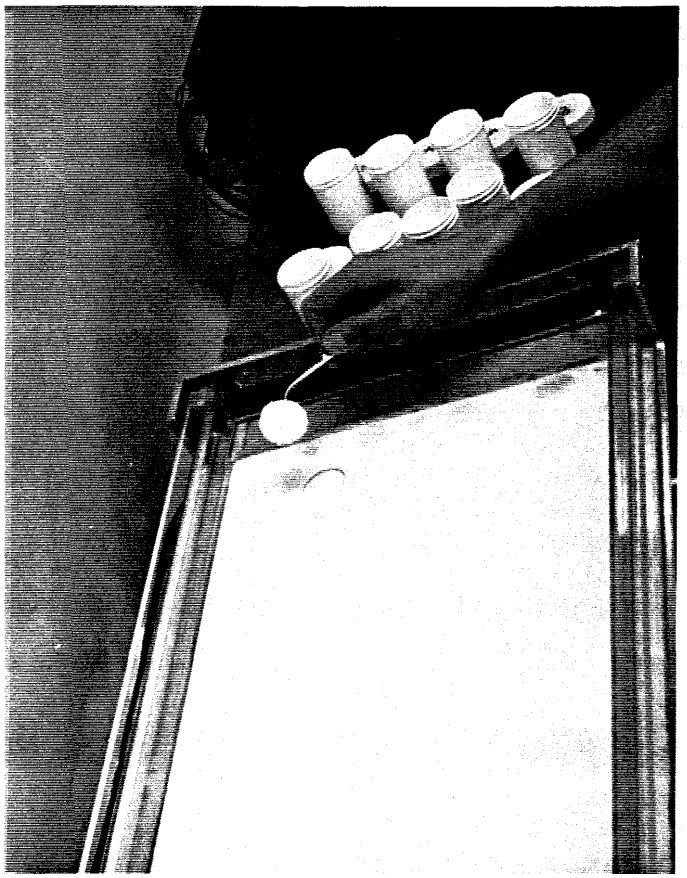

Figure 4.11 The removal of the frosted disk by tweezers.

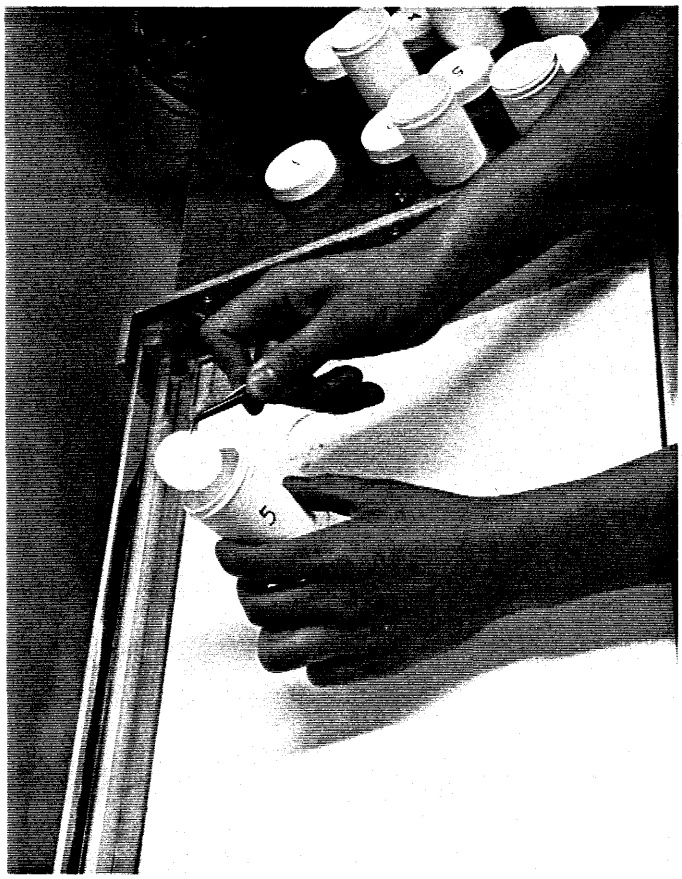

Figure 4.12 The placing of the frosted disk in a plastic container.

A series of tests were performed to measure the local frost average density, ρ_f. Variations in frost density along the X direction of flow were found to be significant (see Figure 4.13 for typical data) while variations across the plate in the Y direction appeared to be negligible. No variations between the frost thickness on each disk and the surrounding plate were observed. Therefore, the maximum difference between the density for the two rows of disks was 6%, as shown in Figure 4.13. A comparison between the measured average density with the data previously reported in the literature, taken under similar conditions, is presented in Figures 4.14 and 4.15. Since the test conditions were not totally reported in the literature, these comparisons may not be under identical conditions. The present frost mass concentration is slightly higher than the data of Tokura et al. (1988), the frost density data agrees very well with the data of Hayashi et al. (1977).

The estimated uncertainty of these measurements can be inferred from the precision of each of the measurements and the variations that were observed in the results. The precision of the frost mass concentration measurement is estimated for each desk, i, using:

$$\frac{\Delta m_{fi}}{m_{fi}} = \sqrt{\left(\frac{2\Delta R_i}{R_i}\right)^2+\left(\frac{\Delta M_{fi}}{M_{fi}}\right)^2} \tag{4.1}$$

and the precision of the frost density measurement is estimated for each desk, i, using:

$$\frac{\Delta \rho_{fi}}{\rho_{fi}} = \sqrt{\left(\frac{\Delta \delta_{fi}}{\delta_{fi}}\right)^2+\left(\frac{2\Delta R_i}{R_i}\right)^2+\left(\frac{\Delta M_{fi}}{M_{fi}}\right)^2} \tag{4.2}$$

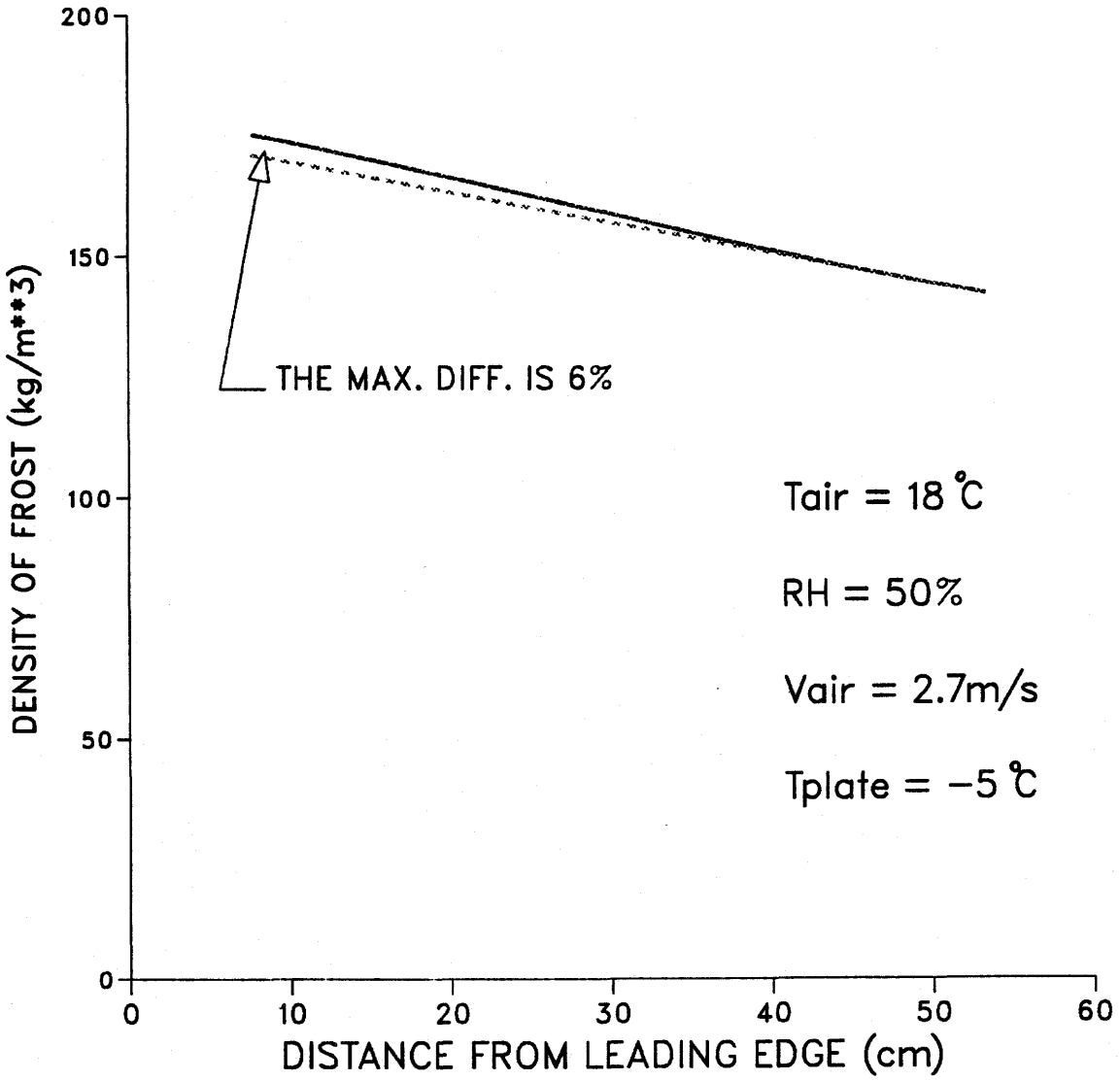

Figure 4.13 Typical data of frost density for each row of disks as a function of distance from the leading edge after 42 minutes of operation.

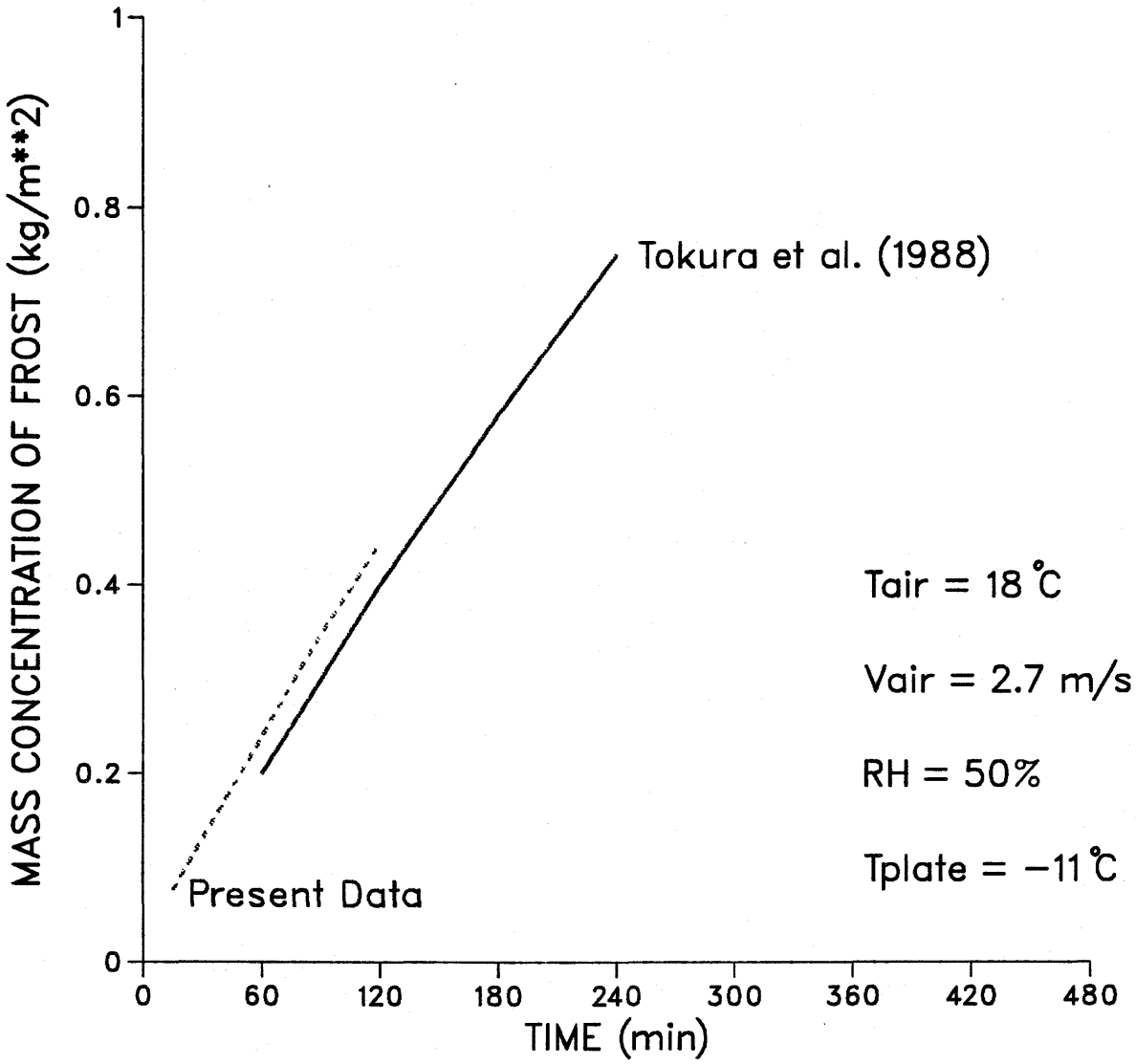

Figure 4.14 A comparison of present data for average plate frost mass concentration with the data of Tokura et al. (1988)

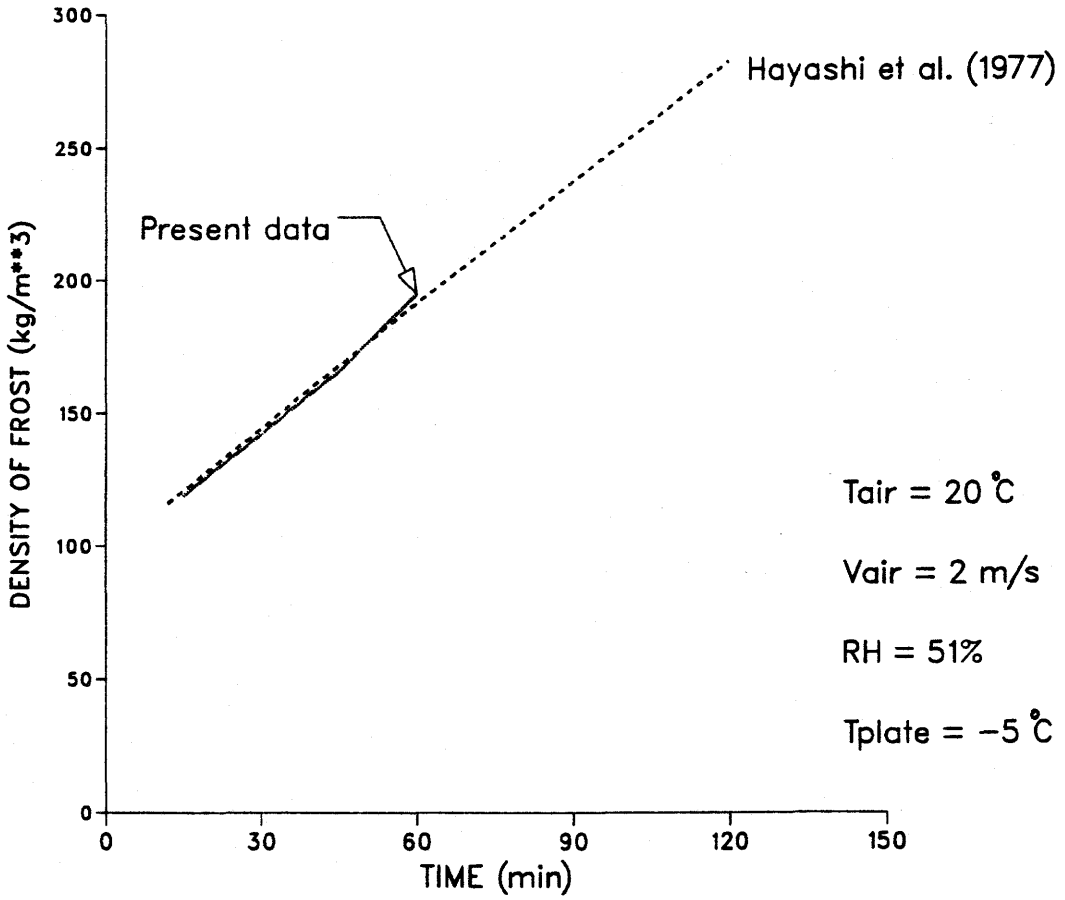

Figure 4.15 A comparison of present data for average plate frost density with the data of Hayashi et al. (1977)

where the uncertainies are taken to be

ΔR_i=0.025+0.08×δ_{fi} (mm)

ΔM_{fi}=0.001 (gm)

$\Delta \delta_{fi}$=0.03 (mm)

0.025 mm is the slot width of the space between each disk and the plate.

The resultant errors for m_{fi} and ρ_{fi} are functions of the frost thickness, as shown in Figure 4.16. The maximum uncertainty of the measurement for ρ_{fi} is 3% for a thickness from 1.5 to 2mm, and less than 6% for frost thickness greater than 0.5mm. As can be seen from Figure 4.16, the frost thickness measurements give rise to large errors for very thin frost thicknesses (δ_f<0.5 mm), but for thicker layers of frost, the area of frost on each disk causes large errors (Eg. (4.2)). For example, δ_{fi}<1 mm, the precision of these frost density measurements is limited mostly by the precision of the frost thickness measurement. On the other hand, for very thick frost thickness, δ_{fi}>4 mm, the precision of the measured density is mostly limited by the precision of the frost area measurement on each disk. Similarly, the maximum uncertainty of the measurement for m_{fi} is 2% for a thickness from 0.6 to 1.5mm, and less than 10% for thickness greater than 0.2mm. For very thin frost thickness,δ_{fi}<0.7 mm, the precision of the frost mass concentration measurements is limited mostly by the precision of the frost mass measurement but for very thick frost thickness, δ_{fi}>4 mm, the precision of the mass concentration is limited mostly by the precision on the measurement of the frost area on each disk.

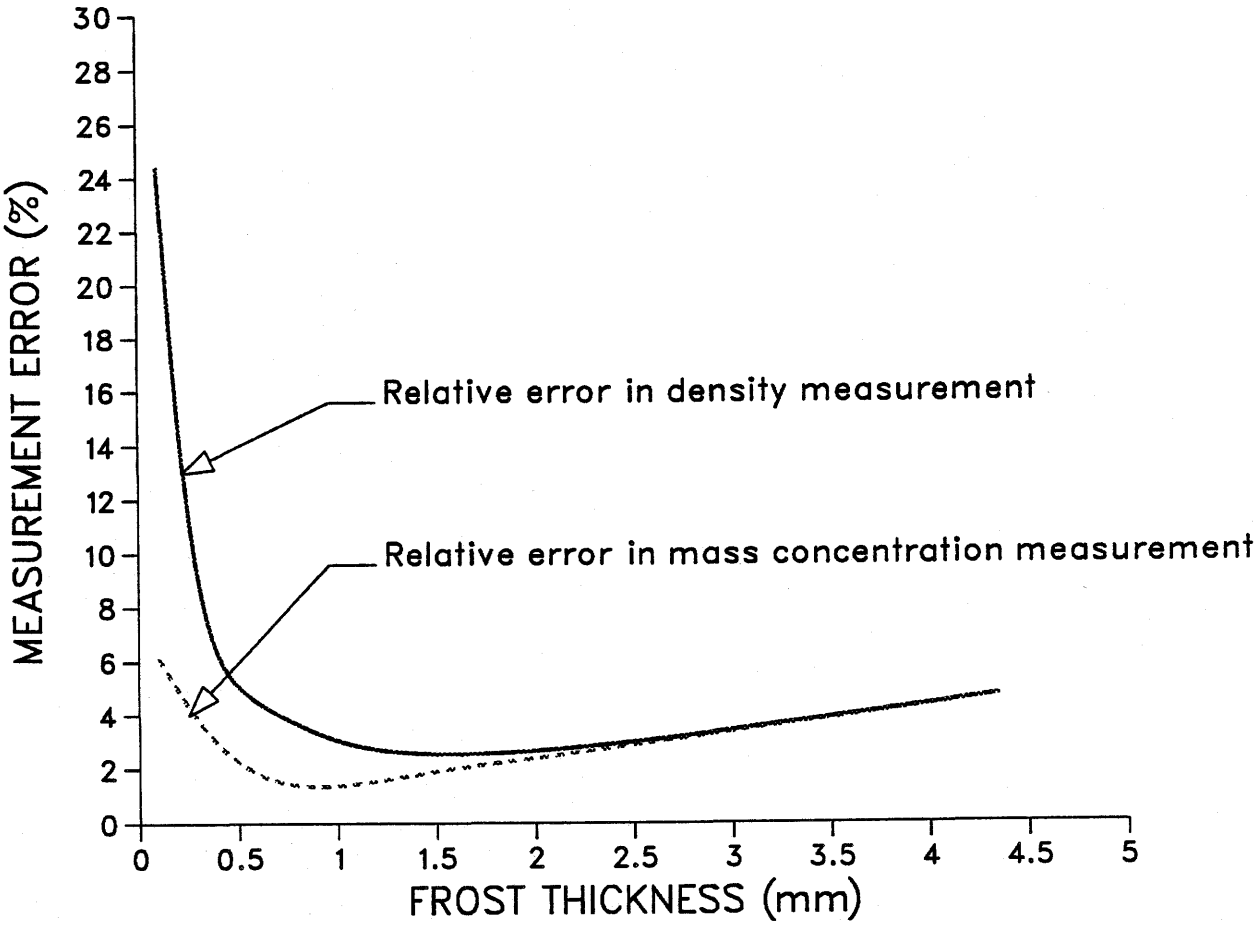

Figure 4.16 Estimated error of the frost mass concentration and density measurements on each disk.

In summary the uncertainty in the frost density measurement is expected to be as low as 3% for frost thicknesses from 1.5 to 2 mm while the mass concentration inaccuracy may be less than 2%, and less than 6% for frost thickness greater than 0.5 mm.

Chapter 5

EXPERIMENTAL RESULTS

Over 50 tests were carried out for frost accumulation and heat flux. Each test was started by precooling the test surface to a preselected temperature without air flow. Then all frost on the surface was removed using alcohol and a dry cloth, the air flow over the test plate was started. The estimated error in establishing the starting time of a test is only a few seconds but at the end of a test the uncertainty is about one minute. Over a two hour test period, variations in the cooling block temperature were less than 1 ^{o}C. Again, over a two hour test period, supply air temperature variations were less than $\pm$ 1 ^{o}C while humidity ratio variations were less than $\pm$ 0.0005. Data from all the sensors were sampled every 20 seconds, averaged over 5 minutes and recorded on disk for later analysis. The duration of a test was between 30 minutes and two hours. Each airflow and plate temperature test condition necessitated a whole sub-series of tests to measure the mass concentration distribution on the plate every 15 minutes over a two hours period. The double set of seven removable disks on the plate permitted two sets of data on frost properties before the experiment had to be started again under identical operating conditions. Thus over the two hour period, the same experiment test was started four times. During a test, the thermal and mass transfer boundary layer development on the cold test plate results in frost thickness, mass concentration, heat flux, and test plate temperature distribution which change with time and distance from the leading edge.

Experimental results are presented and discussed in this chapter. Results are given in terms of the following frost properties: frost thickness, mass concentration, density, thermal conductivity, heat transfer coefficient and mass transfer coefficient. A correlation analysis is presented for each of the properties as well as Nusselt number for heat transfer and Sherwood number mass transfer. The range of independent test parameters is given in Table 5.1.

Table 5.1 Range of Environmental Parameters Used in the Experiments

Parameter	Range
Time (minutes)	0 to 120
Distance from leading edge (mm)	0 to 600
Test surface temperature (^{o}C)	-5 to -15
Supply air humidity ratio (kg/kg)	0.004 to 0.01
Supply air temperature (^{o}C)	15 to 23
Supply air velocity (m/s)	1.15 to 2.67
Inlet Reynolds number	3000 to 7000

5.1. Frost Thickness

The first set of results shows how the frost thickness (i.e. one of the dependent frost properties) varies with each of the independent test parameters. Figure 5.1 shows a typical set of data for the frost thickness on the test plate versus time and position. The frost thickness and the rate of frost growth increased with time in the first 45 minutes. After this, the rate of frost growth decreased even though the frost thickness still increased. Over the two hour test period, one can deduce that the frost growth rate tends

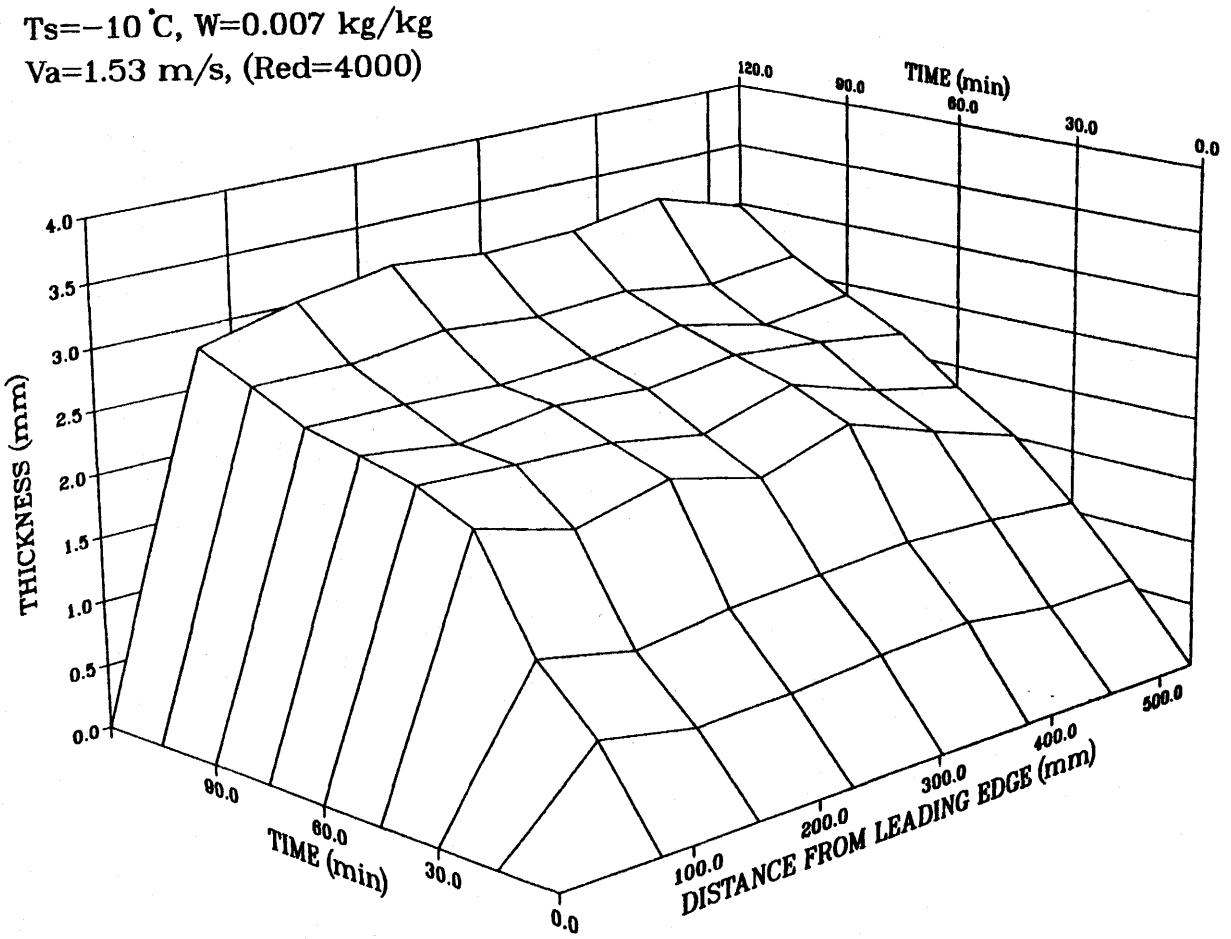

Figure 5.1 Typical results for frost thickness versus time and position

to decrease with time. It could be also seen from Figure 5.1 that during the first 45 minutes, the frost layer is thicker near the leading edge than that downstream. After 45 minutes time the frost becomes more uniform over the entire test plate up to about 90 minutes and then the frost thickness tends to increase with distance from the leading edge. These data confirm the phenomenon observed and described earlier by O'Neal (1982). Therefore, in this case, the local frost growth rate along the plate tends to increase with the distance from the leading edge over a 2 hour test period, with a frost thickness less than 3.5 mm.

In Figure 5.1, the frost thickness versus time and distance surface is not exactly smooth. This is due to experimental uncertainties in the data and slight differences in operating conditions between tests. In order to observe the growth of frost with time at any position on the cold plate, Figure 5.2 presents the correlated data on frost thickness as a function of position with time as a parameter for three different cold plate temperatures. In this figure, the frost thickness data at each position, x, from the leading edge are correlated with time, t (min.), using the parabolic equation:

$$\delta_f = a_1 t + a_2 t^2 \tag{5.1}$$

where a_1 and a_2 are empirical constants.

The resulting root mean square errors did not exceed 0.18 mm and the coefficient of tolerance always exceeds 0.99. In Figure 5.2, the frost growth is, except near the leading and trailing edge, very uniform. Up until 90 minutes, the frost thickness at x=60 mm is larger than at 150 mm. Further downstream, the frost increases with distance and time until x is about 380 mm. Beyond this point, the frost thickness decreases with distance. After 90 minutes, the frost thickness increases with distance from the leading edge until x

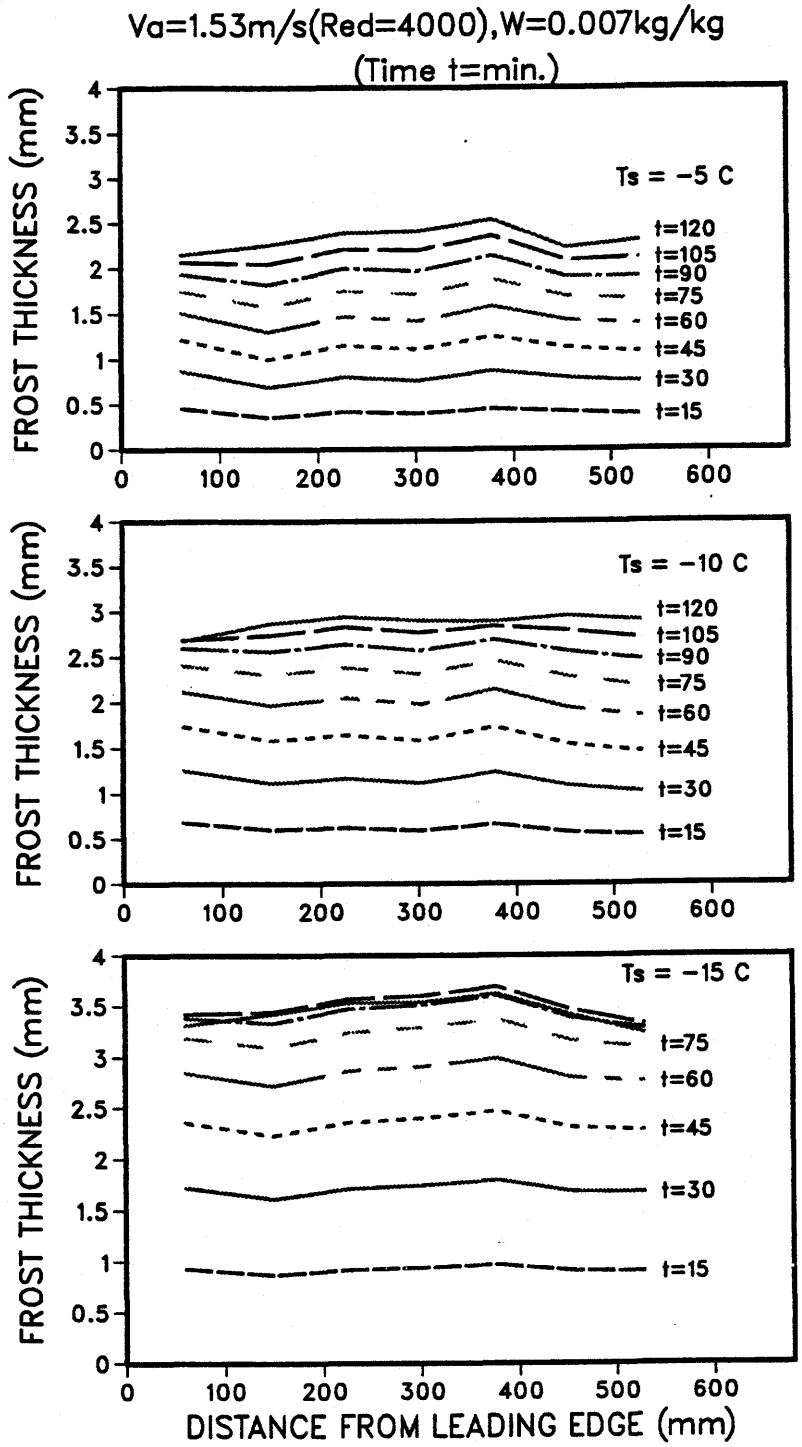

Figure 5.2 Frost thickness versus position where time is a parameter

is about 380 mm where, for all but one point, it decreases with distance from the leading edge.

At a particular time, plate temperature and inlet air speed or Reynolds number, typical data for the distribution of the local frost thickness with changes in air humidity ratio is shown in Figure 5.3. This result shows that as the water vapour concentration in the air increases, there is a corresponding increase in the frost thickness. For a particular set of test conditions, Figure 5.4 shows the frost thickness versus the average test surface temperature, which indicates that frost thickness increases with decreasing test surface temperature. These results are in agreement with similar data reported in the literature.

Figure 5.5 shows the frost thickness variations with the change in air speed or inlet Reynolds number (based on the inlet hydraulic diameter). As shown, the frost thickness increases with increasing air speed or Reynolds number. Also, Figure 5.5 shows that, at lower Reynolds numbers (3000), the frost thickness is thicker toward the leading edge of the plate than the rear while, at high Reynolds numbers (4000) the frost thickness is nearly independent of position. These data quantify the phenomenon described by O'Neal et al. (1984).

Although the measured data could, in theory, be used directly in the estimation of frost thickness on any surface, it is convenient to use a dimensionless correlation for the prediction of frost thickness under different, but similar, test conditions. Such correlations are independent of the dimensions selected for each properties; however, the dimensionless variables and their range of variation must be completely defined. For such correlations, each dependent and independent variable is put into a dimensionless form.

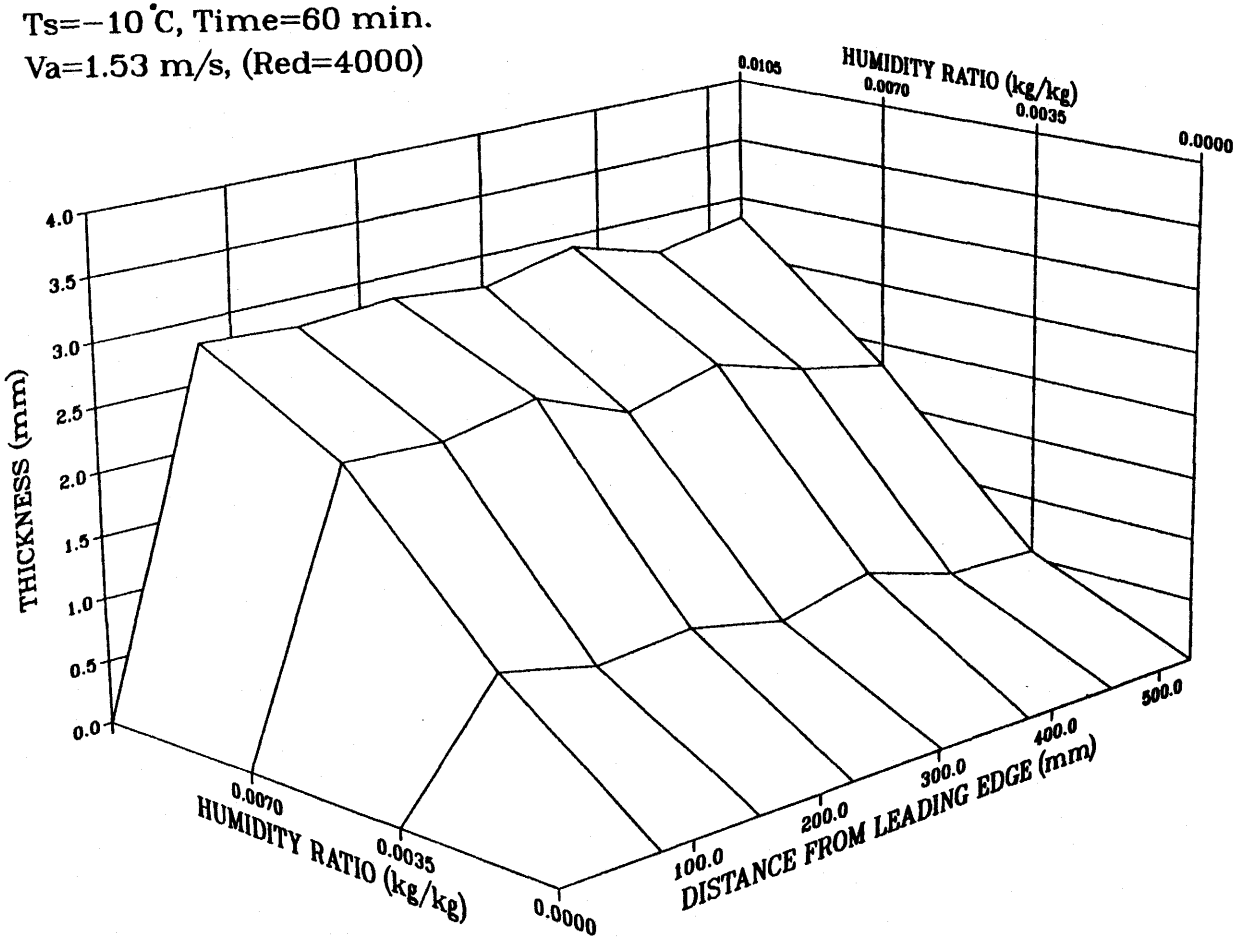

Figure 5.3 Frost thickness versus air humidity ratio and position

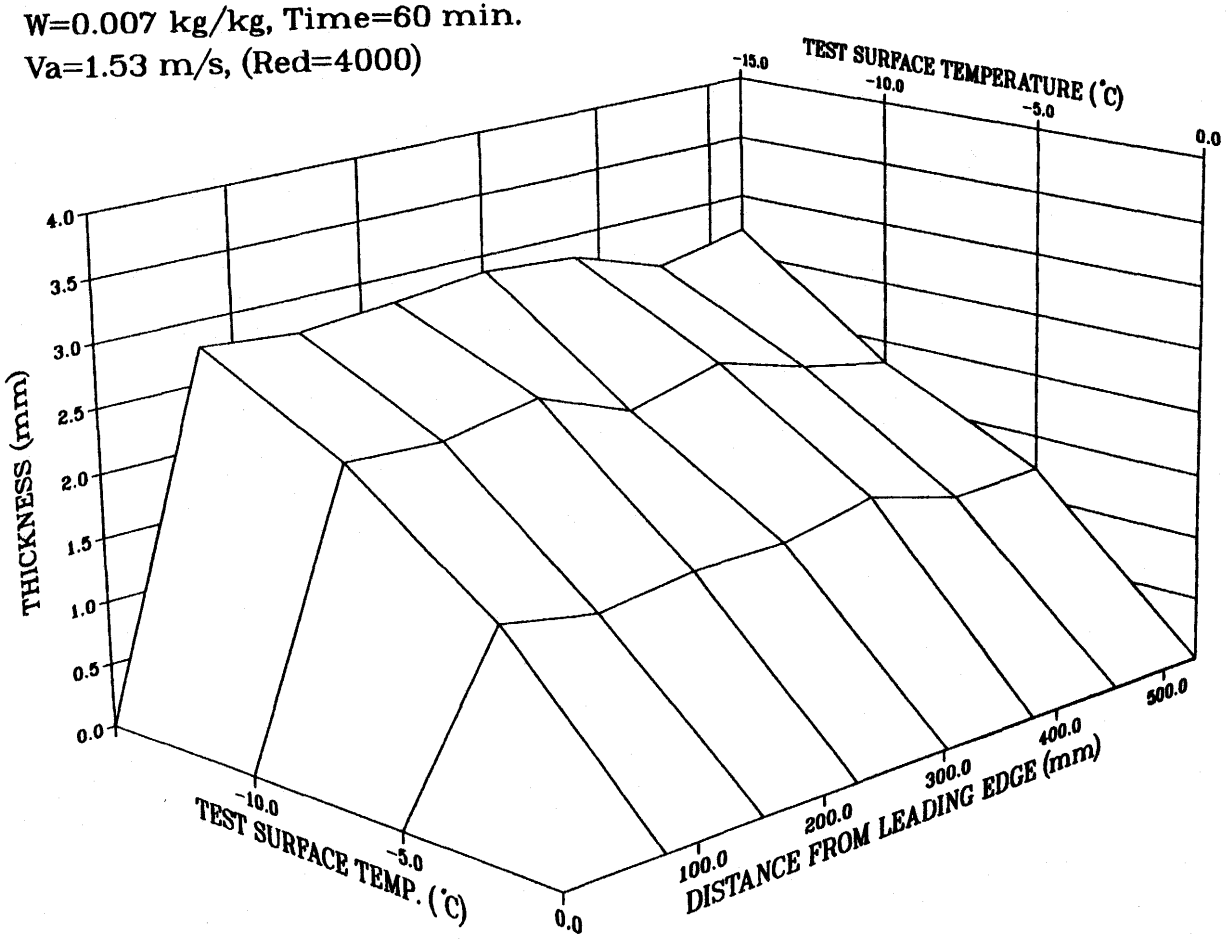

Figure 5.4 Frost thickness versus test surface temperature and position

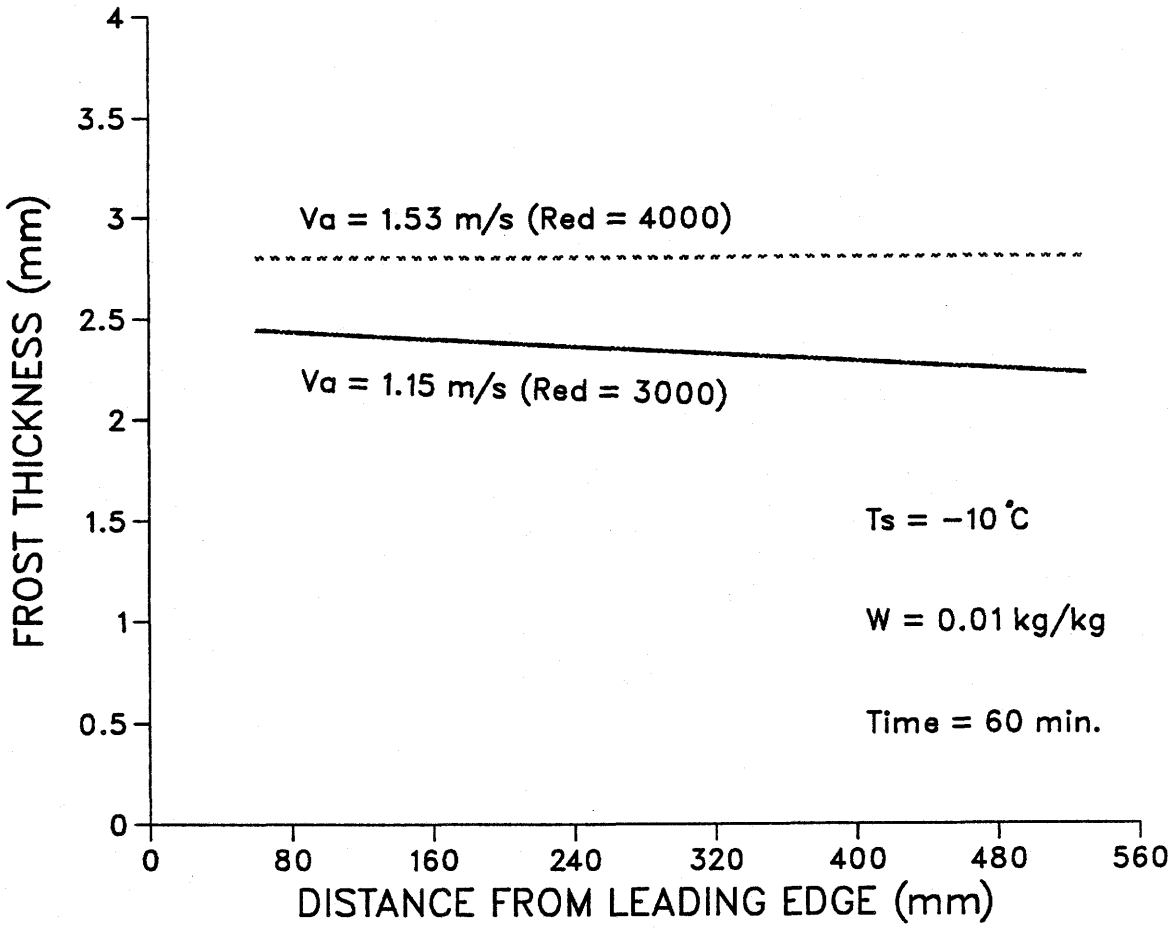

Figure 5.5 Frost thickness versus position with inlet air velocity or Reynolds number as a parameter

For frost thickness, we can use the frost thickness divided by the thickness of ice for the same mass concentration, δ_f/δ_i. For a constant ice density, this ratio is proportional to the ratio of frost thickness, δ_f, and mass concentration of frost, m_f.

A dimensionless correlation of frost thickness summarizes the relationship of frost growth rate with each independent test parameter:

$$\frac{\delta_f}{\delta_i}=187450(X^*)^{0.132}(W)^{0.405}(T^*)^{1.017}(R_{ed})^{-0.720}(F_o)^{-0.253} \tag{5.2}$$

The dimensionless test parameters have the following ranges: $1.33<X^*<14.13$, $0.004<W<0.01$, $0.24<T^*<0.51$, $3000<R_{ed}<7000$, $13<F_o<104$. where:

$\frac{\delta_f}{\delta_i}$ Dimensionless frost thickness

δ_f Frost thickness (m)

δ_i Ice thickness, $\delta_i=\frac{m_f}{\rho_i}$ (m)

m_f Frost mass concentration (kg/m^2)

ρ_i Density of ice, 920 (kg/m^3) at 0°C

X^* Dimensionless position, $X^*=\frac{x}{D_h}$

x Distance from the leading edge of test plate (m)

D_h Hydraulic diameter at inlet of the test section, D_h=0.0375 m.

W Air humidity ratio at the test section inlet (kg/kg)

T^* Dimensionless temperature, $T^*=\frac{T_{tp}-T_{ts}}{T_a-T_{ts}}$

T_{tp} Triple point temperature, 0 °C

T_{ts} Local test surface temperature (°C)
(For a given test, this temperature
varies with distance from leading edge.)

T_a Air temperature at the test section inlet (°C)

R_{ed} Inlet Reynolds number based on the hydraulic diameter,
$R_{ed}=\frac{V_a \cdot D_h}{\nu_a}$

V_a Air velocity at the test section inlet (m/s)

ν_a Kinematic viscosity of air, at the film temperature (m^2/s)

F_o Fourier number, $F_o = \frac{\alpha_a \cdot t}{(D_h)^2}$

α_a Thermal diffusivity of air, at the film temperature (m^2/s)

t Time (s)

A comparison between the measured data of dimensionless frost thickness with the correlation of Eq. (5.2) is shown in Figure 5.6. The root mean square of Eq. (5.2) is 0.22, the exponential coefficient of tolerance for each term is 0.96 for X^*, 0.91 for W, 0.92 for T^*, 0.93 for R_{ed} and 0.95 for F_o. The scattered points far away from the correlation line, in this figure, occur for frost mass concentration (less than 0.045 kg/m^2) with a large frost thickness (larger than 1.52 mm) under the condition of test surface temperature -15 °C and short time duration (15 minutes). Thus, this correlation should not be applied for frost properties with such a combination of frost mass concentration and frost thickness.

It should be recalled that the frost thickness ratio, δ_f/δ_{ice}, is proportional to δ_f/m_f, therefore, Eq. (5.2) implies that the mass concentration, m_f, is growing faster than the frost thickness, δ_f. In order to use Eq. (5.2) to obtain the frost thickness one has to know the mass concentration. Consequently, combining Eq. (5.4) (see the correlation of frost mass concentration in next section), the dimensionless correlation of frost thickness is deduced as follows:

$$\delta_f(kg/m^3) = 0.1555(X^*)^{-0.098}(W)^{1.723}(T^*)^{1.10}(R_{ed})^{0.343}(F_o)^{0.655} \qquad (5.3)$$

From the definition of each independent parameter, it clearly follows that the dimensionless position ratio, X^*, varies directly with the distance from the leading edge, x, the dimensionless temperature, T^*, varies inversely with the test surface temperature,

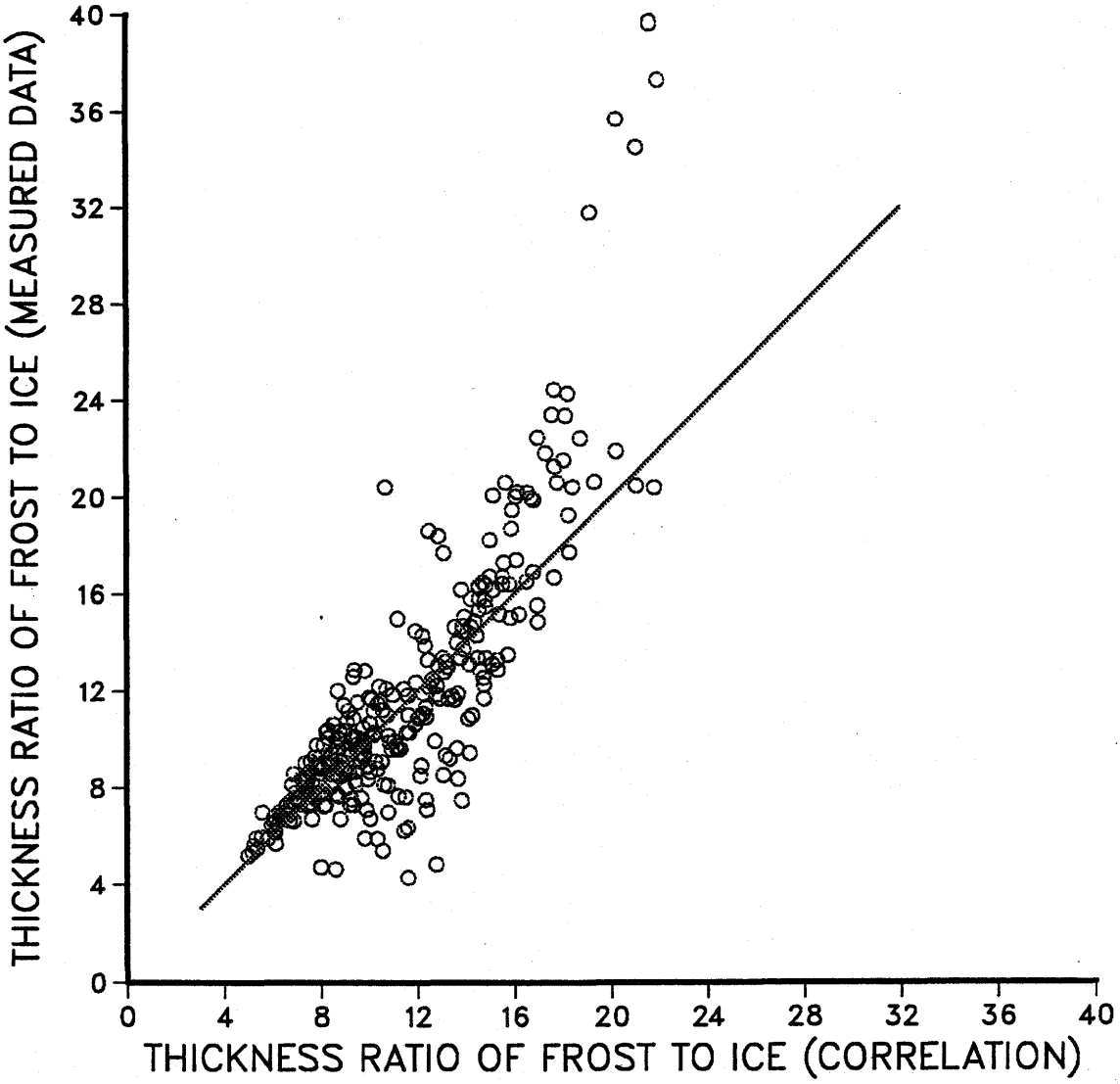

Figure 5.6 A comparison of measured data with the correlation for the dimensionless frost thickness

the Reynolds number, R_{ed}, is directly proportional to the air velocity and the Fourier number, F_o, varies directly with time. Therefore, Eq. (5.3), includes all the independent parameters shown in Figures 5.1 to 5.5, except that these parameters are dimensionless in the equation, i.e. the frost thickness varies directly with the air humidity and velocity, and time, inversely with distance from the leading edge on the test plate and the test surface temperature.

5.2. Frost Mass Concentration

The frost mass concentration on the surface is measured from the total mass of porous ice crystals on a test disk per unit area. As shown in Figure 5.7 the frost mass concentration increases with time and decreases with the distance from the leading edge. In addition, Figure 5.8 shows that the mass concentration increases with increasing air humidity ratio, while Figure 5.9 shows that the mass concentration increases slightly as the average test surface temperature decreases. Figure 5.10 shows that the mass concentration increases with increasing inlet air speed or Reynolds number and humidity ratio (see data for R_{ed}=4000). This result is in agreement with the literature where the mass concentration, averaged over the entire test plate, increases with increasing air velocity (Abdel-wahed et al. 1984; and Senshu et al. 1990). Also, Senshu et al. (1990) showed that the average plate mass concentration increases when the mean refrigerant temperature decreases.

Using the experimental data, a correlation for the frost mass concentration was obtained; this is given by Eq. (5.4):

$$m_f=7.63\times10^{-4}(X^*)^{-0.230}(W)^{1.318}(T^*)^{0.083}(R_{ed})^{1.0635}(F_o)^{0.908} \qquad (5.4)$$

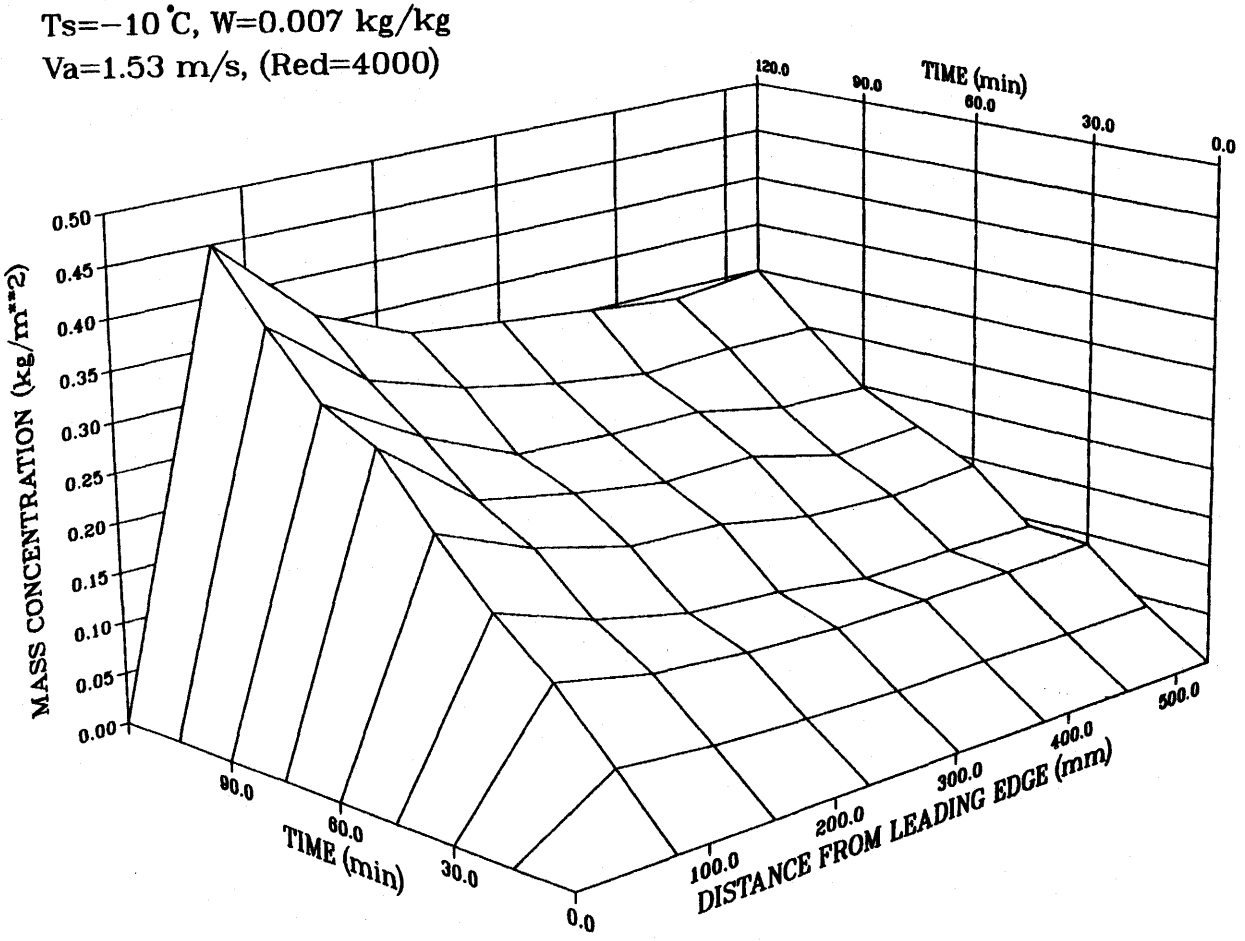

Figure 5.7 Frost mass concentration versus time and position

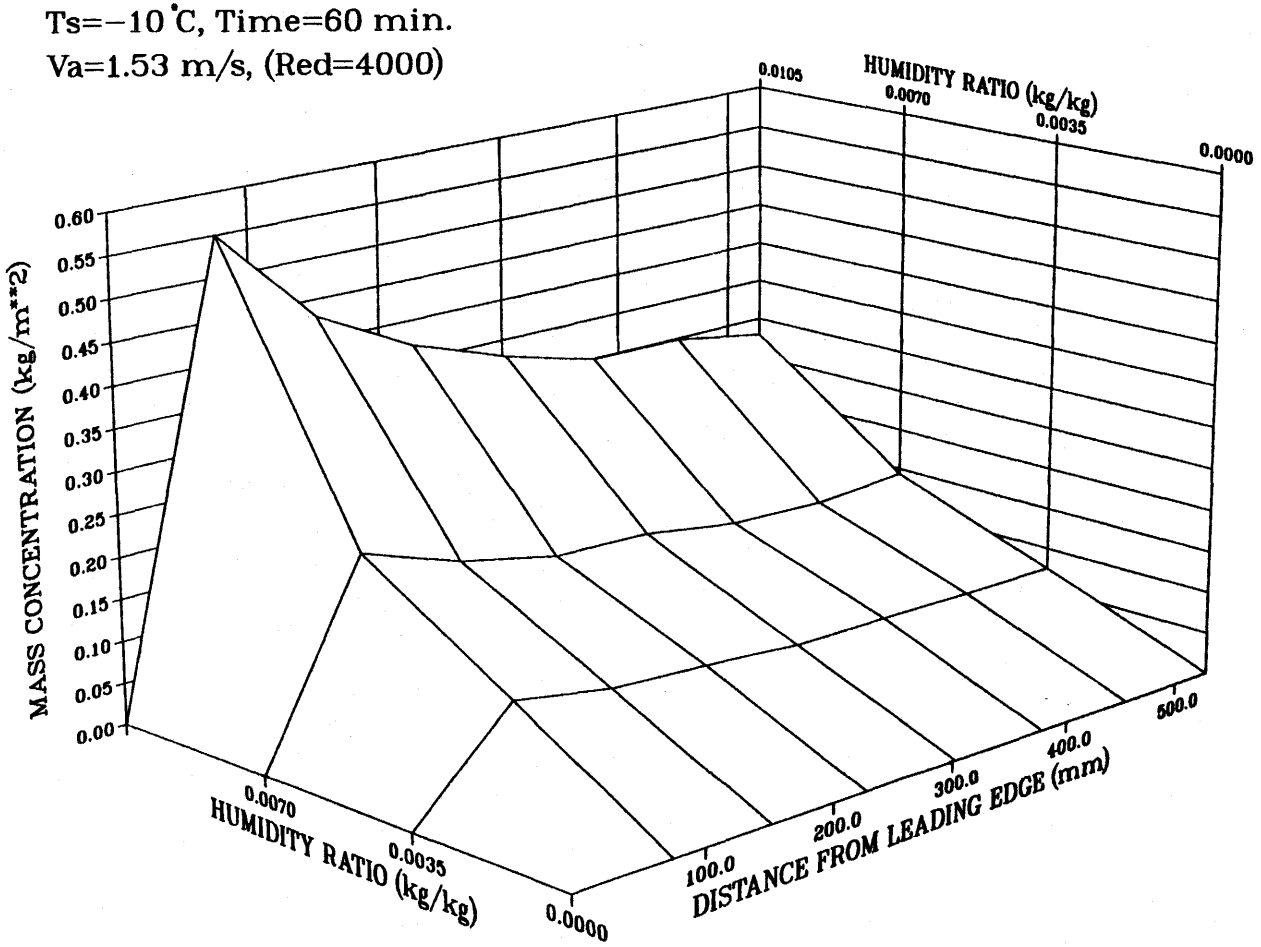

Figure 5.8 Frost mass concentration versus air humidity ratio and position

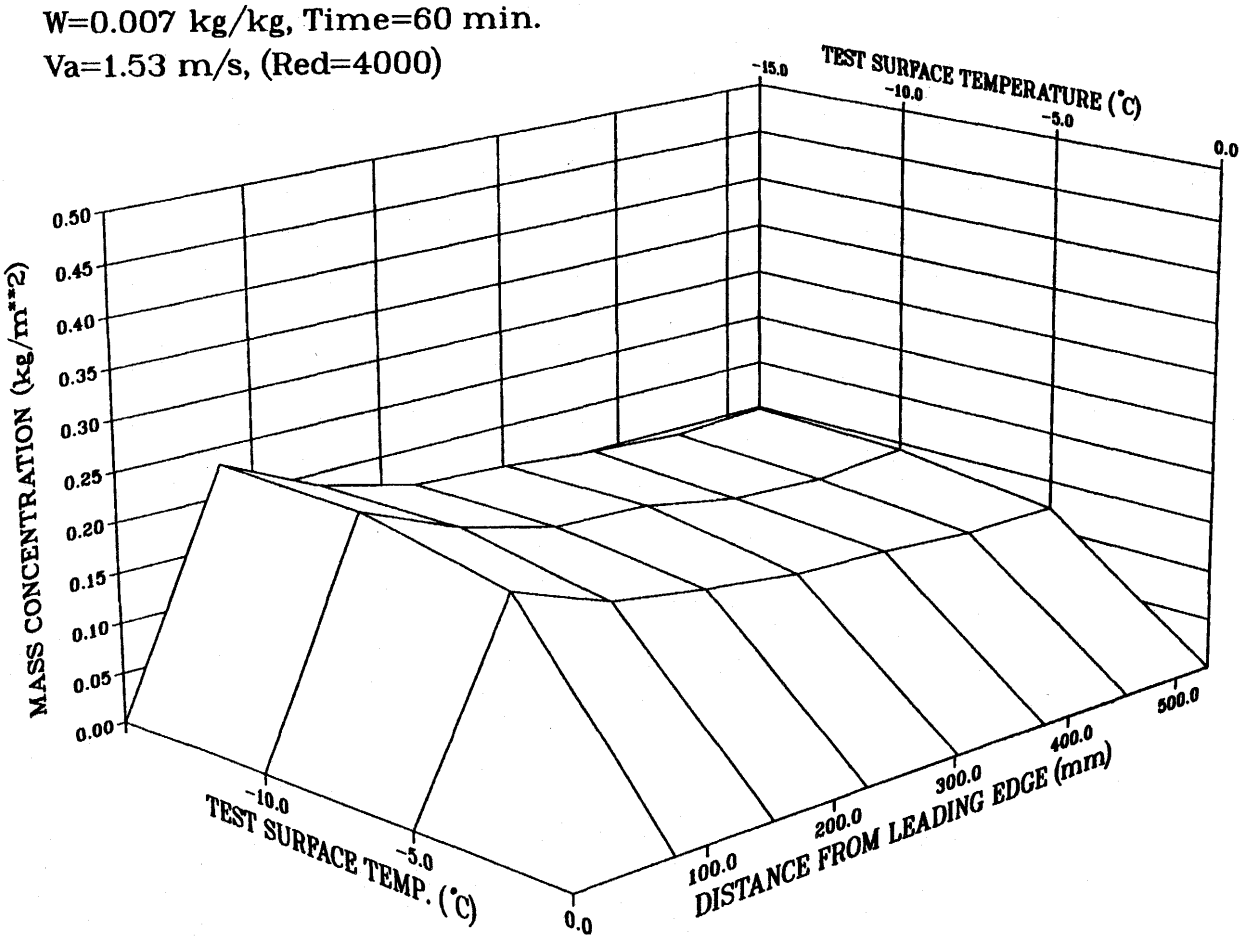

Figure 5.9 Frost mass concentration versus test surface temperature and position

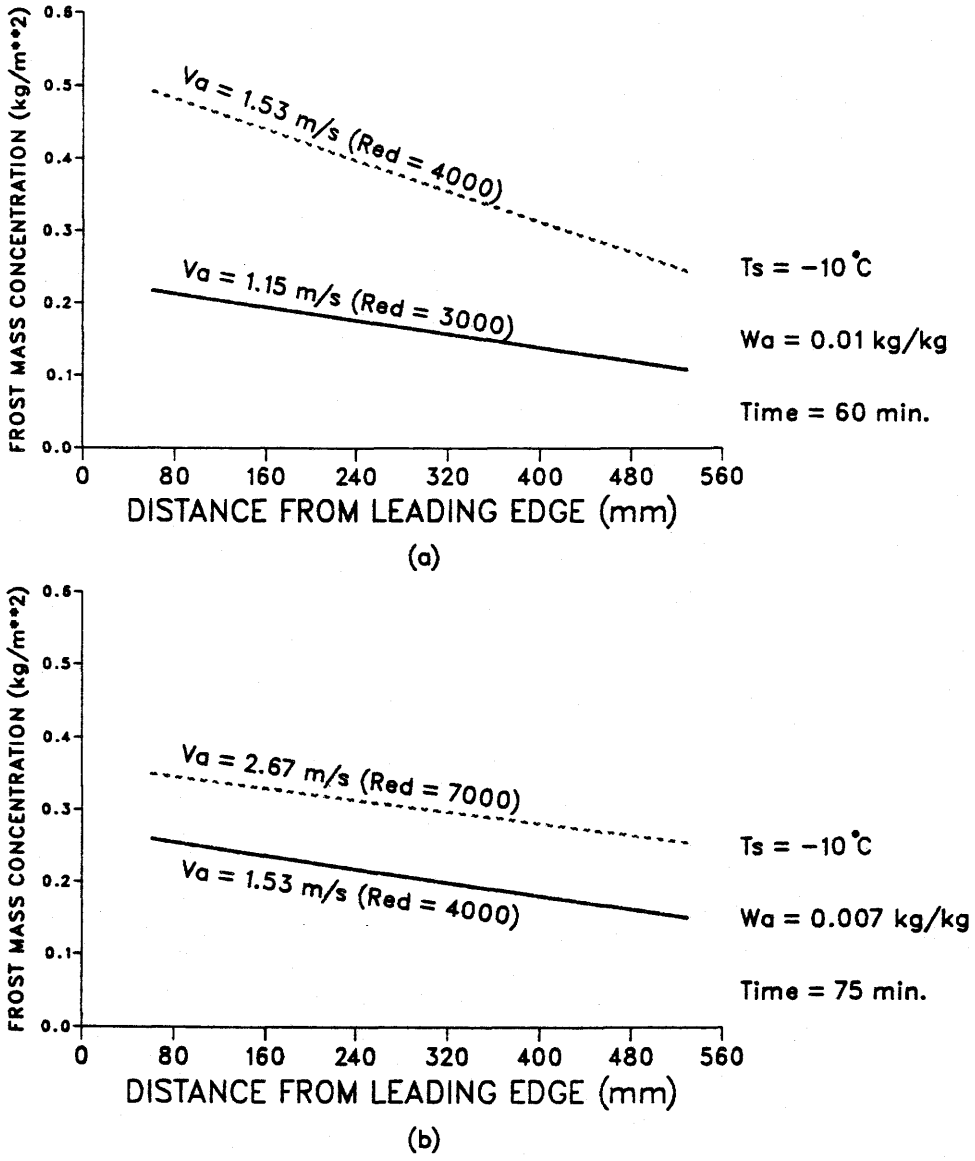

Figure 5.10 Frost mass concentration versus position with inlet air velocity or Reynolds number as a parameter

where: m_f is local frost mass concentration in kg/m^2. That is, except for m_f, (kg/m^2), all the independent parameters in Eq. (5.4) are dimensionless.

Figure 5.11 shows a comparison between the measured data of frost mass concentration and the correlation, Eq. (5.4). The root mean square error of Eq. (5.4) is 0.13, the exponential coefficient of tolerance for each term is 0.96 for X^*, 0.91 for W, 0.92 for T^*, 0.93 for R_{ed} and 0.95 for F_o.

5.3. Frost Density

The frost density is defined, as is common in the literature, to be the ratio of the frost mass concentration, m_f, divided by the frost thickness, δ_f. Figure 5.12 shows the variation of frost density with time and distance from the leading edge. The density increase during the initial period is similar to that reported by Yamakaua et al. (1952), Sanders (1974), Jones et al. (1975) and O'Neal et al. (1984) for plate average frost density. Our results show that during the initial period, the frost density is nearly uniform over the entire plate. However, as time increases, the decrease in the frost density from the leading edge is more substantial.

Figure 5.13 shows the influence of increasing the air humidity ratio on the frost density. As can be seen, the frost density strongly decreases with increasing humidity ratio from 0.004 to 0.007, and slightly increases from the leading edge to the rear area, then turns to decreases slightly at the tail edge with humidity ratio increasing from 0.007 to 0.01. Also the frost density increases with increasing average test surface temperature as shown in Figure 5.14. The same trends for frost density as a function of average test

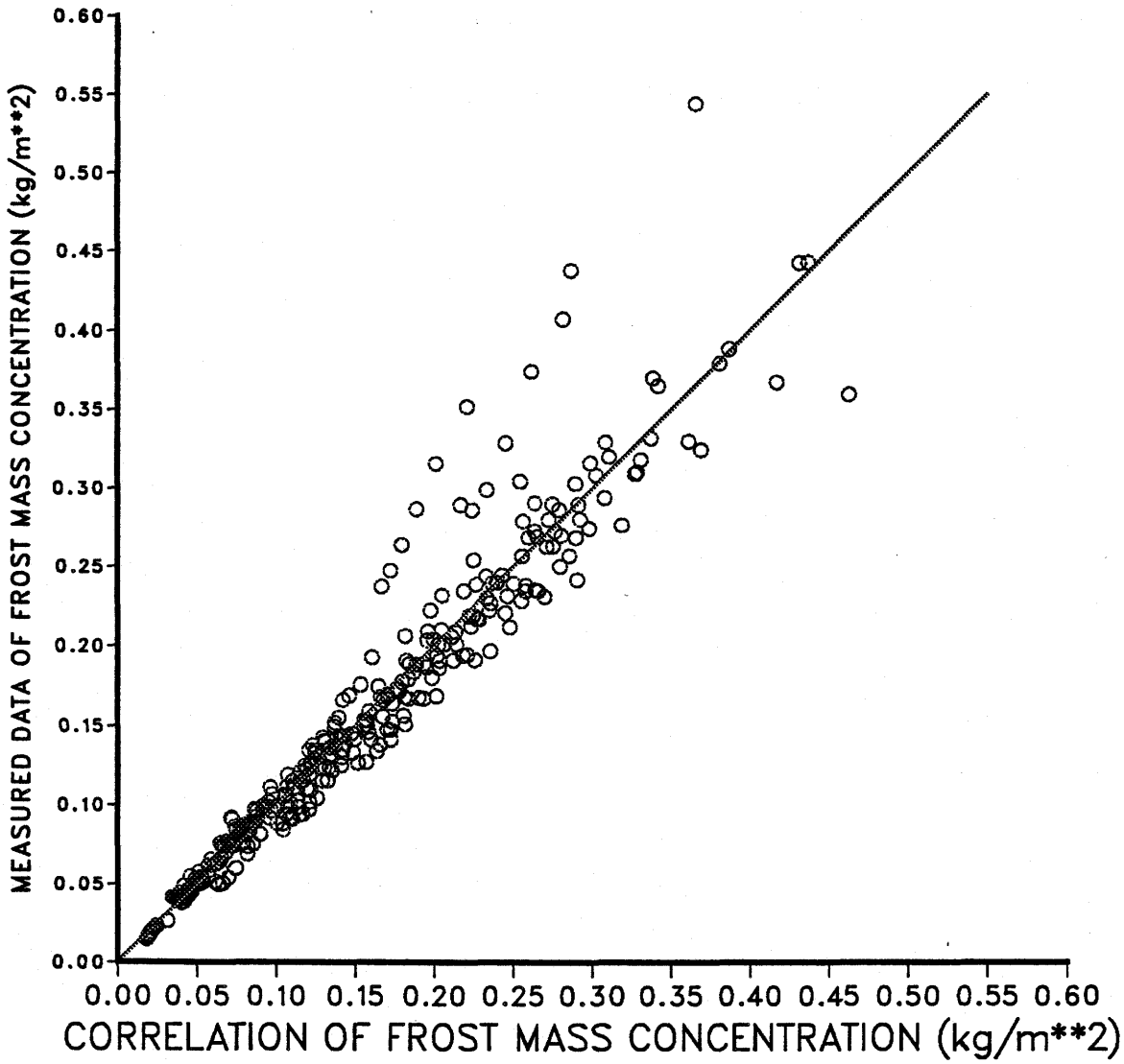

Figure 5.11 A comparison of measured data and the correlation for frost mass concentration

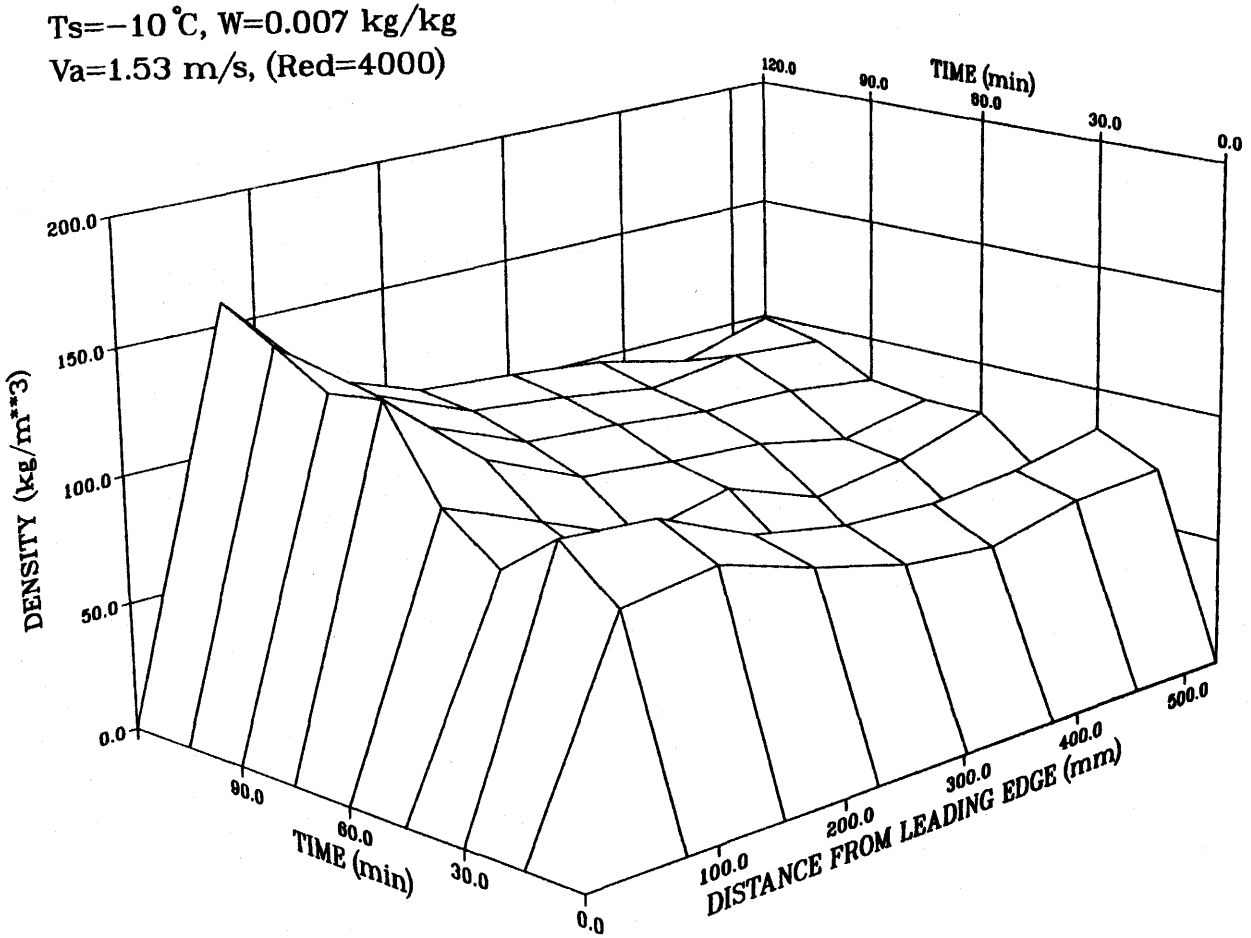

Figure 5.12 Frost density versus time and position

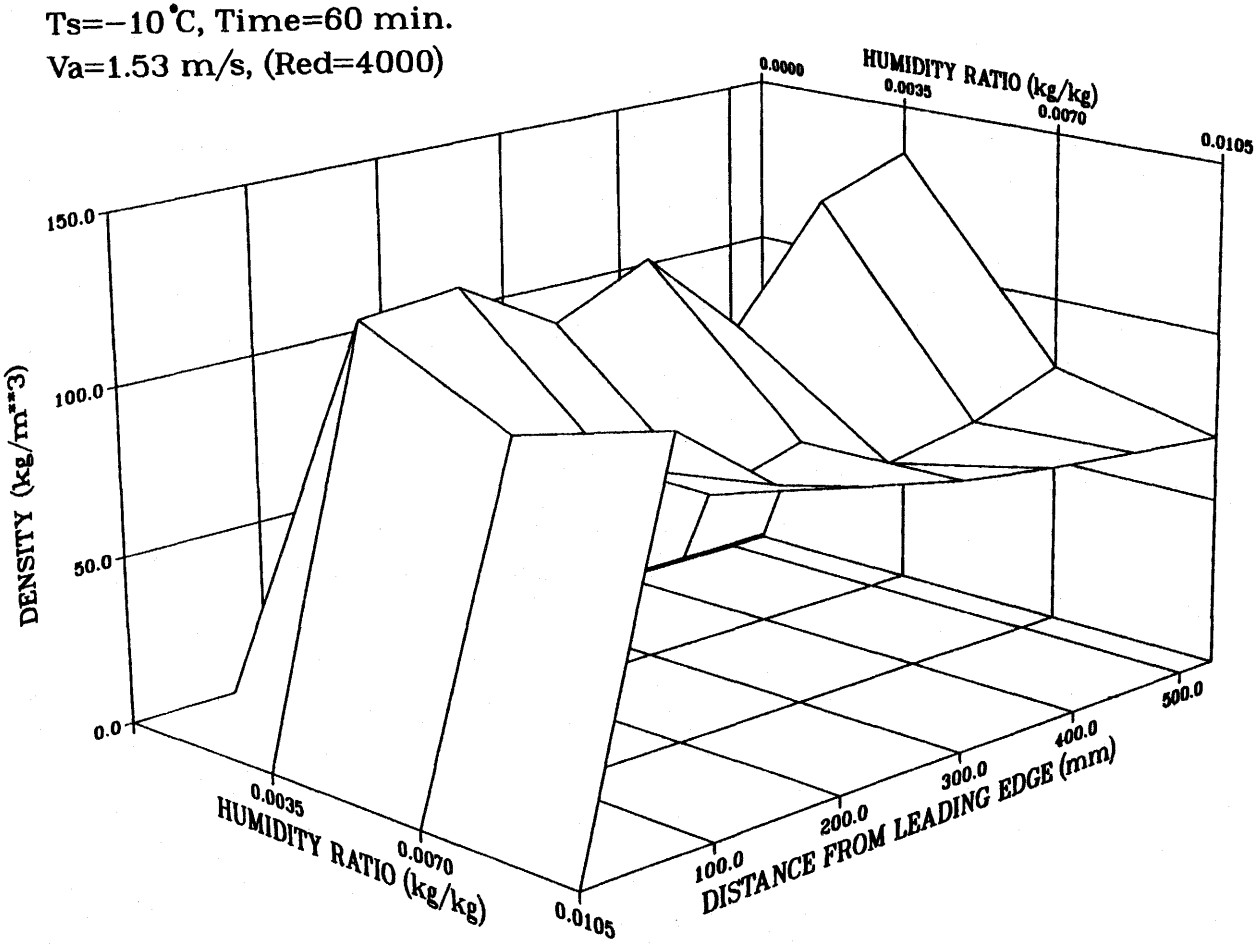

Figure 5.13 Frost density versus air humidity ratio and position

surface temperature were reported by Tokura et al. (1988) for the plate average frost density.

The frost density is also a function of the inlet air velocity. Figure 5.15 shows the frost density increases with increasing inlet Reynolds number. This result is similar to that reported by Schneider (1972) and O'Neal et al. (1984) for the plate average frost density. Furthermore, Figure 5.15, which shows that the frost density decreases with distance from the leading edge, is similar to the result shown earlier in Figure 5.12.

Eq. (5.5) is the correlation of the frost density ratio or ice crystal volume fraction with the previously mentioned dimensionless parameters:

$$\frac{\rho_f}{\rho_i}=5.559\times10^{-6}(X^*)^{-0.137}(W)^{-0.413}(T^*)^{-0.997}(R_{ed})^{0.715}(F_o)^{0.252} \qquad (5.5)$$

where:

$\frac{\rho_f}{\rho_i}$ =Dimensionless frost density or volume fraction of ice crystals

ρ_f Local frost density (kg/m^3)

ρ_i Ice density, 920 (kg/m^3) at 0°C

A comparison between the measured and computed data of dimensionless frost density with the correlation, Eq. (5.5), is shown in Figure 5.16. The root mean square error of Eq. (5.5) is 0.22, the exponential coefficient of tolerance for each term is 0.96 for X^*, 0.91 for W, 0.92 for T^*, 0.93 for R_{ed} and 0.95 for F_o.

Eq. (5.5) shows the frost density is inversely proportional to distance from the leading edge and air humidity, and directly proportional to the average test surface temperature, air velocity and time. This equation includes all the results presented in Figures 5.12 to 5.15.

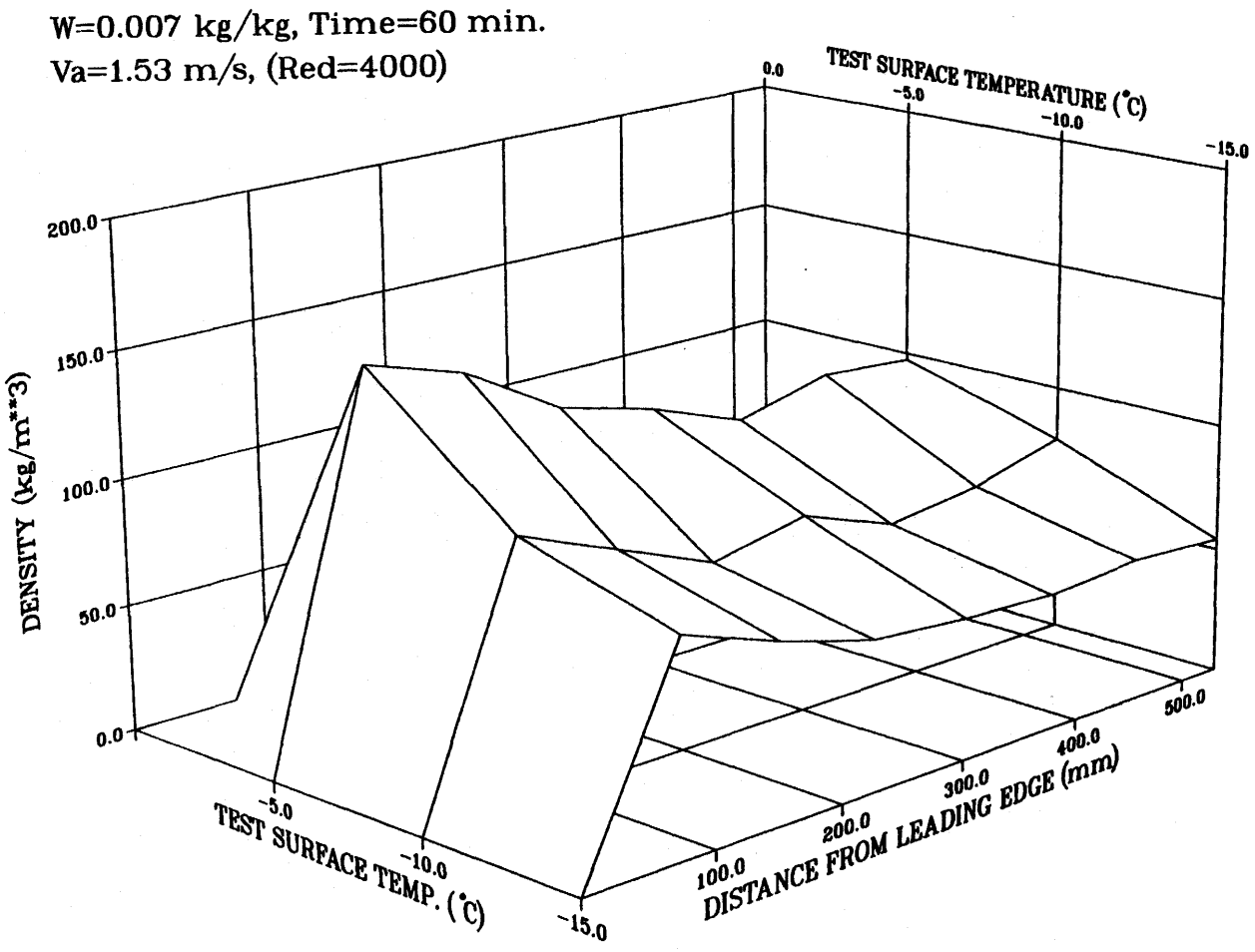

Figure 5.14 Frost density versus test surface temperature and position

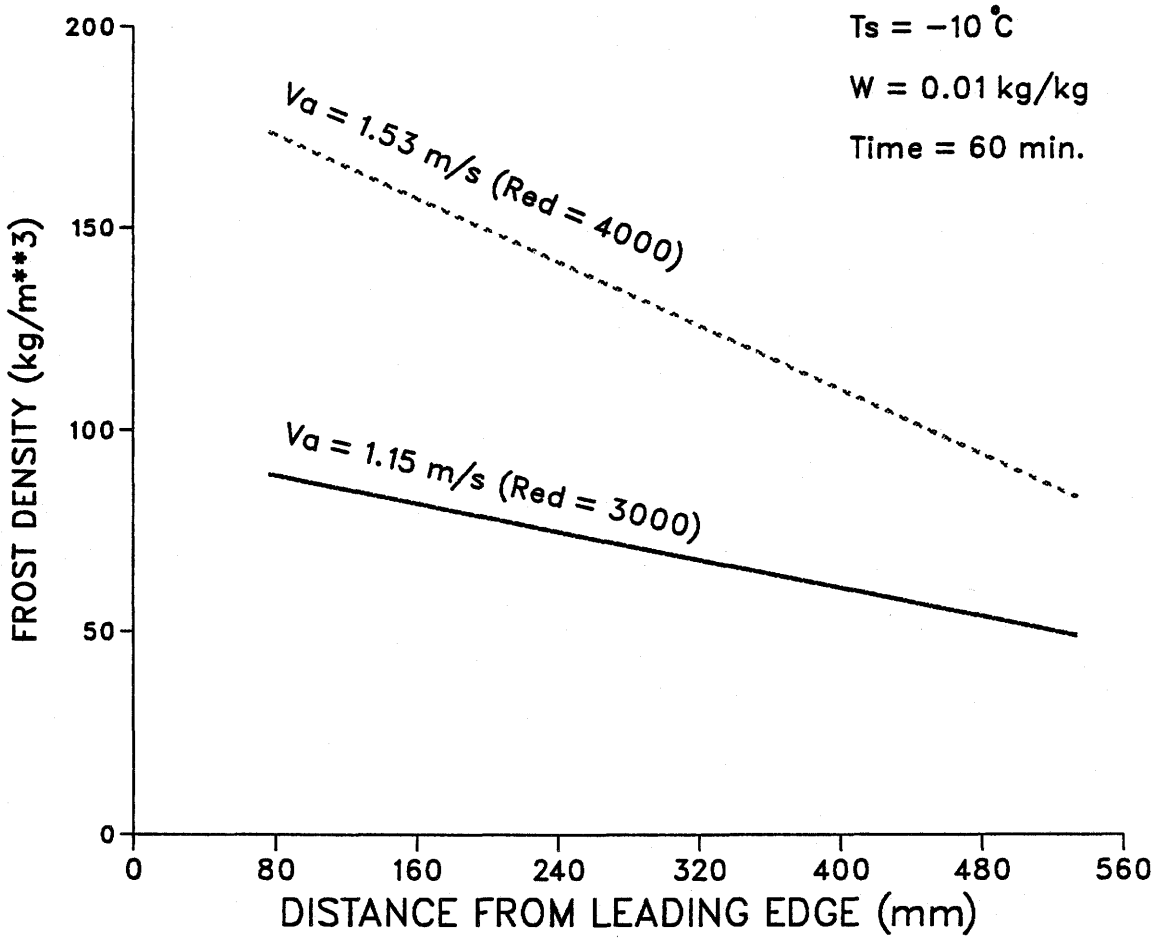

Figure 5.15 Frost density versus position with inlet air velocity or Reynolds number as a parameter

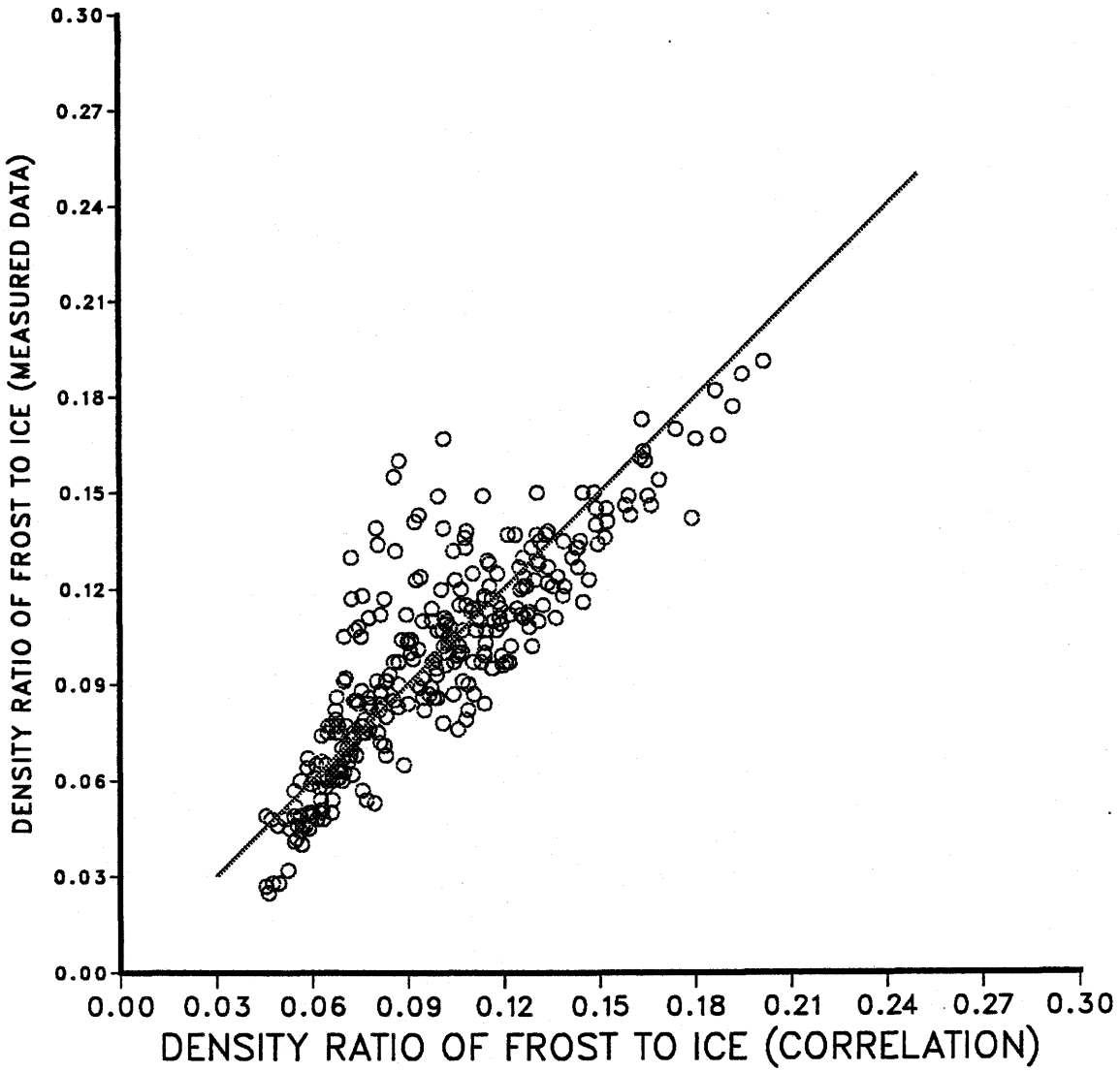

Figure 5.16 A comparison of measured data with the correlation of frost density ratio

It should be noted that the frost thickness ratio, δ_f/δ_{ice}, is the exact inverse of the density ratio, ρ_f/ρ_{ice}; therefore, the correlation Eq. 5.2 should be the inverse of 5.5. Within the accuracy of the correlation, this is indeed the case.

The correlation can be used to create three dimensional plots of frost density ratio versus the other dimensionless variables or the same plot can be presented with dimensional variables. For example, Figure 5.17 shows the density versus time and position on the test surface in a plot similar to Figure 5.12. In this case the surface is smooth with no irregularities such as are evident in Figure 5.12. These irregularities are primarily a consequence of experimental uncertainties.

5.4. Frost Thermal Conductivity

For most solids the heat flux is proportional to the temperature gradient. The constant of proportionality is the thermal conductivity. For porous materials, however, heat may be transferred in the porous medium by conduction, convection and radiation. For porous materials of large thickness relative to the pore size, the apparent thermal conductivity is defined as the steady heat flux divided by the temperature difference across the porous medium and multiplied by the thickness of the material. In the case of frost, a porous medium with a density ratio between 0.03 and 0.24, two additional problems exist when attempting to define its thermal conductivity: the release of latent heat where water vapour forms ice crystals in the frost layer. This causes the temperature in the frost layer to be higher and non-linear with distance from the cold plate. Secondly, the interface temperature between the frost and air is not measured because all attempts to obtain an accurate temperature of this interface have been unsuccessful. In spite of its

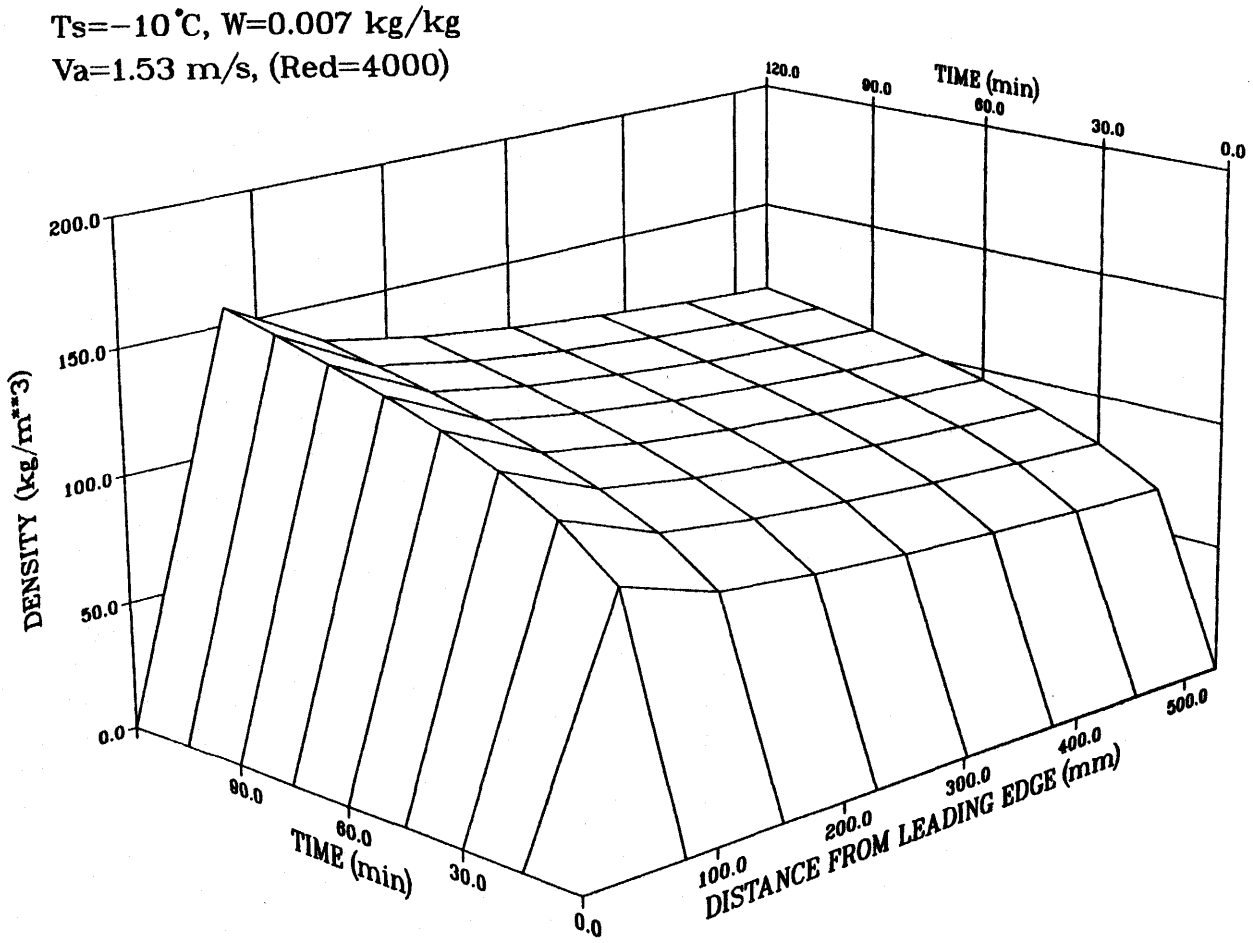

Figure 5.17 Frost density computed using Eq.(5.5) versus time and position

inaccuracy, the thermal conductivity of the frost layer has been assumed by many researchers to be the same as that for a porous medium. Also, the surface temperature of the frost is assumed to be 0 °C, since no other alternative is available at this time. Using this definition, we get:

$$k_f = \frac{q'' \cdot \delta_f}{(0 - T_{ts})} \tag{5.6}$$

where:

k_f Frost thermal conductivity (W/m·K)

q'' Total heat flux (W/m^2)

Figure 5.18 shows the frost thermal conductivity versus time and distance from the leading edge. From this figure the thermal conductivity increases with time and decreases with distance from the leading edge on the test plate. The frost thermal conductivity increases with increasing the air humidity ratio, as shown in Figure 5.19, which is similar to the results reported by other researchers.

The result, shown in Figure 5.20 is similar to that reported by Yonko et al. (1967); the frost thermal conductivity increases slightly with a decreasing average test surface temperature. Also, the frost thermal conductivity increases with the inlet Reynolds number; as shown in Figure 5.21.

Similar to the analysis of frost thickness and density, a dimensionless correlation was obtained for the local frost thermal conductivity:

$$\frac{k_f}{k_i} = 0.011 (X^*)^{-0.370} (W)^{2.044} (T^*)^{0.216} (R_{ed})^{1.093} (F_o)^{0.699} \tag{5.7}$$

where:

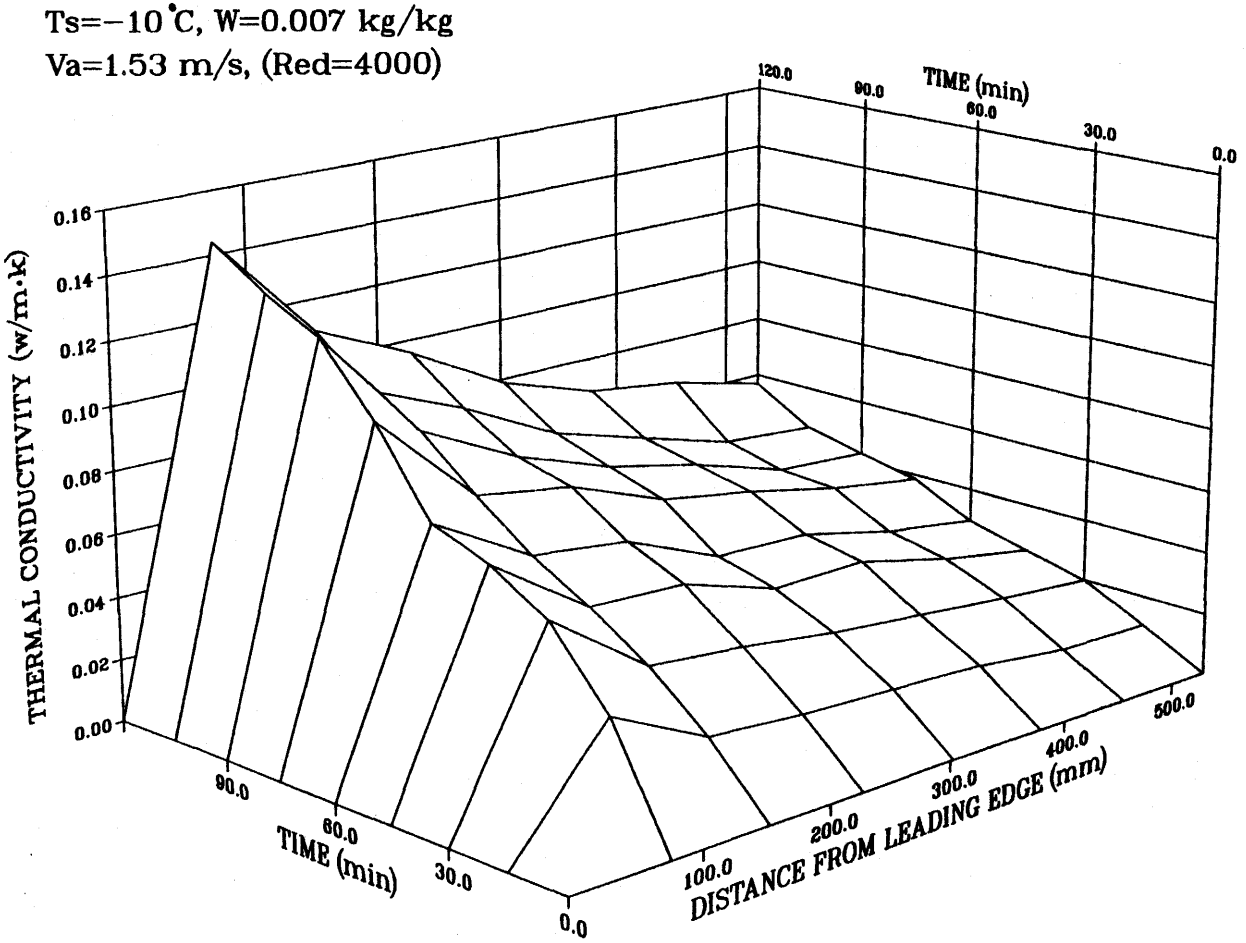

Figure 5.18 Frost thermal conductivity versus time and position

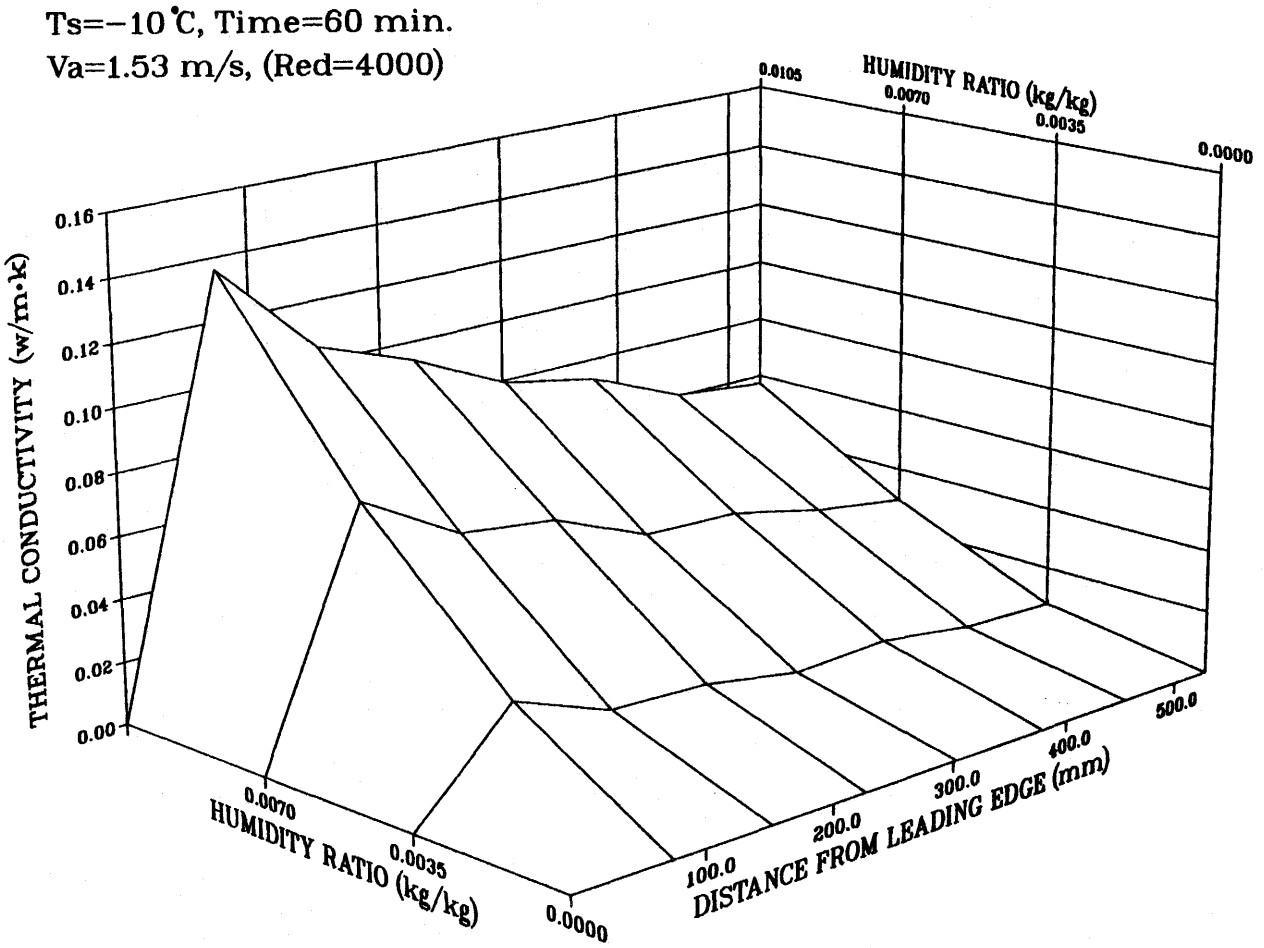

Figure 5.19 Frost thermal conductivity versus air humidity ratio and position

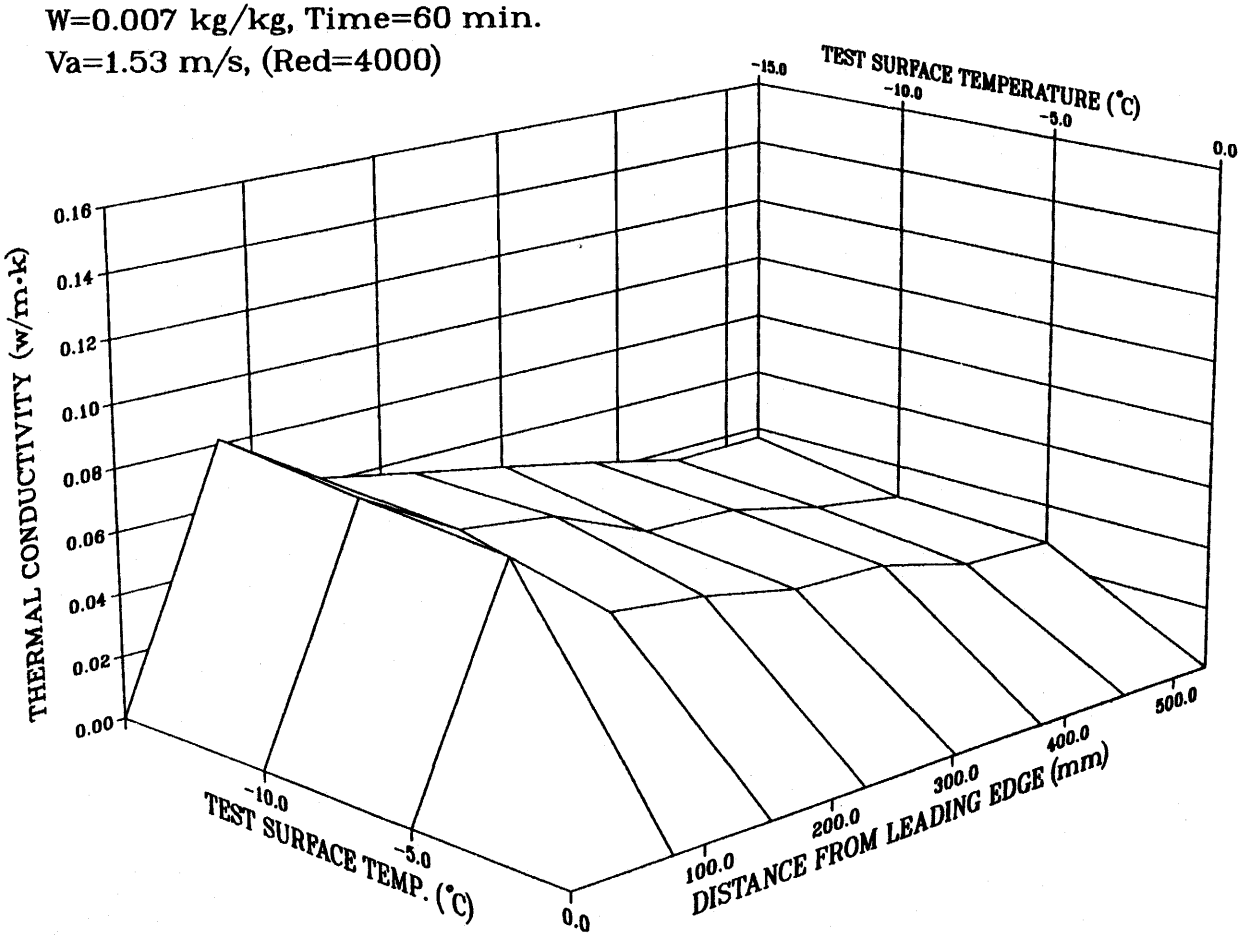

Figure 5.20 Frost thermal conductivity versus test surface temperature and position

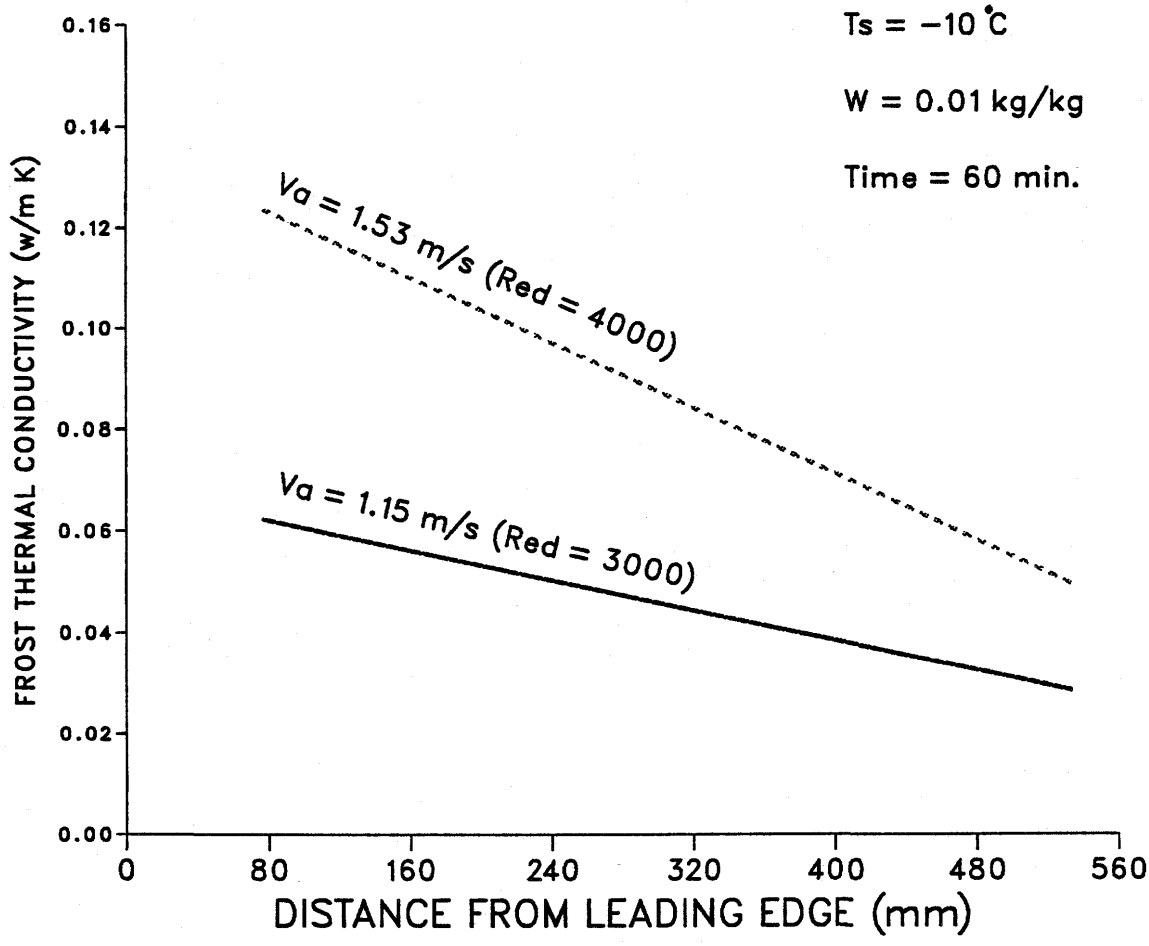

Figure 5.21 Frost thermal conductivity versus position with inlet air velocity or Reynolds number as a parameter

$\frac{k_f}{k_i}$ Dimensionless frost thermal conductivity

k_i Thermal conductivity of ice, 1.88 (W/m·K) at 0°C

Figure 5.22 shows a comparison between the measured and computed data with the correlation, Eq. (5.7). The root mean square error of Eq. (5.7) is 0.24, the exponential coefficient of tolerance for each term is 0.96 for X^*, 0.91 for W, 0.92 for T^*, 0.93 for R_{ed} and 0.95 for F_o.

The exponents in Eq. (5.7) indicate that the frost thermal conductivity ratio increases rapidly with increasing air humidity ratio, air velocity and time, and with decreasing the average test surface temperature; but it decreases with distance away from the leading edge.

A number of studies in literature reported that the thermal conductivity is a function of the frost density alone (see Chapter 2), however, in this study, comparing Eq. (5.5) and Eq. (5.7), shows that frost density and thermal conductivity have different exponents with air humidity ratio and average test surface temperature.

5.5. Heat Transfer

In this section, the frost-to-air heat transfer coefficient is studied, where the frost-to-air heat transfer coefficient is obtained using the corrected heat flux, which combines the measured local normal heat flux through the heat-flux meter and amount equal to the local heat flux caused by the slightly higher temperatures near the leading edge on the test plate. Thus this is an apparent heat transfer coefficient, assuming a frost-air interface temperature of 0 °C and no phase change within the frost layer.

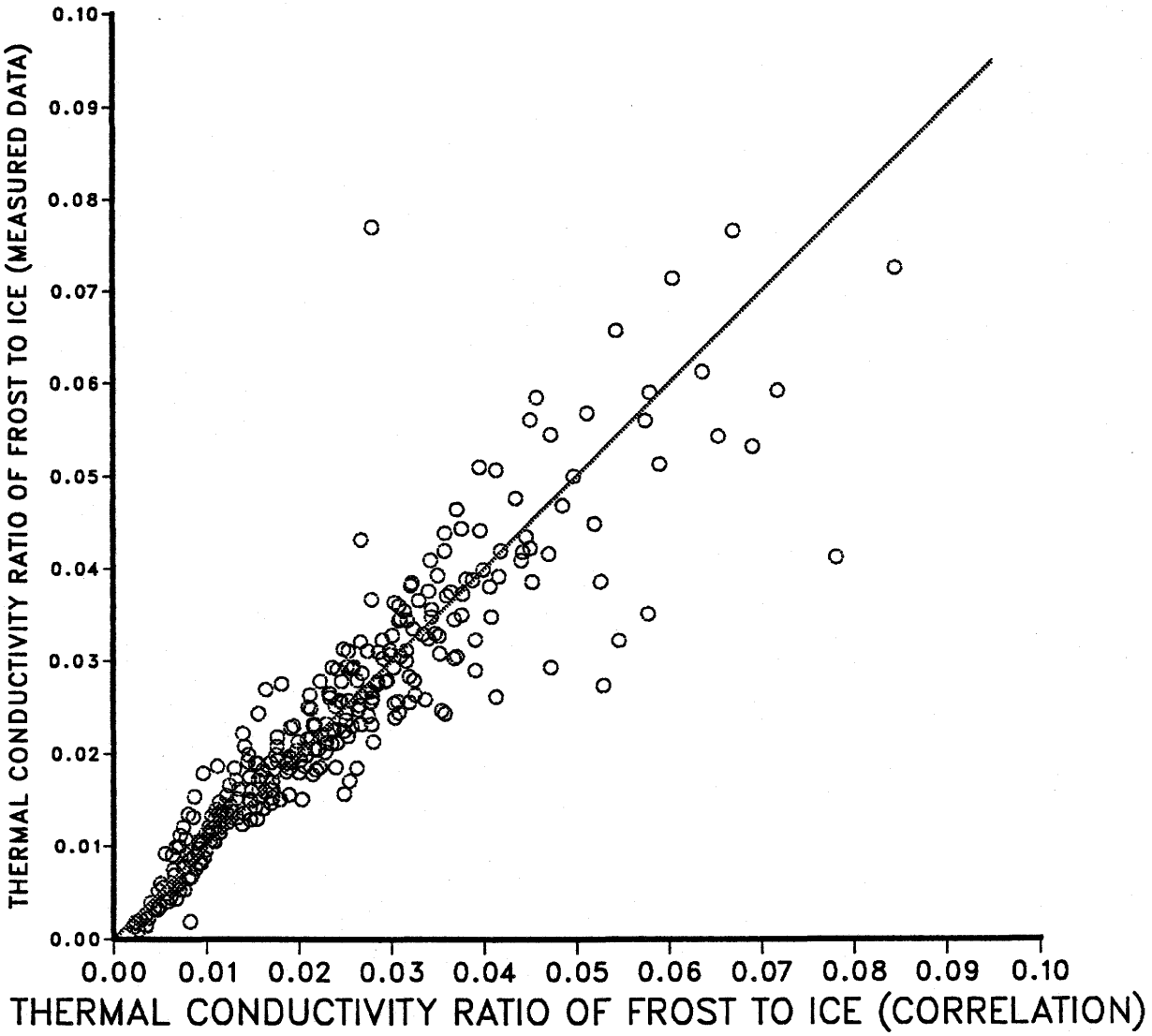

Figure 5.22 A comparison of measured and computed data with the correlation of the frost thermal conductivity

Figure 5.23 shows that the heat transfer coefficient is nearly constant with time but decreases with distance from the leading edge. Yamakawa et al. (1972) reported that their heat transfer coefficients were almost constant in time. Figure 5.24 shows the heat transfer coefficient increases slightly with the air humidity ratio. This result was also reported by Kondepudi et al. (1989). Figure 5.25 shows the heat transfer coefficient increases when the average test surface temperature decreases. In Figure 5.26, the heat transfer coefficient increases with inlet air velocity. This result is in agreement with Gates et al. (1967).

The following correlation equation was developed to predict the heat transfer coefficient, ($W/m^2 \cdot K$), over the range of test variables:

$$h_f = 0.506(X^*)^{-0.302}(W)^{0.297}(T^*)^{0.725}(R_{ed})^{0.717}(F_o)^{0.035} \tag{5.8}$$

where:

h_f Heat transfer coefficient under frost formation condition, defined by $h_f = \frac{1}{R_{sum} - R_f}$ ($W/m^2 \cdot K$)

R_{sum} Total heat transfer thermal resistance, defined by $R_{sum} = \frac{T_a - T_{ts}}{q''}$ ($m^2 \cdot K/W$)

R_f Frost thermal resistance, defined by $R_f = \frac{\delta_f}{k_f}$ ($m^2 \cdot K/W$)

A comparison between the measured data and the correlation, Eq. (5.8), is shown in Figure 5.27. The root mean square error of Eq. (5.8) is 0.11, the exponential coefficient of tolerance for each term is 0.96 for X^*, 0.91 for W, 0.92 for T^*, 0.93 for R_{ed}, and 0.95 for F_o.

A dimensionless correlation for frost to air heat transfer is given by:

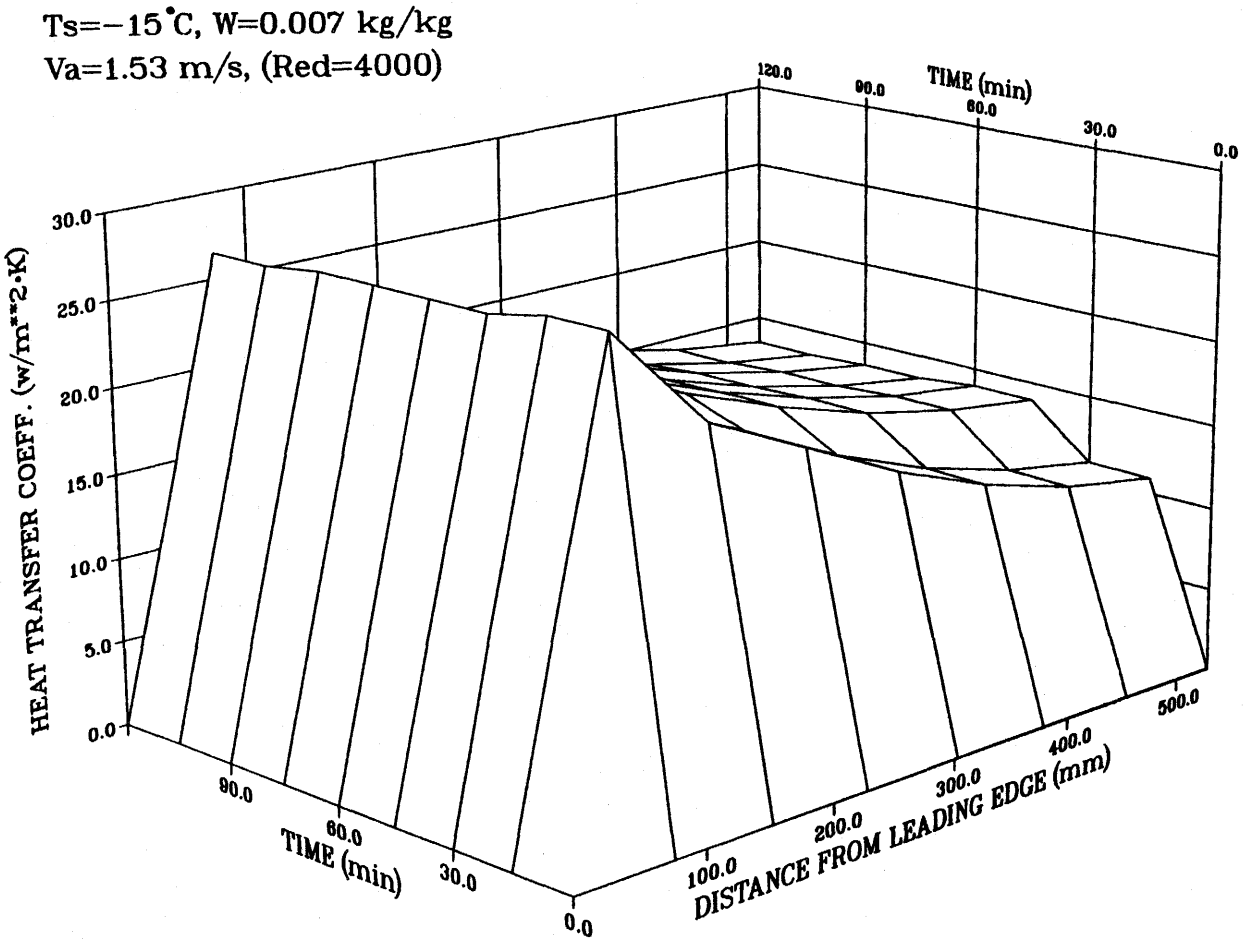

Figure 5.23 Heat transfer coefficient versus time and position

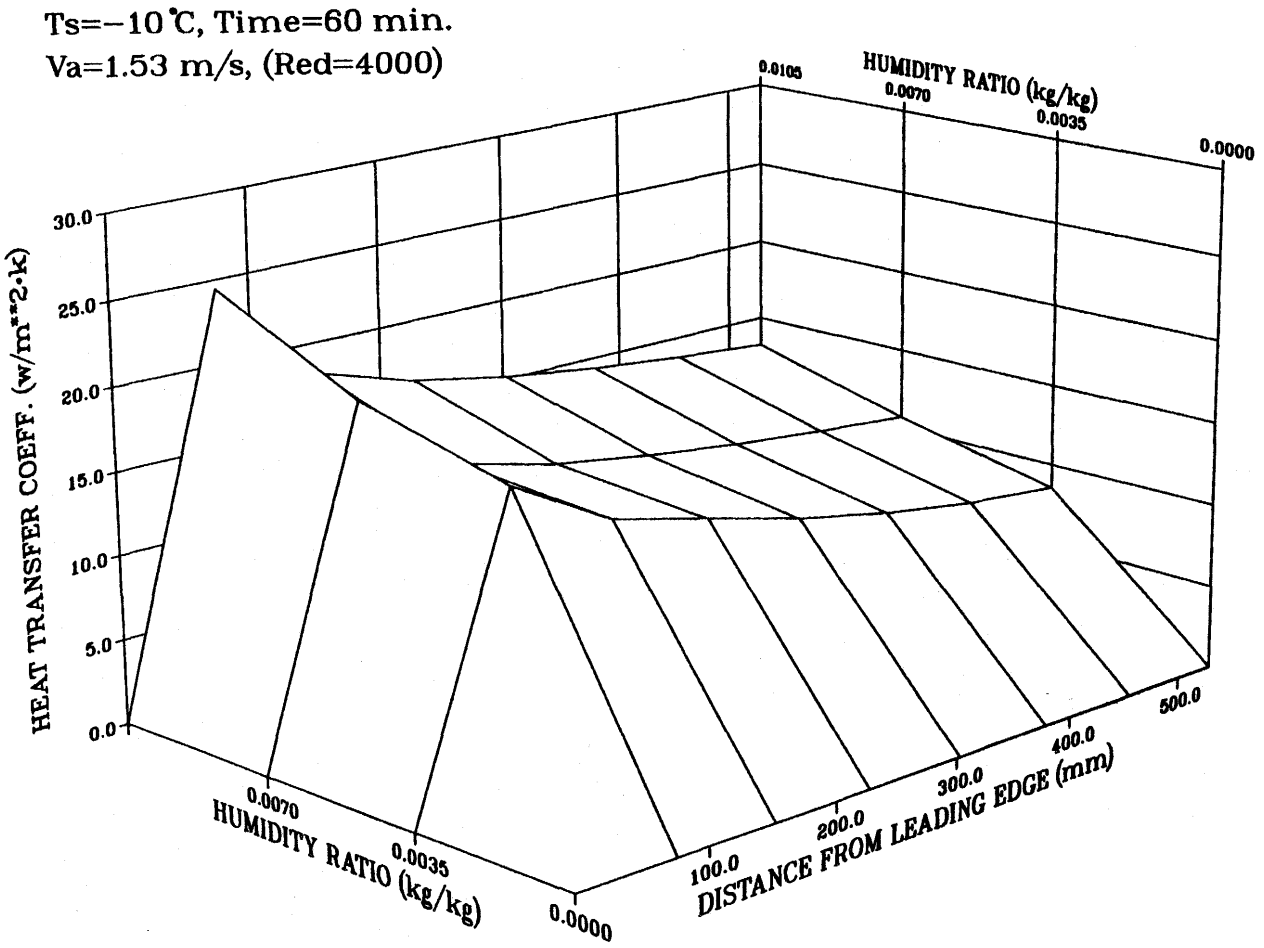

Figure 5.24 Heat transfer coefficient versus humidity ratio and position

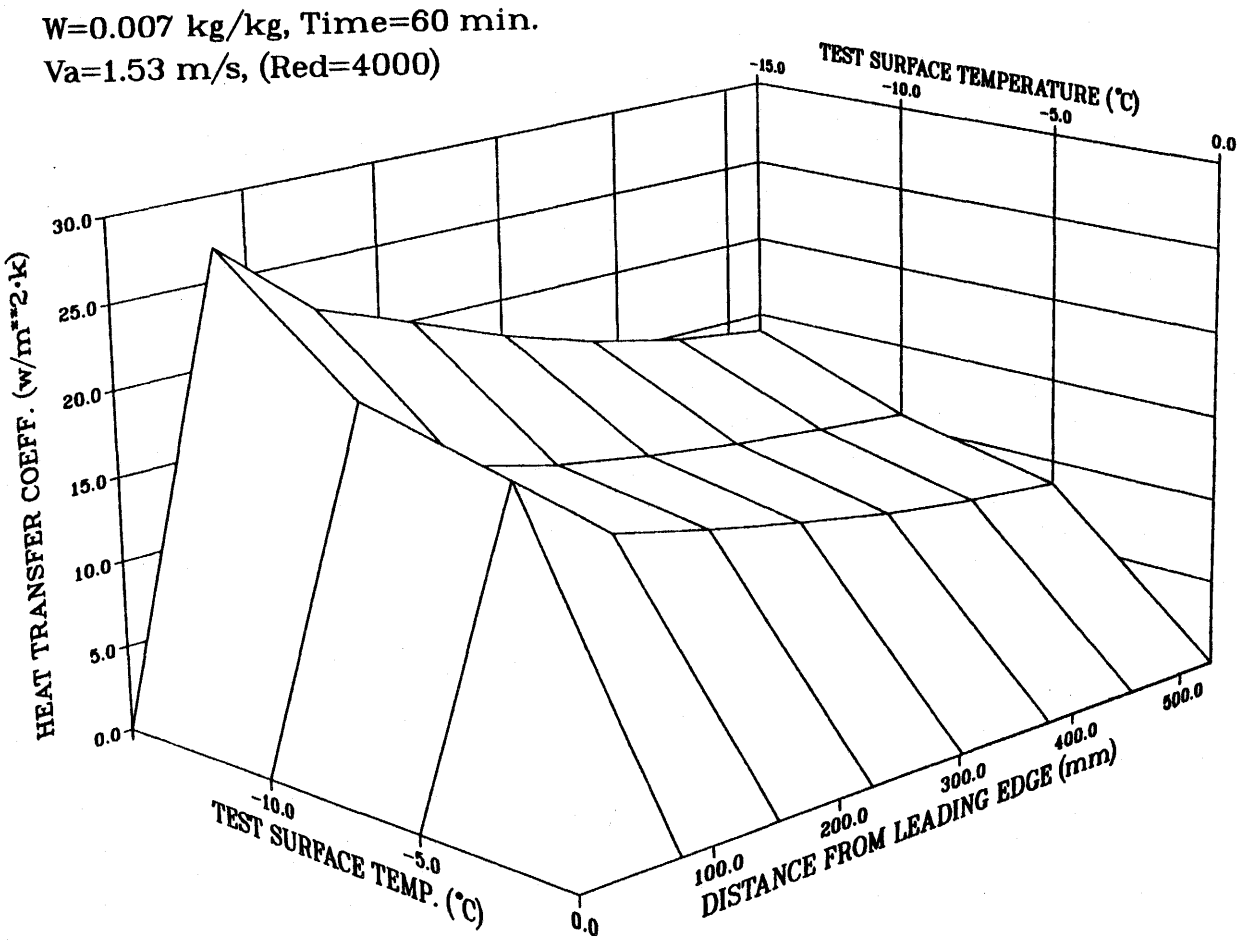

Figure 5.25 Heat transfer coefficient versus test surface temperature and position

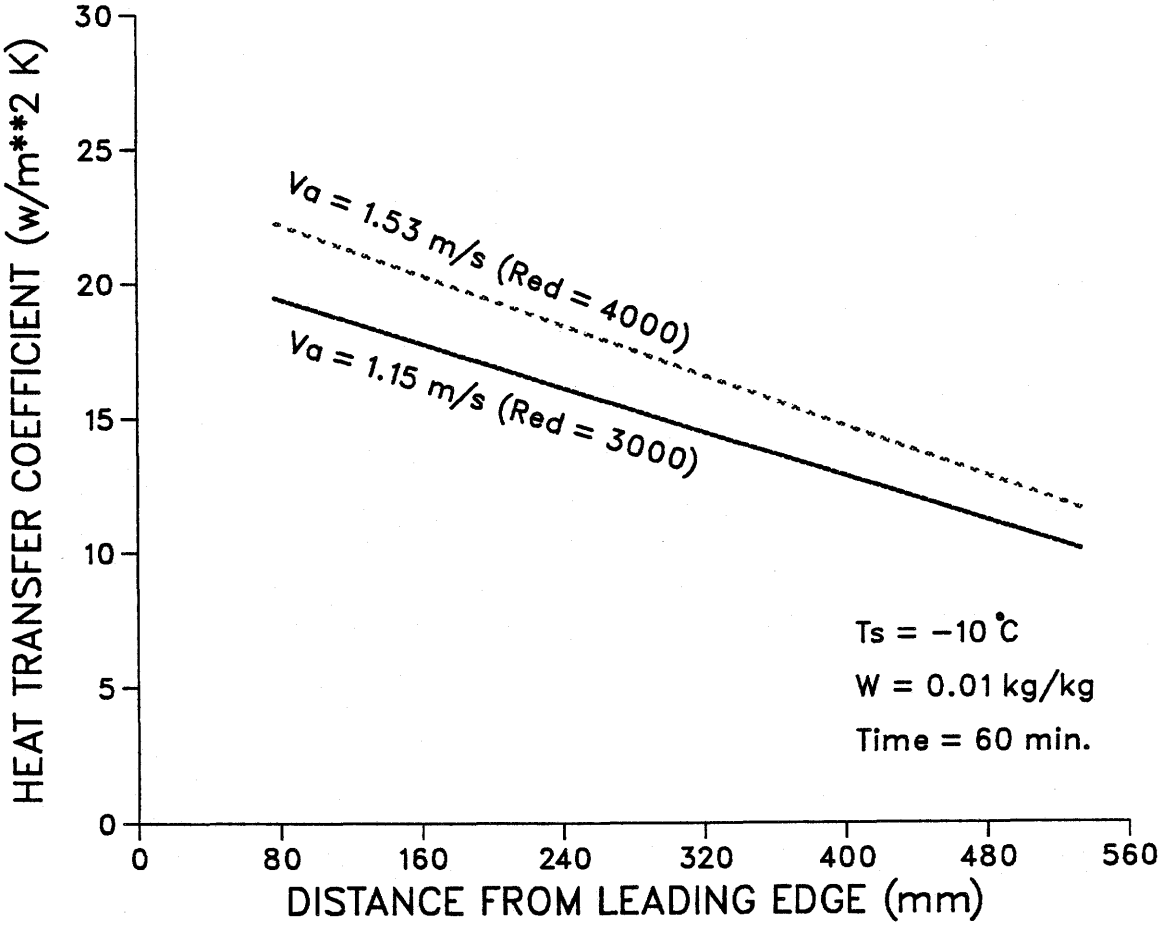

Figure 5.26 Heat transfer coefficient versus position with inlet air velocity or Reynolds number as a parameter

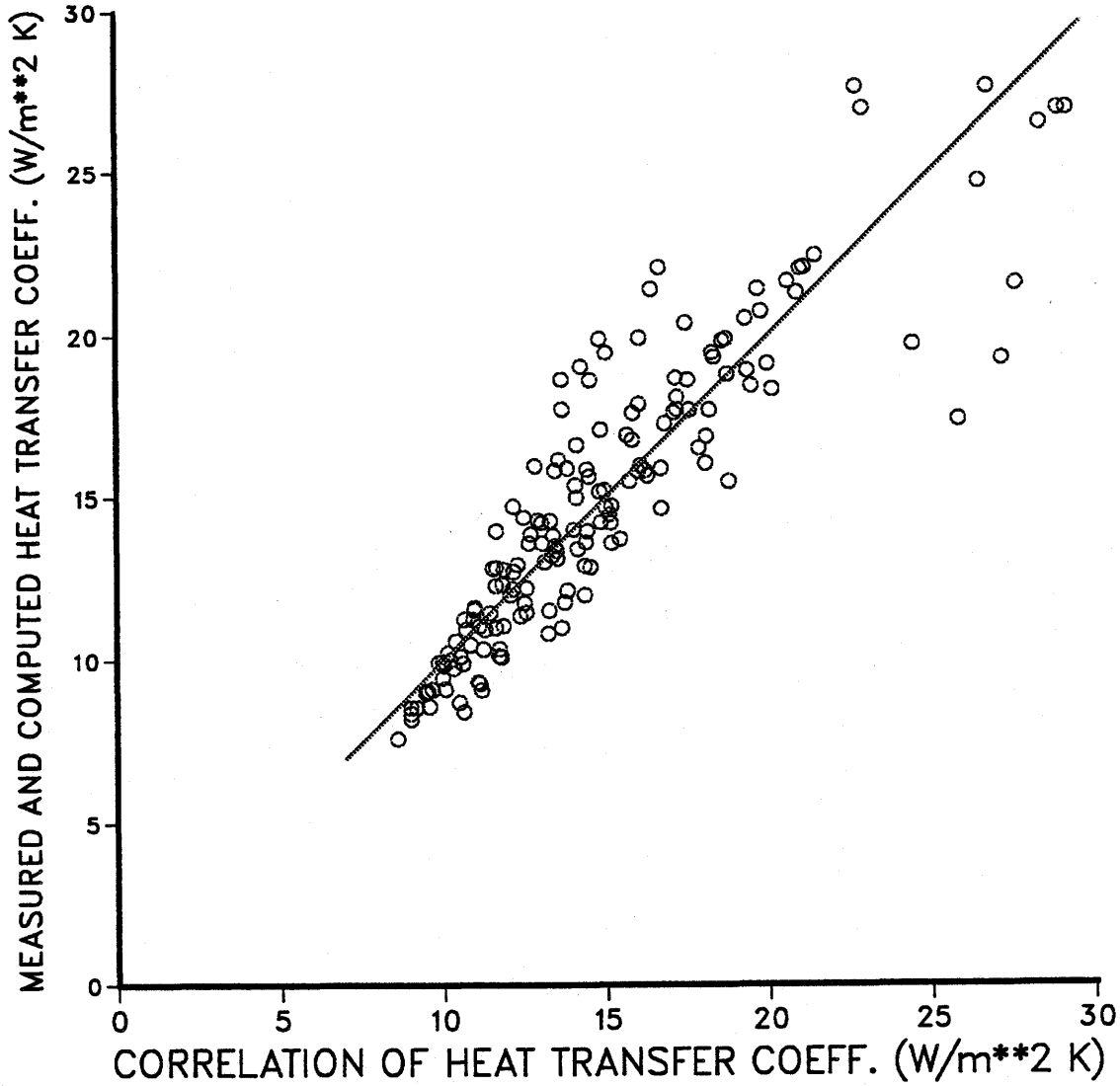

Figure 5.27 A comparison between measured and computed data and the correlation for heat transfer coefficient

$$Nu_f=0.7203(X^*)^{0.698}(W)^{0.294}(T^*)^{0.729}(R_{ed})^{0.721}(F_o)^{0.036} \quad (5.9)$$

where:

Nu_f Local Nusselt number under frost formation condition,

$Nu_f=\frac{h_f X}{k_a}$

k_a Thermal conductivity of air at the film temperature (W/m·K)

Figure 5.28 shows a comparison between the measured and computed data with the correlation, Eq. (5.9). The root mean square of Eq. (5.9) is 0.12, the exponential coefficient of tolerance for each term is 0.96 for X^*, 0.91 for W, 0.92 for T^*, 0.93 for R_{ed}, and 0.95 for F_o.

It is shown, according to Eq. (5.9), that the Nusselt number for frost to air heat transfer is in directly proportional to the distance from the leading edge of the test plate, air humidity and velocity, and time, is inversely proportional to the average test surface temperature.

5.6. Mass Transfer

Reviewing the literature, it was found that many of the investigators considered that the relationship between heat and mass transfer coefficients under frosting conditions is related through the Chilton-Colburn analogy (see Chapter 2). The mass transfer coefficient has been studied in this work and the following findings were obtained:

Figure 5.29 shows the mass transfer coefficient slightly decreasing with increasing time, and that it is higher at the leading edge than downstream along the test plate. The

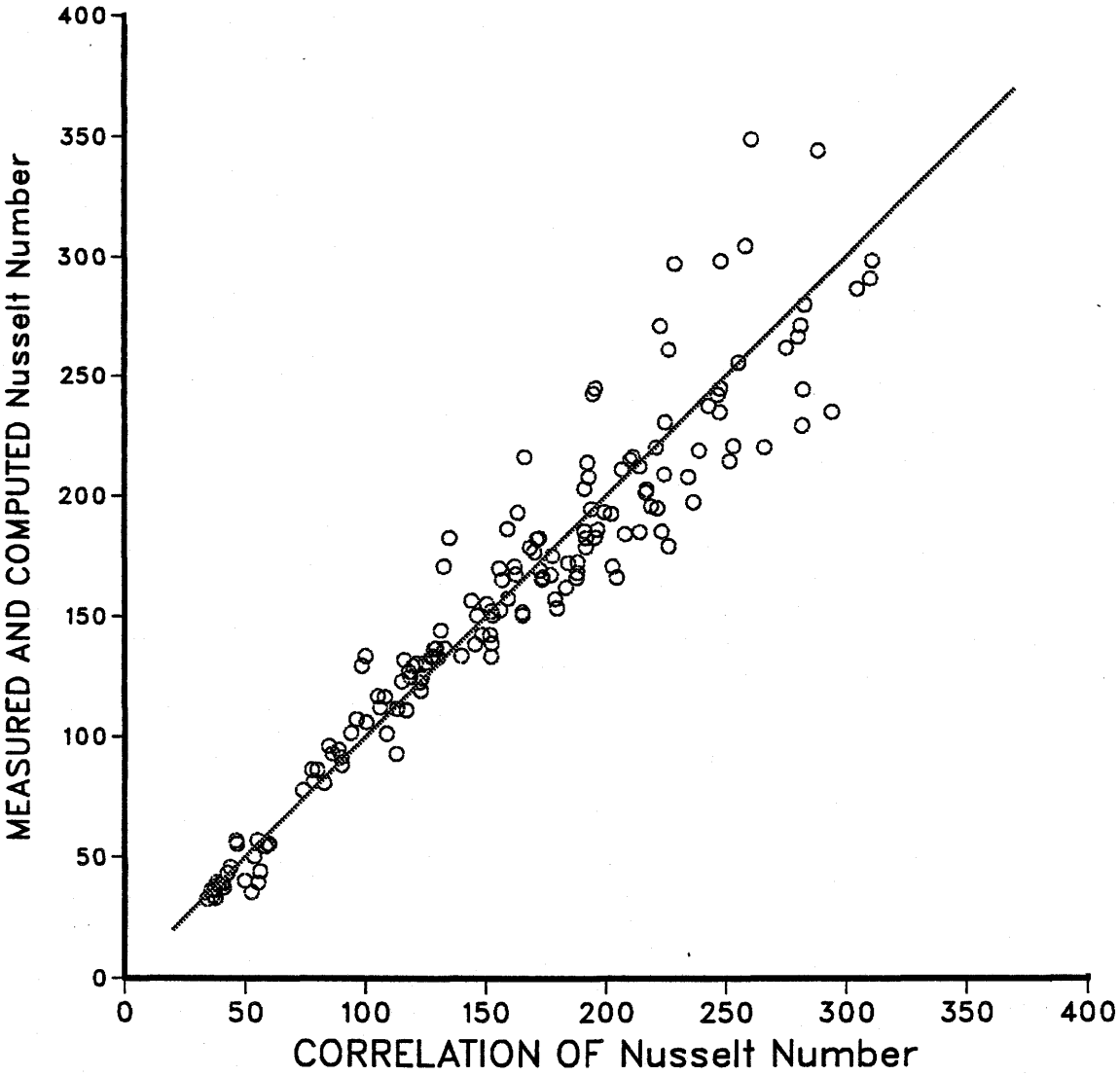

Figure 5.28 A comparison of measured and computed data with correlation of Nusselt number

results obtained indicate that the mass transfer coefficient decreases significantly with increasing the air humidity ratio from 0.004 to 0.007, and slightly decreases with air humidity ratio ranging from 0.007 to 0.01. This interesting phenomenon is shown in Figure 5.30.

The mass transfer coefficient decreases slightly with a decrease in the average test surface temperature, as shown in Figure 5.31. Figure 5.32 shows the tendency of the mass transfer coefficient to increase with inlet Reynolds number.

Using the measured data a correlation for the mass transfer coefficient ($kg/m^2 \cdot s$) was obtained:

$$h_{mf}=7.34\times10^{-9}(X^*)^{-0.219}(W)^{-2.856}(T^*)^{-0.127}(R_{ed})^{0.171}(F_o)^{-0.188} \quad (5.10)$$

where:

h_{mf} Mass transfer coefficient with frost formation, defined by $h_{mf}=\frac{m_f}{\Delta W}$ ($kg/m^2 \cdot K$)

m_f The time rate of change of frost mass concentration ($kg/m^2 \cdot s$)

ΔW The humidity ratio difference between the inlet air and the saturated air at 0°C (kg/kg) (i.e. on the surface of the frost)

The root mean square error of Eq. (5.10) is 0.27, and the exponential coefficient of tolerance for each term is 0.96 for X^*, 0.91 for W, 0.92 for T^*, 0.93 for R_{ed} and 0.95 for F_o.

The dimensionless correlation analysis for mass transfer with frost formation is presented in Eq. (5.11):

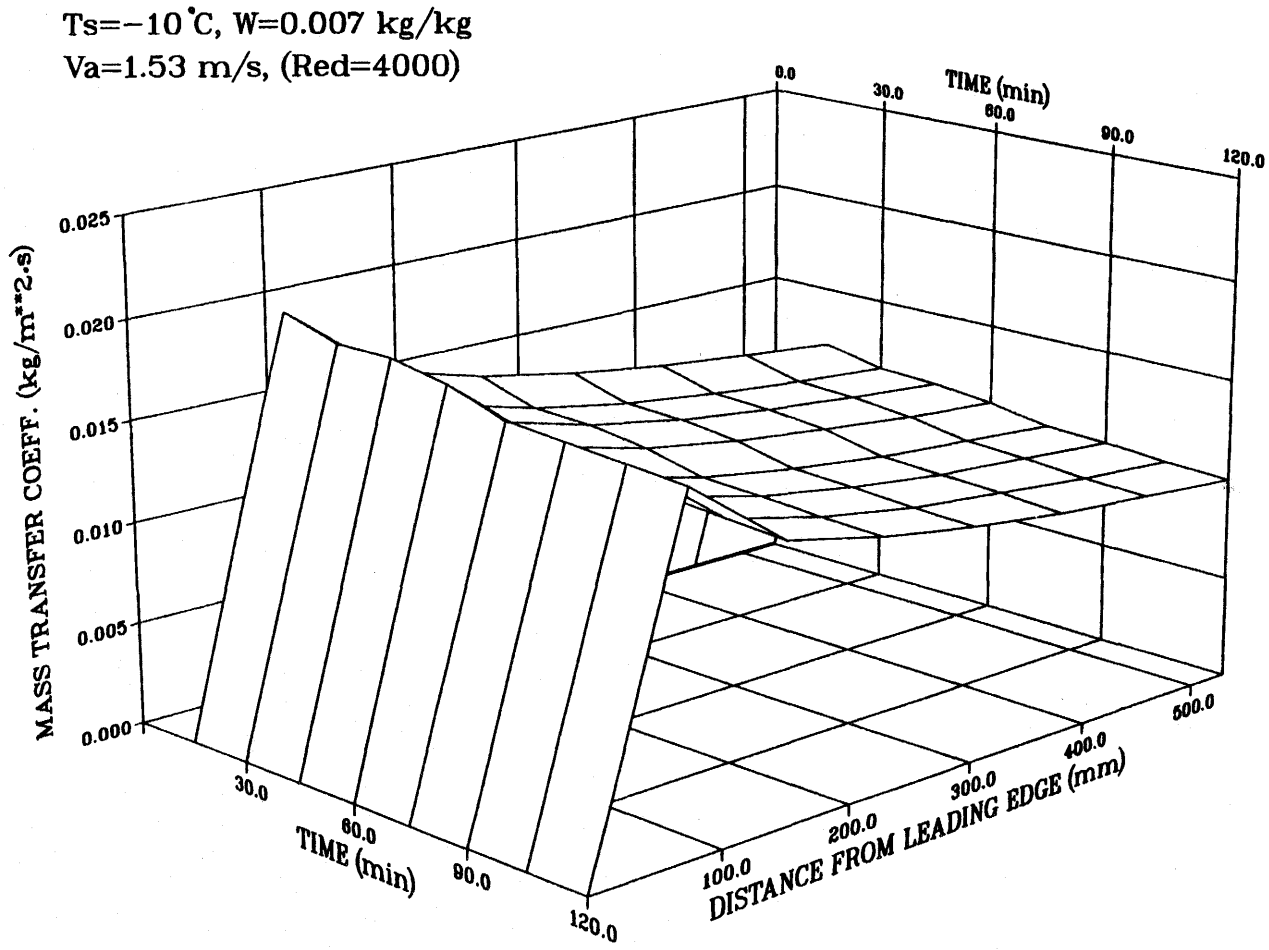

Figure 5.29 Frost mass transfer coefficient versus time and position

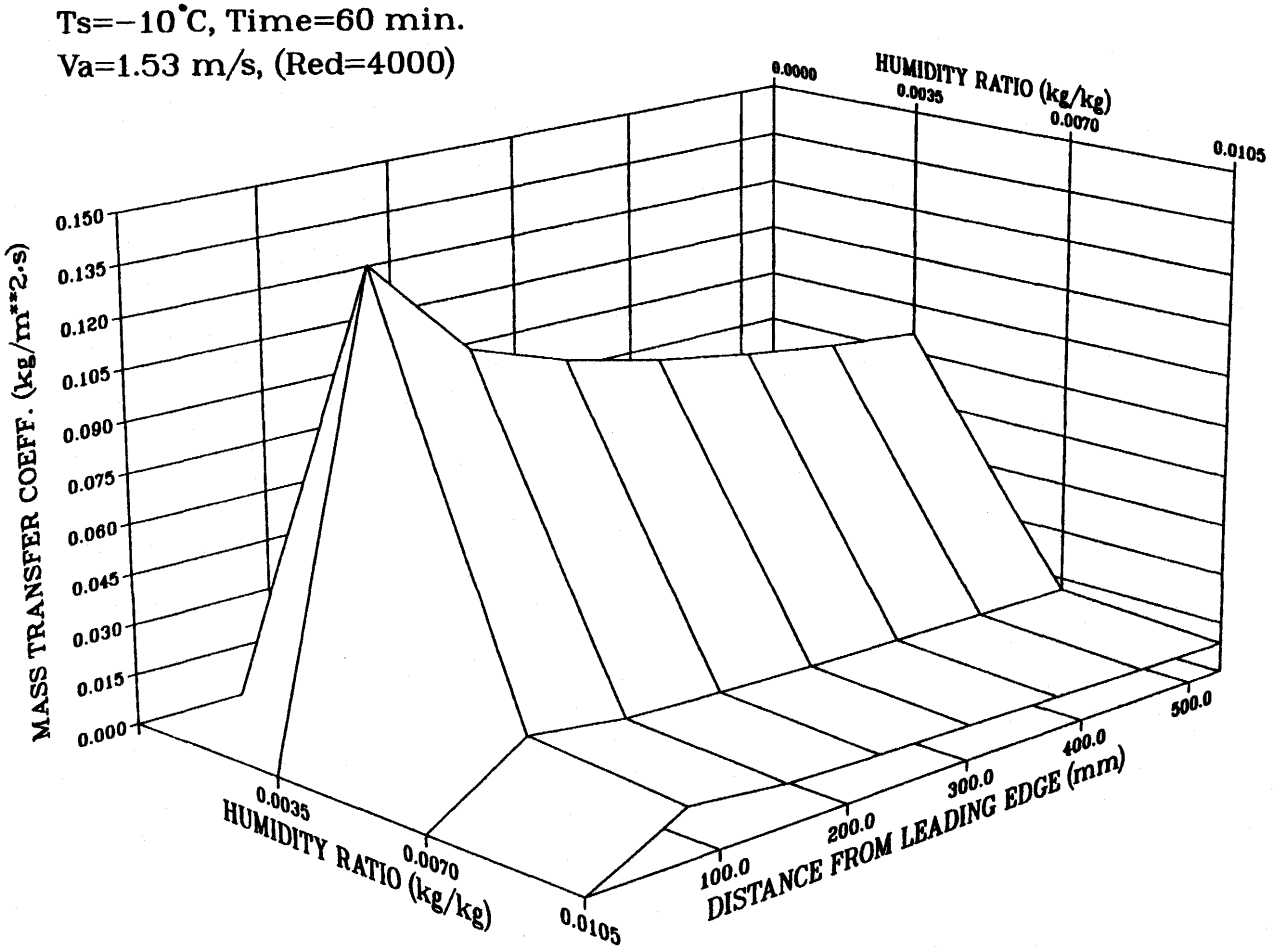

Figure 5.30 Frost mass transfer coefficient versus humidity ratio and position

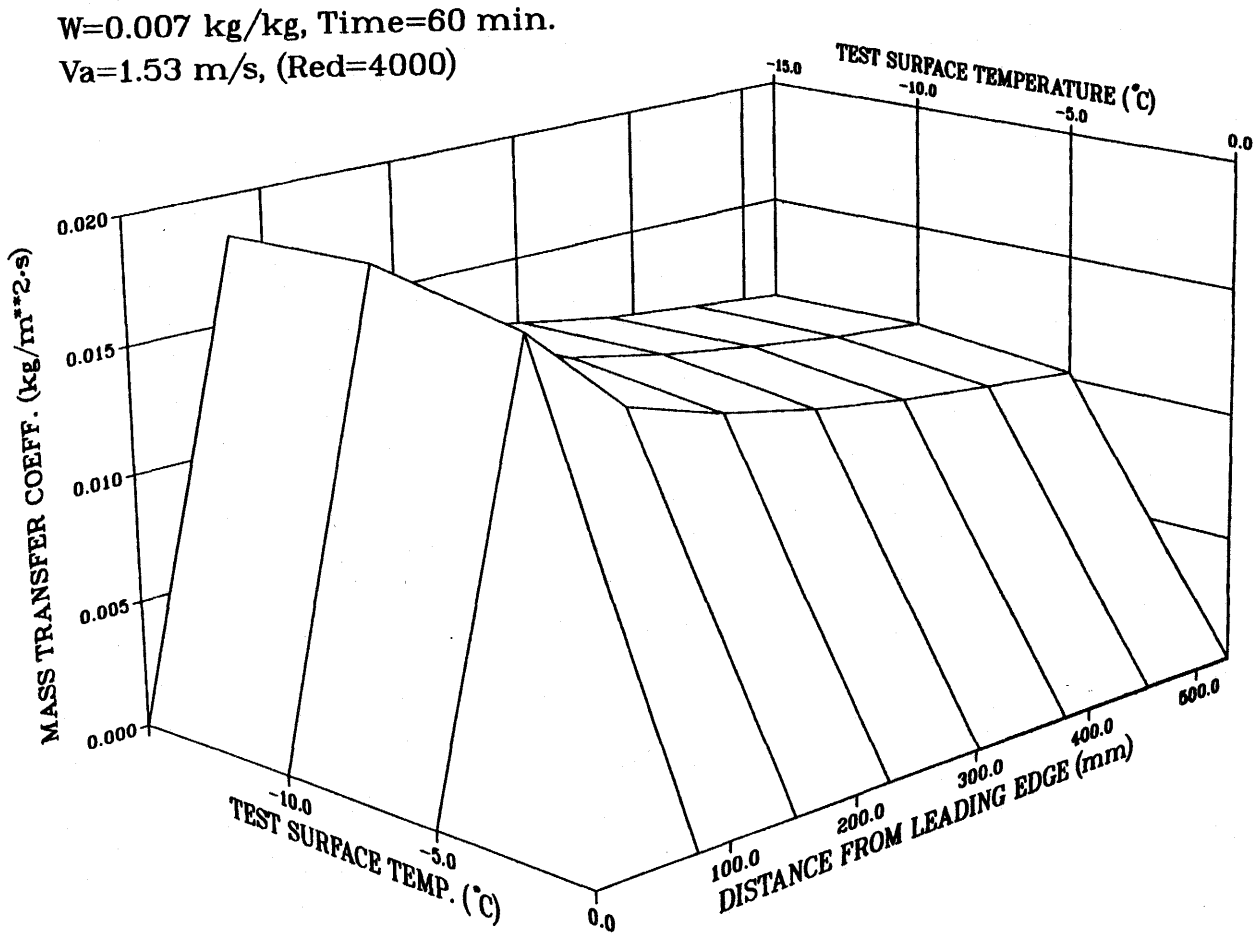

Figure 5.31 Frsot mass transfer coefficient versus test surface temperature and position

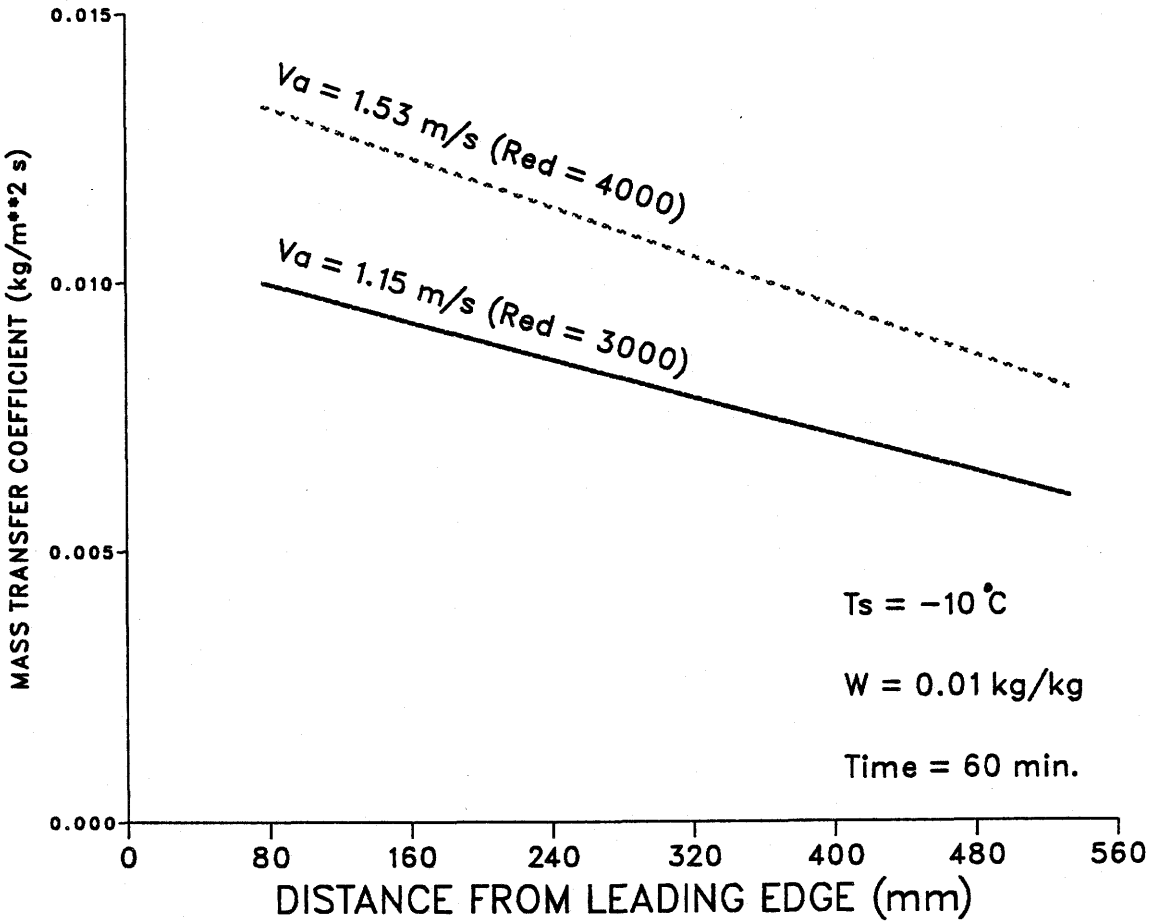

Figure 5.32 Frost mass transfer coefficient versus position with inlet air velocity or Reynolds number as a parameter

$$Sh_f=1.019\times10^{-5}(X^*)^{0.781}(W)^{-2.859}(T^*)^{-0.119}(R_{ed})^{0.185}(F_o)^{-0.187} \quad (5.11)$$

where:

Sh_f Sherwood number with frost formation, defined by $Sh_f=\frac{h_{mf}X}{D_{AB}}$

D_{AB} Binary diffusion coefficient for water vapor in air at the film temperature (m^2/s)

Figure 5.33 shows the comparison between the measured and computed data with the correlation, Eq. (5.11). The root mean square error of Eq. (5.11) is 0.27, and the exponential coefficient of tolerance for each term is 0.96 for X^*, 0.91 for W, 0.92 for T^*, 0.93 for R_{ed} and 0.95 for F_o.

Eq. (5.11) shows that the Sherwood number for air-to-frost mass transfer varies directly with distance from the leading edge on the test plate, the average test surface temperature, and air velocity, and inversely with the air humidity, and time.

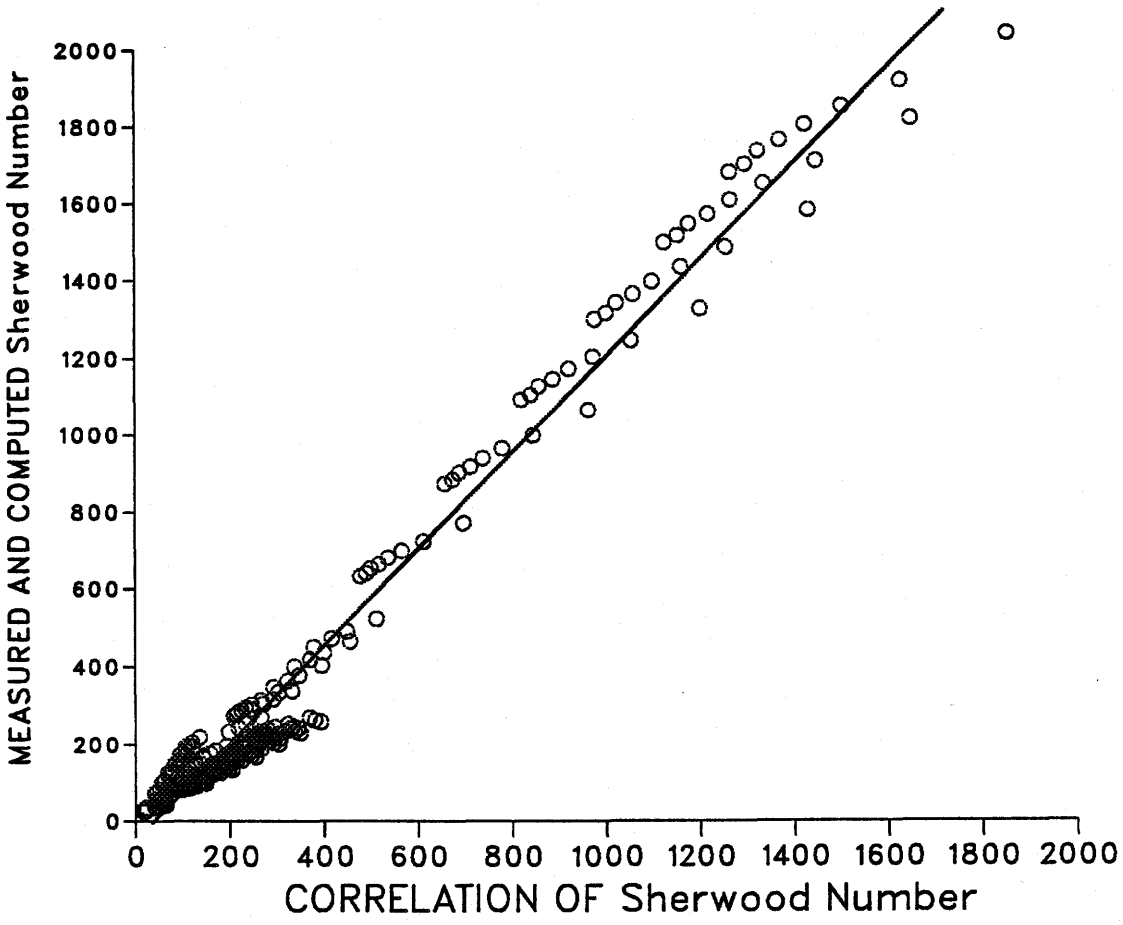

Figure 5.33 A comparison of measured and computed data with correlation for the Sherwood number

Chapter 6

DISCUSSION OF EXPERIMENTAL RESULTS

6.1. Comparison of the Correlations with other Experimental Data

The range of test conditions used in this study differs significantly from those reported by most researchers. However, some of the data reported by others can be used for comparison with the results reported here.

The experimental data reported by Hosoda et al. (1967) for frost thickness versus time is compared with the Eq. (5.2); the result is shown in Figure 6.1. The test facility of Hosoda et al. (1967), a cold copper plate (150 mm by 300 mm by 5 mm) was installed in a 150 mm square and 300 mm long rectangular duct such that frost grew on both sides of the plate. The frost thickness was measured using still photography. During their experiments, the copper plate would gradually become warmer. Figure 6.1 (a) shows that the correlation slightly overpredicts the data of Hosoda at a test surface temperature of -13 ^{o}C. The best agreement is obtained at a test surface temperature of -18 ^{o}C (Figure 6.1 (b)). In this comparison it is noted that the Reynolds number, R_{ed}, and the dimensionless position, X^{*}, are estimated since the inlet flow conditions and the location on the test plates for thickness measurements were not completely described by Hosoda.

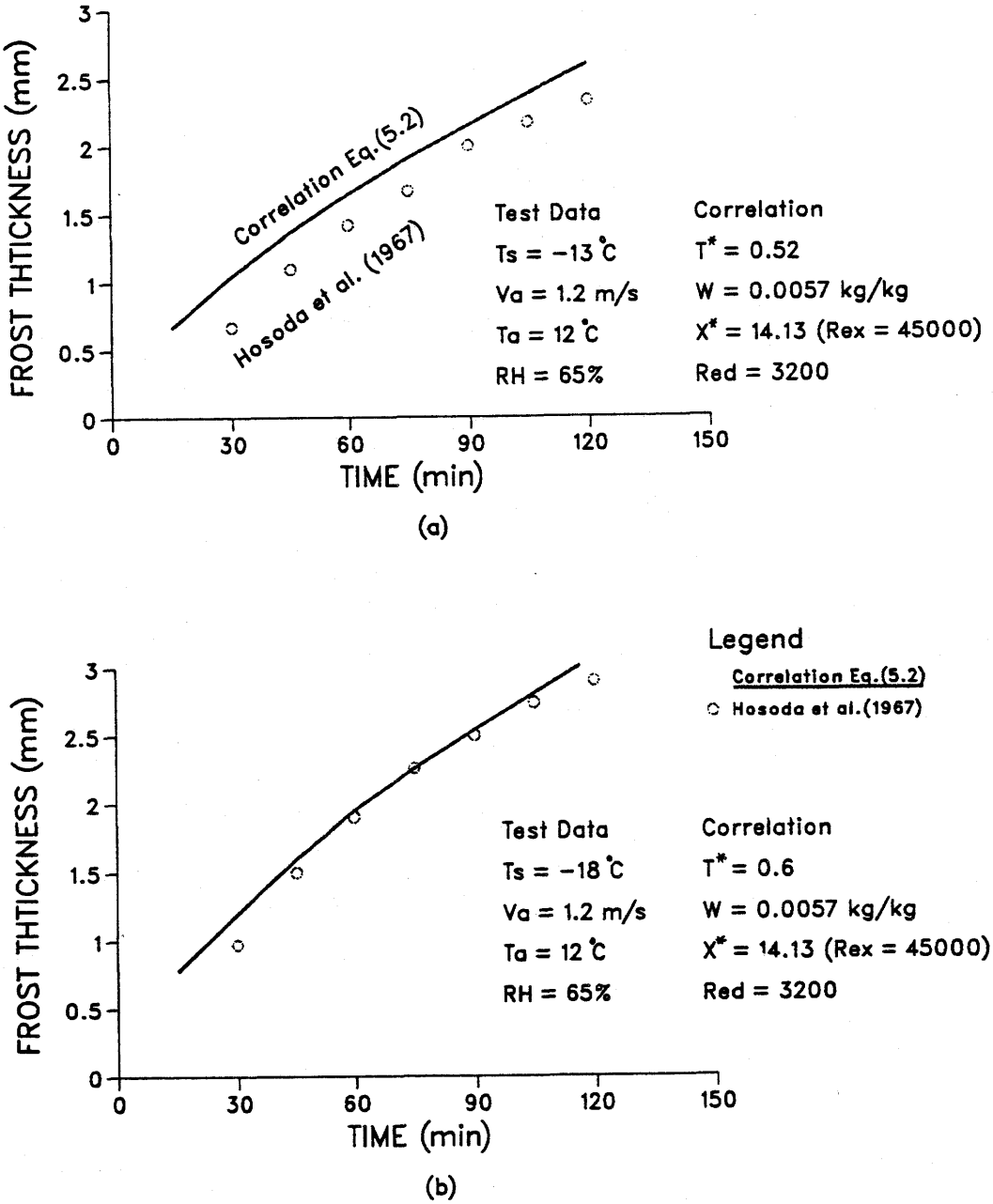

Figure 6.1 Comparison between Eq. (5.2) and the experimental data of Hosoda et al. (1967)

Figure 6.2 shows the comparison between Eq. (5.4) and the experimental data of Toyura et al. (1988) for the frost mass concentration. In the latter's experiment, the test section was 150 mm wide by 380 mm long and 150 mm high. The frost deposit surface was made of stainless steel (0.1 mm thick). The frost thickness was measured by bringing a fine wire into contact with the surface of the frost layer and reading a micro-cathetometer. Unfortunately, the technique and the accuracy associated with measuring the local mass concentration were not presented in this study. Also, the dimensionless position, X^*, is estimated.

The comparison of the correlation for predicting the frost density, Eq. 5.5, with the experimental data of Hayashi et al. (1977) is shown in Figure 6.3. The test plate in their experiment was made of stainless steel plate, 95 mm wide 1000 mm long and 21 mm thick, which was situated in a 1500 mm long and 250×250 mm test section. The method of measuring the density at the given location (x = 670 mm) was not presented. Figure 6.3 shows that the correlation predicted approximately 75% of the Hayashi's data, within the range of validity of the correlation presented in this study.

In the above comparisons, the differences between the correlations and the data reported by other researchers could be due to several reasons: (1) large differences in the techniques and consequently the accuracy for measuring the frost properties; (2) the errors associated with the measurement of the test surface temperature and air humidity; (3) the calculation of the Reynolds number based on hydraulic diameter in correlations; and (4) the definition of the starting time (t=0) in a particular test.

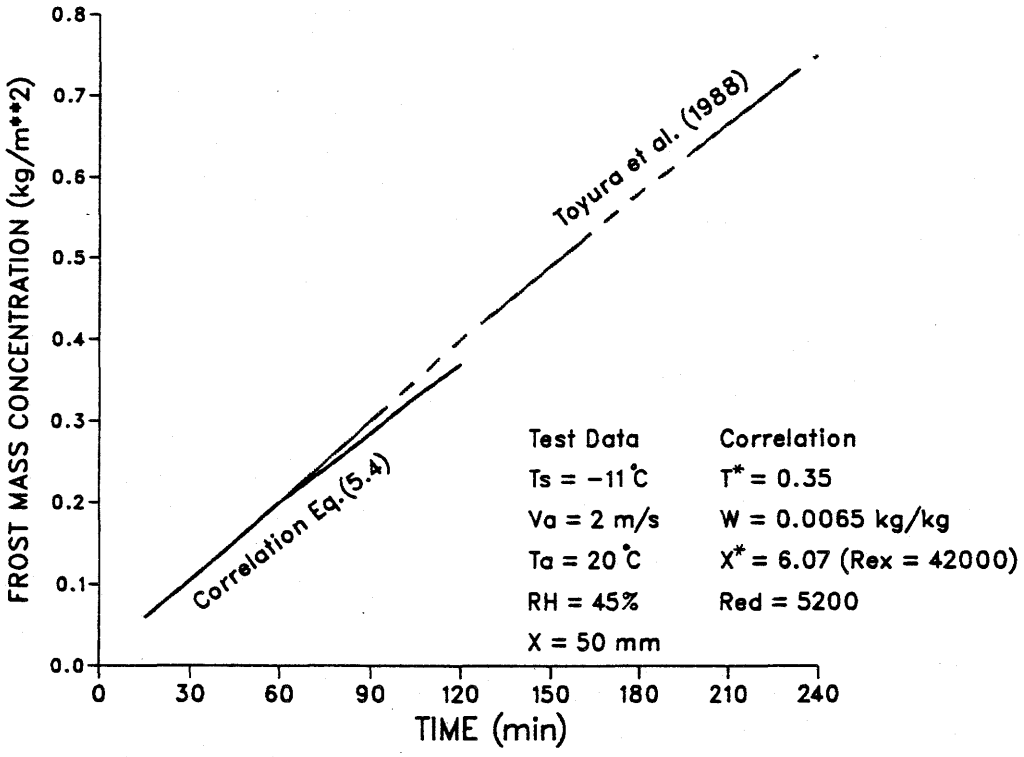

Figure 6.2 Comparison between Eq. (5.4) and the experimental data of Toyura et al. (1988)

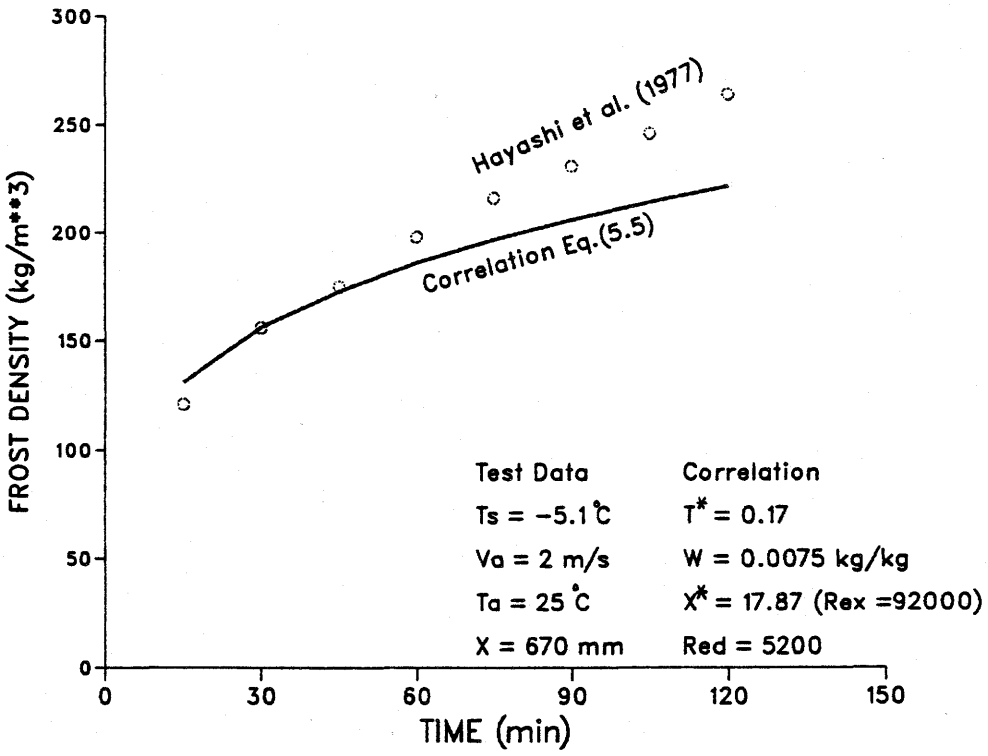

Figure 6.3 Comparison between Eq. (5.5) and the experimental data of Hayashi et al. (1977)

6.2. The Heat Flux Through the Frost Surface

The heat transfer process on the frosted surface is quite complicated. There are no models to calculate the heat flux directly without the experimental data. Considering the heat transfer from air to frost, and the latent heat due to sublimation to be quasi-steady, the total heat flux through the frost layer, q''_f, could be theoretically estimated from:

$$q''_f = q''_{fa} + q''_s \tag{6.1}$$

where q''_{fa} (W/m^2) is heat flux from air to frost, and is estimated from:

$$q''_{fa} = h_{fa}(T_a - T_{tp}) \tag{6.2}$$

and q''_s (W/m^2) is latent heat flux due to sublimation, and is given by:

$$q''_s = h_{sg} \cdot m_f \tag{6.3}$$

where:

h_{fa} Apparent heat transfer coefficient with frosting ($W/m^2 \cdot K$), $h_{fa} = Nu \frac{k_a}{X}$

T_a Air temperature (^oC)

T_{tp} Triple point temperature, 0 ^oC

h_{sg} Latent heat of sublimation for water vapor from gas to solid (J/kg)

m_f Frost mass concentration rate (kg/m^2)

Alternatively, the heat transfer process from the air to the frost surface could be treated as a constant heat flux or constant wall temperature process by assuming no phase change similar to the heat transfer on a flat plate. The Nusselt number, Nu, in this case can be calculated using the following equation (Kays, W. M. and Crawford, M. E. 1980):

$$StPr^{0.4} = 0.03 R_{ex}^{-0.2} \tag{6.4}$$

where: $St = \frac{Nu}{R_{ex} Pr}$

Using equations (6.1) to (6.4) and the correlation given in Chapter 5 (Eq. 5.4), which could be used for calculating the frost mass concentration rate, the heat flux can be estimated. Figure 6.4 shows the comparison between the predicted heat flux and the measured frost heat flux. The measured heat flux data agree with the predicted heat flux within ±25%.

As a result of the experimental apparatus configuration the reported data for the heat flux includes the contribution due to axial conduction along the test plate. The experimental test plate was designed to minimize this axial heat flux while still satisfying the requirements to measure the distribution of frost mass. The design was such that this heat flux would be much smaller than the heat flux through the heat-flux meter, but small rapid changes in heat flux would not be accurately monitored by such a system. As discussed earlier in Chapter 3, the temperature gradient along the flow direction and which decreases from the leading edge on the test plate results in a heat flux in the test plate. This axial heat flux was found to be substantial near the leading edge (approximately 23% of the total heat flux through the frost). This correction has been added to all the heat flux data.

6.3. The Effective and Apparent Frost Thermal Conductivity

Comparing the typical data of frost thermal conductivity with the frost mass concentration (Chapter 5), it can be seen that both vary in a similar manner with each independent test parameter. This could be attributed to the fact that the measured heat flux used to calculate the frost thermal conductivity is obtained based on the assumption that the frost surface-to-air interface temperature is 0°C and quasi-steady heat conduction

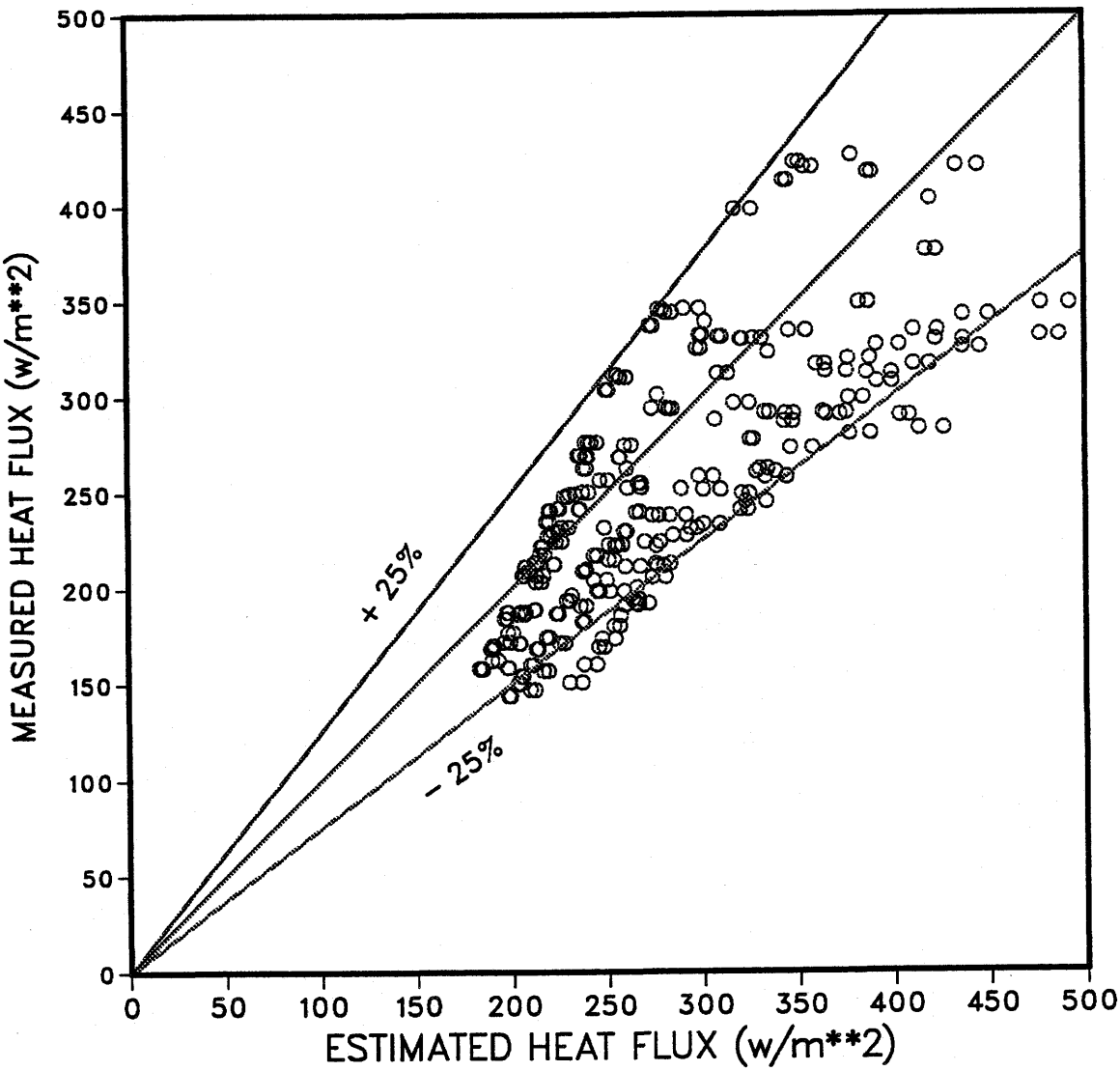

Figure 6.4 Comparison between estimated (Eq. 6.1 to 6.4 and 5.4) and measured frost heat flux

involves no phase change. This assumption is used inspite of the fact that the measured heat flux includes the latent heat flux due to sublimation. Therefore, the frost thermal conductivity is affected by the rate of frost mass accumulating in the frost layer. It is renamed the apparent thermal conductivity here. An alternative approach is to estimate the thermal conductivity of a porous structure based on the volume fraction of each component. Eq. (6.5) (Tao et al. 1991) can be used to obtain the effective frost thermal conductivity, k_{eff}, thus:

$$k_{eff} = \varepsilon_i \cdot k_i + \varepsilon_a \cdot k_a \tag{6.5}$$

where:

ε_i Average volume fraction of ice in the frost layer,

$$\varepsilon_i = \frac{\rho_f}{\rho_i}$$

k_i Thermal conductivity of ice (W/m·K)

ε_a Volume fraction of air in frost, $\varepsilon_a = 1 - \varepsilon_i$

k_a Thermal conductivity of air (W/m·K)

Figure 6.5 shows a comparison between the effective and the apparent thermal conductivities. As can be seen, the effective thermal conductivity calculated from Eq. (6.5) is five times larger than apparent thermal conductivity calculated from Eq. (5.7). It should be noted, however, that the effective frost thermal conductivity describes this value in one dimension only, while the frost conductivity results from heat flux in the frost layer, a three dimensional process. Perhaps this difference between the effective and the apparent thermal conductivities could explain why one should not accept the argument that the frost thermal conductivity is a function of the frost density alone. Physically this is a very complex problem; further research needs to be done to explain the physical processes before accurate estimates of the thermal processes can be made.

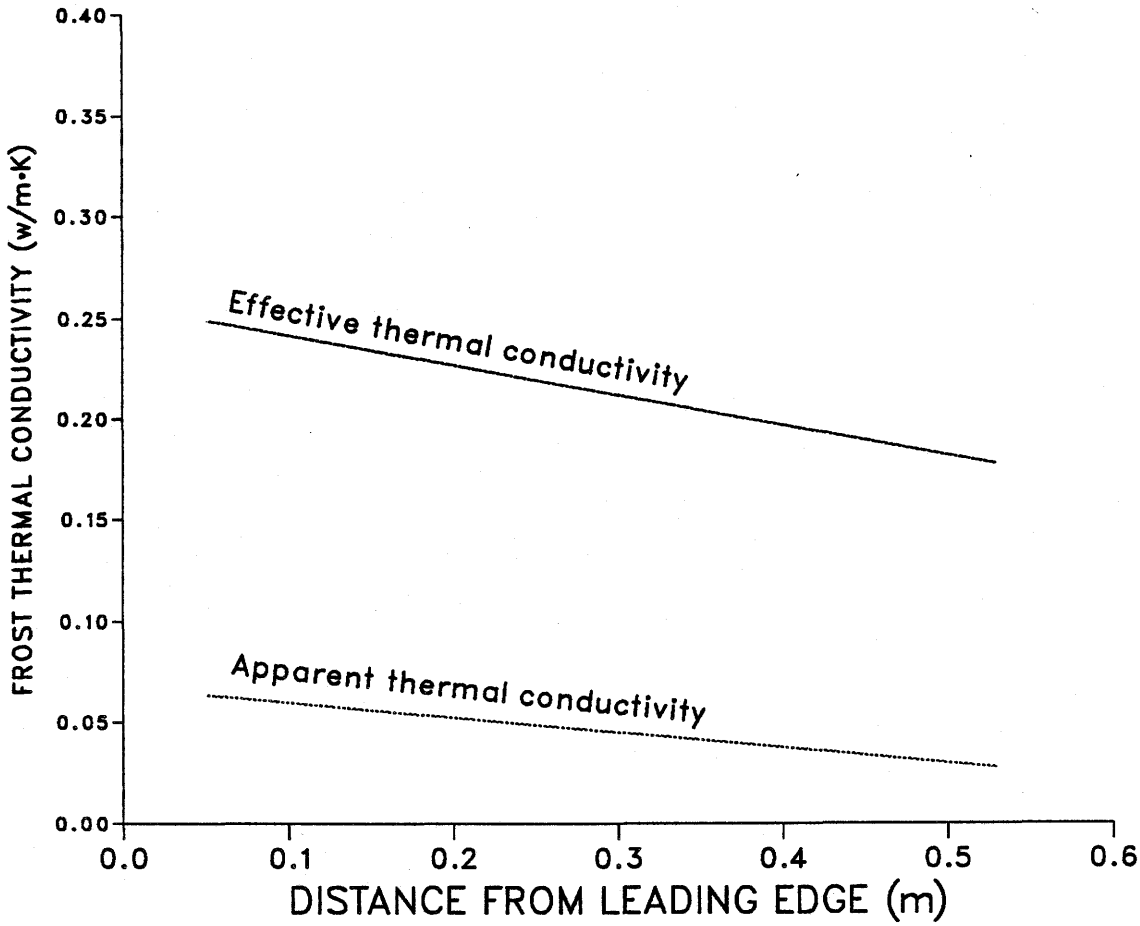

Figure 6.5 The effective (Eq. 6.5) and the apparent (Eq. 5.6) frost thermal conductivity

6.4. The Apparent Frost Nusselt Number

The correlation for the Nusselt number across the frosted surface, Eq. 5.9, is based on the thermal conductivity of air at the film temperature and the convective heat transfer coefficient (defined as $h_f=q''_f/(T_a-0)$). Again, the frost-air interface temperature is assumed to be 0 °C, while the heat flux is taken to be equal to the corrected measured cold plate heat flux. Therefore, the calculated Nusselt number is actually an overall frost Nusselt number, Nu_{fo}. That is, the quasi-steady heat flux through the frost-air interface, q''_{fa}, is expected to differ from the measured heat flux, q''_f, by an amount equal to the product of the rate of mass concentration, m_f, and the heat of sublimation, h_{sg}:

$$q''_{fa} = q''_f - m_f h_{sg} \tag{6.6}$$

The apparent Nusselt number for heat transfer between the air and frost surface, Nu_{fa}, using this definition of heat flux is therefore:

$$Nu_{fa} = \frac{h_{fa} \cdot x}{k_a} \tag{6.7}$$

where: $h_{fa} = q''_{fa}/(T_a-0)$.

Finally, the correlation of apparent Nusselt number, Nu_{fa}, is:

$$Nu_{fa} = 0.051\ (X^*)^{0.611}\ (W)^{-0.860}\ (T^*)^{1.647} (R_{ed})^{0.317}\ (F_o)^{0.206} \tag{6.8}$$

The root mean square error of Eq. (6.8) is 0.37, and the exponential coefficient of tolerance for all the independent terms exceeds 0.99. The higher root mean square error indicated that the value of latent heat flux, employed here, might be not correct. Perhaps

an empirical constant needs to be added to correct the error caused by the different between the free convection and the forced convection.

Comparing of the Eq. (6.8) (or Eq. 5.9) with Eq. (5.11), it is clear that there is no apparent simple relationship between the heat transfer and mass transfer under frosting conditions. Although both coefficients have the same dependency with distance from leading edge, air velocity and humidity ratio, the trends with the average test surface temperature and time (and the air humidity for Eq. 5.9) are different. Therefore, the heat transfer and mass transfer under frosting conditions can not be treated as only a function of Reynolds number, i.e. they do not appear to be directly related through the Chilton-Colburn analogy, as previous studies have suggested.

6.5. Frost Properties with Position

As mentioned earlier in Chapter 5, the frost mass concentration-time-distance surface is not perfectly smooth (see Figure 5.7). This is due to experimental uncertainties and slight differences in operating conditions between one test and another. In order to observe the mass accumulation of frost with time at any position on the cold plate, Figure 6.6 presents the correlated data of frost mass concentration as a function of position with time as a parameter for three different test surface temperatures. The mass concentration starts at zero over the entire plate but the rate of mass concentration is much larger toward the leading edge. In this figure, the frost mass concentration at any position, x, from the leading edge was correlated with time using the following relation:

$$m_f = a_1 t + a_2 t^2 \tag{6.9}$$

where a_1 and a_2 are empirical constants. The root mean square errors of Eq. (6.9) did not exceed 0.007 kg/m^2, and the coefficient of tolerance always exceeds 0.99.

As discussed in a paper submitted to ASHRAE for review (Mao, Besant, and Rezkallah 1991), Figure 5.2 (Chapter 5) and 6.6 show that the frost thickness and mass concentration exhibit characteristics in which the fluid mechanics of air flowing over an abrupt frost thickness step at the leading edge appears to be important. It is expected that an accurate prediction of the airflow coupled with heat and mass transfer will be necessary for the accurate prediction of frost growth in this region. Further downstream, $x>380$ mm, the frost growth behaves more like a typical fully developed heat and mass flux boundary layer in which the heat and mass fluxes decrease with increasing distance from the leading edge. Between these two regions, $150<x<380$ mm, the frost growth appears to be in transition from the leading edge, where fluid mechanics effects are coupled to the heat and mass transfer ($x<150$ mm), to a fully developed boundary layer ($x>380$ mm).

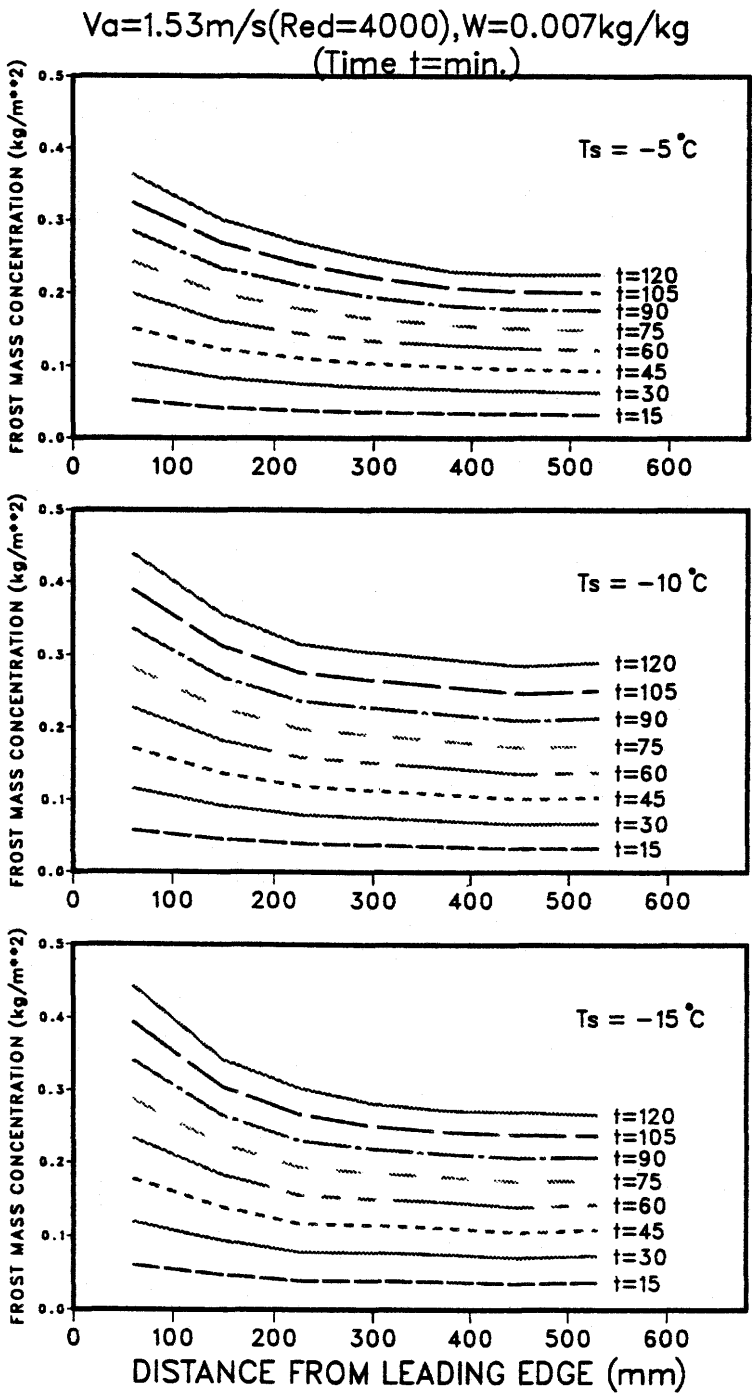

Figure 6.6 Frost mass concentration versus position with time as a parameter

Chapter 7

SUMMARY, CONCLUSIONS AND FUTURE WORK

7.1. Summary

The object of this study was to devise new techniques to measure the frost thickness and mass concentration, to collect frost property data over a range of test variables, and to correlate these data. The following summarizes the accomplishments and the main findings from the study:

1. A test apparatus was designed and constructed which is capable of providing the desired test conditions and measuring the frost thickness, density and heat transfer rates across the frosted surface. The temperature distribution in the test apparatus and the air temperature and humidity measurements were taken with an uncertainty of temperature and air humidity of $\pm 0.1^{o}C$, and 0.0016 kg/kg, respectively.

2. A new frost thickness measurement system was designed, assembled and calibrated. This new method of frost height measurement, which uses a low power laser beam and a sensitive light meter, has a precision of 0.025 mm.

3. A new method of measuring the local mass concentration of frost was developed and tested. This technique employs the use of fourteen thin,

small disks thermally bonded to the cold plate to collect the frost samples. The mass concentration and density can be obtained at seven location on a frost growth boundary layer using this technique with less than 4% error for frost thicknesses between 1 and 3 mm.

4. Over 50 test runs were carried out for frost accumulation and heat flux measurements over a wide range of test conditions, as shown in Table 7.1, and the recorded test data are listed in Appendix C.

5. Using the test data, correlations were developed for the characteristics of frost mass concentration, thickness, density, thermal conductivity, convective heat transfer coefficient, frost Nusselt number, mass transfer coefficient and the Sherwood number. These correlations are summarized in Table 7.2.

Table 7.1 Range of Environmental Parameters Used in the Experiments

Parameter	Range
Time (minutes)	0 to 120
Distance from leading edge (mm)	0 to 600
Test surface temperature (^{o}C)	-5 to -15
Supply air humidity ratio (kg/kg)	0.004 to 0.01
Supply air temperature (^{o}C)	15 to 23
Supply air velocity (m/s)	1.15 to 2.67
Inlet Reynolds number	3000 to 7000

Table 7.2 Summary of Correlations for Frost Growth and Heat and Mass Transfer with Airflow over a Cold Flat Plate

Exponent (Coefficient of Tolerance)							
Frost Variable	Intercept	RMS	X^*	W	T^*	R_{ed}	F_o
$\frac{\delta_f}{\delta_{ice}}$	1.875×10^{5}	0.22	0.132(0.96)	0.405(0.91)	1.017(0.92)	-0.720(0.93)	-0.253(0.95)
m_f (kg/m^2)	7.630×10^{-4}	0.13	-0.230(0.96)	1.318(0.91)	0.083(0.92)	1.064(0.93)	0.908(0.95)
δ_f (m)	0.156	0.22	-0.098(0.96)	1.723(0.91)	1.10(0.92)	0.343(0.93)	0.655(0.95)
$\frac{\rho_f}{\rho_{ice}}$	5.559×10^{-6}	0.22	-0.137(0.96)	-0.413(0.91)	-0.997(0.92)	0.715(0.93)	0.252(0.95)
$\frac{K_f}{K_{ice}}$	0.011	0.24	-0.370(0.96)	2.044(0.91)	0.216(0.92)	1.093(0.93)	0.699(0.95)
h_f (w/m^2 K)	0.506	0.11	-0.302(0.96)	0.297(0.91)	0.725(0.92)	0.717(0.93)	0.035(0.95)
Nu_{fo}	0.720	0.12	0.698(0.96)	0.294(0.91)	0.729(0.92)	0.721(0.93)	0.036(0.95)
Nu_{fa}	0.051	0.37	0.611(0.99)	-0.860(0.99)	1.647(0.99)	0.317(0.99)	0.206(0.99)
h_{mf} (kg/m^2 s)	7.34×10^{-9}	0.27	-0.219(0.96)	-2.856(0.91)	-0.127(0.92)	0.171(0.93)	-0.188(0.95)
Sh_f	1.019×10^{-5}	0.27	0.781(0.96)	-2.859(0.91)	-0.119(0.92)	0.185(0.93)	-0.187(0.95)

Range of variables: $1.33<X^*<14.13$, $0.004<W<0.01$, $0.24<T^*<0.51$, $3000<R_{ed}<7000$, $13<F_o<104$.

7.2. Conclusions

Prior to this work, no investigators have accurately measured the frost mass concentration at different and uniformly distributed locations on the test plate; no data was available to quantify the variation in the frost properties with the distance from the leading edge on a flat plate and no dimensionless correlations of frost properties existed as a function of dimensionless position, time, air humidity, air velocity and temperature. The present data and correlations lead to a number of general conclusions over the range of test variables; these are:

1. The frost mass concentration, m_f, thickness, δ_f, thermal conductivity, k_f, and convective heat transfer coefficient, h_f, (1) increases with increasing time, air humidity ratio and velocity, and with decreasing test surface temperature; and (2) decreases with increasing the distance from the leading edge on the test plate.

2. The frost density, ρ_f, (1) increases with increasing time, air velocity, and the test surface temperature; and (2) decreases with increasing air humidity ratio and distance from the leading edge of the test plate.

3. The frost overall Nusselt number, Nu_{fo}, increases with increasing the values of all the independent variables except it decreases with test surface temperature. The apparent Nusselt number, Nu_{fa}, (1) increases with increasing air velocity, distance from the leading edge on the test plate, time and with decreasing the test surface temperature; and (2) decreases with increasing air humidity ratio.

4. The mass transfer coefficient, h_{mf}, (1) decreases with increasing time, air humidity ratio, and distance from the leading edge on the test plate; and (2) increases with increasing air velocity and the test surface temperature. The mass transfer Sherwood number, Sh_f, (1) increases with increasing the distance from leading edge on the test plate, air velocity, and test surface temperature; and (2) decreases with increasing air humidity ratio and time.

7.3. Future Work

This study has raised many questions about the frost formation process and frost properties. Further studies should be done to address some of the problems:

1. Since the range of the test variables was limited in this study, steps should be taken to extend this range to accommodate the wider heat exchanger operational range found in practical applications. Particularly, the frost formation, for air temperatures in the range of 15 $^{o}C>T_a>0$ ^{o}C, test plate temperature in the range of 0 $^{o}C>T_p>-5$ ^{o}C, inlet Reynolds numbers in the transition range, $2000<R_{ed}<3000$, and laminar range, $1000<R_{ed}<2000$, and air humidity $W>0.01$, should be investigated.

2. The geometry of the current experimental apparatus should be changed to investigate a narrow airflow passage similar to the spacing in a finned tube heat exchanger. The time variation of heat exchanger fin efficiency should be investigated as frost forms on the fins of a heat exchanger.

3. In order to more fully understand the physics of frost formation, a study should be undertaken to investigate and model the variation in frost

properties (such as temperature and density) inside the frost layer. The effect of surface conditions on the formation of frost, such as surface roughness and material type (e.g. Teflon), are not fully understood. New experiments need to be devised to investigate these factors. Accurate models of these phenomena will permit the extrapolation of existing frost property data over wider ranges of operating variables. Such studies would not be possible without new instrumentation and new theoretical models.

4. The properties of frost layers during defrosting should be investigated to determine the most efficient methods and procedures for defrosting cycles in heat exchangers.

REFERENCES

Abdel-wahed, R.M., Hifni, M.A., and Sherif, S.A., 1984. "Heat and mass transfer from a laminar humid air stream to a plate at subfreezing temperature." International Journal of Refrigeration, Vol.7, No.1.

Barrow, H. 1985. "A note on frosting of heat pump evaporator surfaces." Heat Recovery Systems Vol.5, No.3

Beatty, Jr.K.O., Finch, E.B., and Schoenborn, E.M. 1951. "Heat transfer from humid air to metal under frosting conditions." Journal of the ASRE

Besant, R.W., Rezkallah, K.S., Mao, Y., and Falk, J., 1990. "Measurement of frost thickness using a laser beam and light meter." ASHRAE Transactions, Vol.96, Pt.1.

Biguria, G.,and Wenzel, L.A., 1970. " Measurement and correlation of water frost thermal conductivity and density." I&EC Fundamentals, Vol.9.,No.1.

Brian, P.L.T., Reid, R.C., and Shah, Y.T., 1970. "Frost deposition on cold surfaces." Ind.Eng.Chem. Fundm., Vol.9,No.3.

Chung, P.M., Algren, A.B., and Minneapolis, M. 1958. "Frost formation and heat transfer on a cylinder surface in humid air cross flow. part 1: Experimental study." Heating, Piping & Air Conditioning, September pp171-178

Chung, P.M., Algren, A.B., and Minneapolis, M. 1958. "Frost formation and heat transfer on a cylinder surface in humid air cross flow. part 2: Theoretical stuy and conclusions." Heating, Piping & Air Conditioning, October pp115-122

Cremers, C.J., Hahn, O.J., and Skorupski, J.H. 1978. "Frost density measurements on vertical cylinders by Gamma-Ray attenuation." Advances in Cryogenic Engineering Vol.23, pp371-375

Cremers, C.J., and Mehra, V.K., 1982. "Frost formation on vertical cylinders in free convection." Journal of Heat Transfer, Vol.104/3.

Gates, R.R., Sepsy, C.F., and Huffman, G.D. 1967. "Heat transfer and perssure loss in extended surface heat exchangers operating under frosting conditions. Part 1: Literature survey, test apparatus and perliminary results." ASHRAE Transactions Vol.73, Pt.2

Gordon, J., Wylen, V. & Sonntag, R.E. 1965. *Fundamentals of classical thermodynamics* John Wiley & Sons, Inc.

Hayashi, Y., Aoki, A., Adachi, S., and Hori, k., 1977. "Study of frost properties correlating with frost formation types." Journal of Heat Transfer, Vol.99.

Holman, J.P. 1981. *Heat transfer* McGraw-Hill, Inc.

Hosoda, T.,and Uzuhashi, H., 1967. "Effects of frost on the heat transfer coefficient." HITACHI Review Vol.16, No.6

Huffman, G.D. and Sepsy, C.F. 1967. "Heat transfer and perssure loss in extended surface heat exchangers operating under frosting conditions. Part 2: Data analysis and correlation." ASHRAE Transactions Vol.73, Pt.2

Incropera, F.P. and DeWitt, D.P. 1987. *Fundamentals of heat and mass transfer* John Wiley & Sons, Inc.

Jones, B.W. and Parker, J.D. 1975. "Frost formation with varying environmental parameters." Journal of Heat Transfer

Kays, W.M. and Crawford, M.E. 1980. *Convective heat and mass transfer* McGraw-Hill Book Company.

Kamei, S., Mizushina, T., Kifune, S., and Koto, T. 1952. "Research on the frost formation in a low temperature cooler condenser." The JAPAN SCIENCE REVIEW Vol.2 No.3

Kondepude, S.N. and O'Neal, D.L. 1989. "The effects of frost growth on extended surface heat exchanger performance: A Review." ASHRAE Transactions Vol.93, Pt.2

Kondepude, S. and O'Neal, D. 1989. "The effects of frost formation on the thermal performance of finned tube heat exchangers." AIAA 24th Thermophysics Conference AIAA89-1741

Krakow, K.I., Lin, S., and Oskarsson, S.P. 1990. "A method for determining the effects of coil geometry and fan type on evaporator frosting." ASHRAE Transactions Vol.96, Pt.1

Loper, J.L. 1960. "Frost formation upon a thin aluminum tank containing liquid oxygen." ASHRAE Transactions Vol.66, No.1703

Mao, Y., Besant, R.W., and Rezkallah, K.S. 1991.(a) "A method of measuring frost density using flush-mounted removable disks." ASHRAE Transactions, Vol.97, Pt.1

Mao, Y., Besant, R.W., and Rezkallah, K.S. 1991.(b) "Measurement and correlation of frost properties with air flow over a flat plate." Submitted to ASHRAE for review.

Marinyuk, B.T. 1980. "Heat and mass transfer under frosting conditions." International Journal of Refrigeration Vol.3 No.6

Niederer, D.H. 1976. "Frosting and defrosting effects on coil heat transfer." ASHRAE Transactions Vol.82, Pt.1

O'Neal, D.L. 1982. "The effect of frost formation on the performance of a parallel plate heat exchanger." Ph.D Thesis, Purdue University

O'Neal, D.L., and Tree, D.R., 1984. "Measurement of frost growth and density in a parallel plate geometry." ASHRAE Transactions, Vol.90(2A), pp278-290.

O'Neal, D.L., and Tree, D.R., 1985. "A review of frost formation in simple geometries." ASHRAE Transactions, Vol.91, Pt.2

Osharsson, S.P., Krakow, K.L., and Lin, S. 1990. "Evaporator model for operation with dry, wet, and frosted finned surfaces Part 1: Heat transfer and fluid flow theory." ASHRAE Transactions, Vol.96, Pt.1

Osharsson, S.P., Krakow, K.L., and Lin, S. 1990. "Evaporator model for operation with

dry, wet, and frosted finned surfaces Part 2: Evaporator models and verification." ASHRAE Transactions, Vol.96, Pt.1

Padki, M.M., Sherif, S.A., and Nelson, R.M. 1989. "A simple method for modelling the frost formation phenomenon in different geometries." ASHRAE Transactions, Vol.95, Pt.2

Parish, H.C., and Sepsy, C.F. 1972. "A numerical analysis of frost formation under forced convection." ASHRAE Transactions, Vol.79, Pt.1

Patankar, S.V. 1980. *Numerical heat transfer and fluid flow* Hemisphere Publishing Corporation.

Phillips, E.G., Chant, R.E., Bradley, B.C., and Fisher, D.R. 1989. "A model to compare freezing control strategies for residential air-to-air heat recovery ventilators." ASHRAE Transactions, Vol.95, Pt.2

Rite, R.W., and Crawford, R.R. 1991. a:"The effect of frost accumulation on the performance of domestic refrigerator-freezer finned tube evaporation coils." ASHRAE Transactions, Vol.97, Pt.2

Rite, R.W., and Crawford, R.R. 1991. b:"A parameteric study of factors goveming the rate of frost accumulation on domestic refrigerator-freezer finned tube evaporation coils." ASHRAE Transactions, Vol.97, Pt.2

Sami, S.M. and Duong, T. 1989. "Mass and heat transfer during frost growth." ASHRAE Transactions Vol.95, Pt.1

Sanders, C.th., 1974. "The influence of frost formation and frosting on the performance of air coolers." Ph.D. Dissertation, Technische Hogeschool, Delft, Netherlands.

Schneider, H.W. 1972. "Transferred mass and density of frost formed on a cylindrical tube in cross flow." IIR-Commissions B1, B2, and EL. (International Institute of Refrigeration) pp149-155

Schneider, H.W., 1978. "Equation of the growth rate of frost forming on cold surfaces." Int. J. Heat Mass Transfer, Vol.21, pp1019-1024

Schulte, D.W., and Howell, R.H. 1982. "The effect of air turbulence on the rate of frost growth on a horizontal flat plate." ASHRAE Transactions, Vol.87, Pt.2

Senshu, T., Yasuda, H., Oguni, K., and Ishibane, K., 1990."Heat pump performance under frosting conditions: Part 1- Heat and mass transfer on cross-finned tube heat exchangers under frosting conditions," ASHRAE Transactions, Vol.96, Pt.1

Sherif, S.A., Abdel-Wahed, R.M., and Hifini, M.A. 1988. "A mathematical model for the heat and mass transfer on a flat plate under frosting conditions." ASME/AIChE 25th National Heat Transfer Conference Proceedings

Stoecker, W.F. 1957. "How frost formation on coils affects refrigeration systems." Refrigerating Engineering Vol.65, No.2

Stoecker, W.F. 1960. "Frost formation on refrigeration coils." ASHRAE Transactions, Vol.66

Tao, Y-X, Besant, R.W. and Rezkallah, K.S. 1991. "A mathematical model for predicting the densification and growth of frost on a flat plate." Submitted for reivew to the International Journal of Heat and Mass Transfer

Tantakitti, C. and Howell, R.H. 1986. "Air-to-air heat pumps operating under frosting conditions on the outdoor coil." ASHRAE Transactions Vol.92, Pt.1

Thigpen, j.j., Canterbury, J., Killgore, E.M., and Trammel, G.J. 1964. "The investigation of heat transfer and frost formation in humid air flowing across a plate surface held at sub-freezing temperatures." National Science Foundation, Report submitted by the Dept. of Engineering Research at Louisiana Polytechnic Inst. Ruston, Louisiana.

Thompson, D.R. 1958. "Frost formation on cryogenic heat exchangers with atmospheric heat sources." ASME 85-HT-3

Tokura, I., Saito, H., and Kishinami, K. 1983. "Study on properties and growth rate of frost layers on cold surfaces." Journal of Heat Transfer, Vol.105/895.

Tokura, I., Saito, H., and Kishinami, K. 1988. "Prediction of growth rate and density of frost layer developing under forced convection." Warme-und Stoffubertragung 22, pp285-290. Spring-Verlag, in English.

Touloukian, Y.S., Powell, R.W., Ho, C.Y., and Klenmens, P.G. 1970. "Thermal conductivity." TPRC Vol.2, Nonmetallic Solids, IFI/PLENUM, NY, pp956-958.

Trammel, G.J., Little, D.C., and Killgore, E.M. 1968. "A study of the frost formed on a flate plate held at sub-freezing temperatures." ASHRAE Journal Vol.10, No.7

White, J.E., and Cremers, C.J. 1981. "Prediction of growth parameters of frost deposits in forced convection." Journal of Heat Transfer Vol.103

Wijeysundera, N.E., Bong, T.Y. and Yeo, S.H. 1984. "Measurement and analysis of frost density distribution on a vertical tube in free convection." 84-WA/HT-104.

Yamakawa, N., Takahashi, N. and Ohtani, S. 1972. "Forced convection heat and mass transfer under frost conditions." Heat Transfer-Japanese Research, Vol.1, No.2

Yasuda, H., Senshu, T., Kuroda, S., Atsumi, A., and Oguni, K. 1990. "Heat pump performance under frosting conditions. Part 2: Simulation of heat pump cycle characteristics under frosting conditions." ASHRAE Transactions Vol.96, Pt.1

Yonko, J.D. and Sepsy, C.F. 1967. "An investigation of the thermal conductivity of frost while forming on a flat horizontal plate." ASHRAE Transactions, Vol.73, Pt.2

Appendix A

DESIGN OF THE TEST PLATE, HEAT-FLUX METER, AND COLD HEAT EXCHANGER BLOCK

In this appendix, problems concerning the design of the aqueous-glycol cooled heat exchanger block, heat-flux meter and flat plate test surface are discussed. These components are shown in cross section in Figure A.1. The purpose of heat exchanger cold block was to achieve a uniform cold temperature, range -30 ^{o}C to 0 ^{o}C, over the entire top surface of the block while heat was transferred primarily from air passing over the top surface. Temperature variance in the top surface were to be less than 0.1 ^{o}C at the maximum heat flux (500 W/m^2).

Aluminium was selected for the cold block heat exchanger due to its high thermal conductivity, good machinability and low cost. Aqueous-glycol, cooled to sub-freezing temperatures was pumped through a serpentine tube path, machined into the heat exchanger block and as shown in Figure A.2. The size and spacing of this tube path had to be selected to result in a aqueous-glycol temperature rise of less than 1 ^{o}C from inlet to outlet.

To estimate the temperature distribution in the heat exchanger block, steady-state two-dimensional heat conduction theory was used assuming that the parallel machined

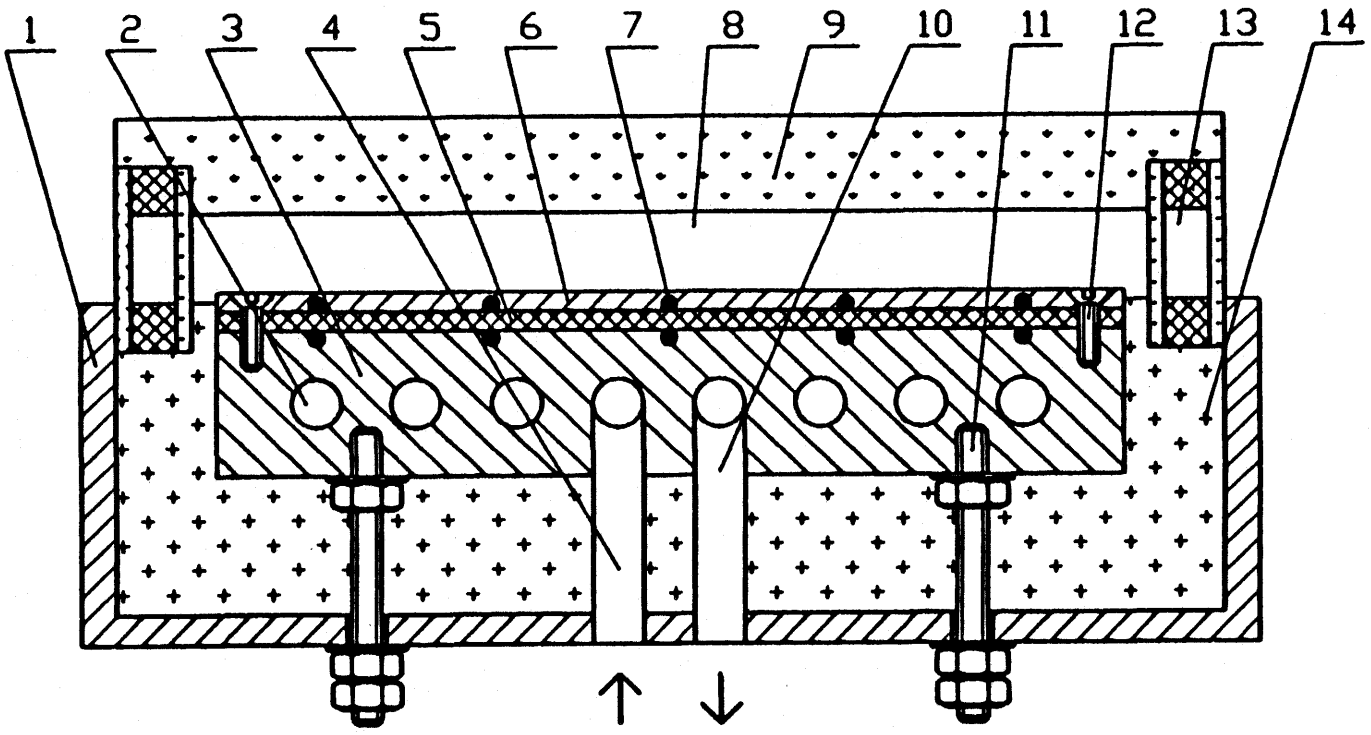

1, Aluminum Frame
2, Aqueous Glycol Coolant Passage
3, Aluminum Cooling Block
4, Coolant Inlet
5, Polyethylene Thermal Resistance Sheet
6, Aluminum Test Surface
7, Thermocouple Pair
8, Airflow Channel
9, Acrylic Plastic Cover Plate
10, Coolant Outlet
11, Nylon Bolt
12, Nylon Bolt
13, Glass Dual Paned Window
14, Extruded Polystyrene

Figure A.1 A cross section profile of the test section

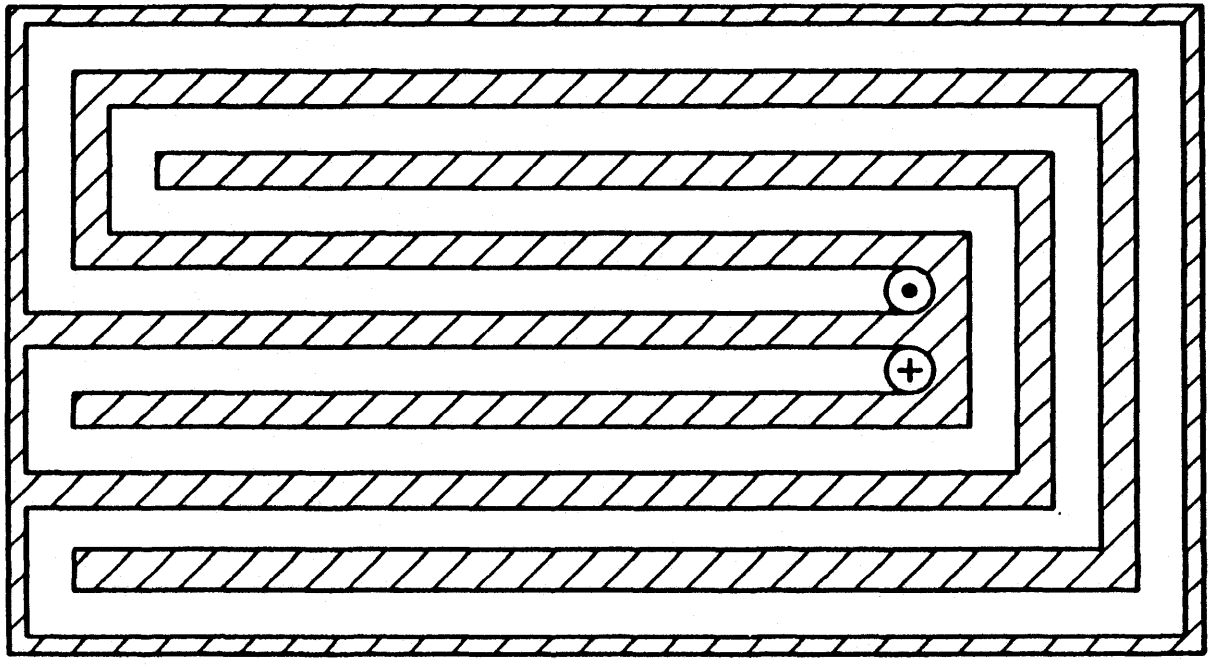

Figure A.2 A schematic plan view of the cold aluminum block showing the flow path of the aqueous glycol coolant

tubes in the cold aluminium block could be replaced by an equal number of heat sinks. Heat transfer from the block to the glycol was estimated using standard tube heat convection correlations.

A question that could not be answered in this preliminary design phase was, how low a temperature could a 50% concentration aqueous-glycol coolant be pumped without over loading the pump? That is, as the temperature of the aqueous-glycol mixture is lowered in the environmental chamber its viscosity increases dramatically resulting in a corresponding increase in the flow resistance of the circuit and decrease in pump efficiency. Since the performance curves for commercial pumps do not cover operating conditions similar to those considered for this experiment, only after construction operational tests could fix the lowest aqueous-glycol temperature that a selected pump could maintain.

The design of the heat-flux meter and top test plate involved additional trade-offs. The material used for the heat-flux meter must have a much lower thermal conductivity than aluminium and this thermal conductivity should be constant or nearly constant over the temperature range of operation for the heat-flux meter. The thickness of the heat-flux meter had to be selected so that errors in the measurement of heat-flux would be small over the typical range of operation but the resistance to heat flux created by the heat-flux meter itself should be as small as practical so that, for a given cold heat exchanger block temperature, the top test plate temperature would be as low as practical. These two opposing requirements suggested a careful design analysis. The top test plate should be selected with a material of high conductivity to reduce any lateral temperature differences. This top test plate also had to accommodate the removable disks, described

in Chapter 4, that are used to measure the mass concentration at various points on the test plate. If the heat flux, resulting from heat convection and frost accumulation due to the airflow boundary layer, varied with distance from the leading edge then the top plate had to be as thin as practical, if the local heat flux was to be measured with the heat-flux meter. Finally, the top plate surface had to be smooth and horizontal without large elastic deformations that might result from any edge clamping schemes. Thus the design of the top plate involved several design trade-offs and again a careful analysis of the heat transfer characteristics was indicated.

For the same reasons as the heat exchanger block, aluminium was selected for the top test plate. Selecting a material for the heat-flux meter was much more difficult due to the lack of heat conduction coefficient information from the manufacturers of possible materials. Finally, a high density polyethylene sheet material was selected for the heat-flux meter.

To analysis the expected temperature distribution in the aluminium test plate and the polyethylene heat-flux meter a two dimensional finite difference model was developed. This model could be used to investigate the temperature distribution in the axial air-flow direction (i.e. as a function of distance from the leading edge) or the lateral direction perpendicular to the airflow direction. The later temperature distribution could be used to select the width of the test plate to reduce the edge effect heat flux and temperature errors to a negligible amount. The geometric model and the boundary conditions selected for investigation are shown in Figure A.3. In this model the cold heat exchanger block is assumed to be at a uniform known temperature. The polyethylene heat-flux meter sheet is placed centrally on top of this heat exchanger block and the aluminium test plate is on the

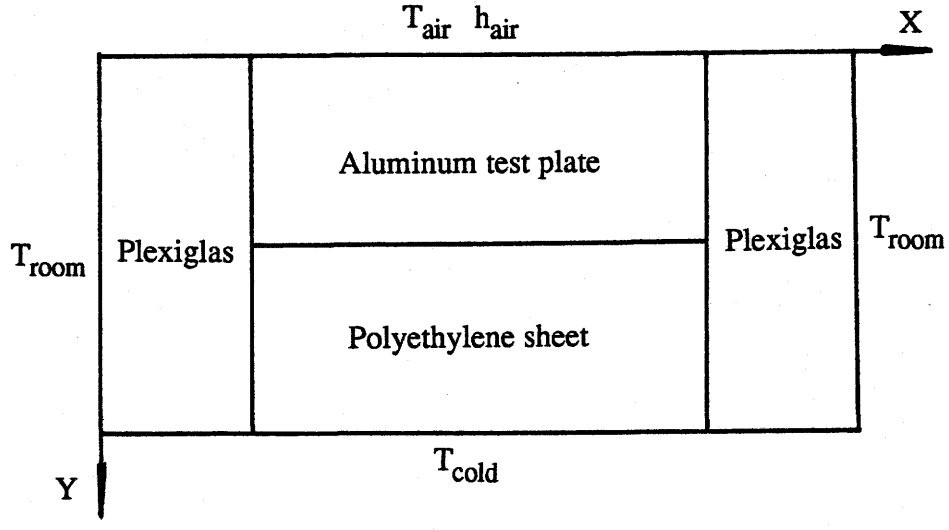

Figure A.3 Schematic diagram of simulation model

top. At either end of these plates, a plexiglas bar was selected for its low thermal conductivity and good machinability.

The heat conduction problem was formulated using the two-dimensional heat conduction equation

$$\rho c \frac{\partial T}{\partial t} = \frac{\partial}{\partial x}(k\frac{\partial T}{\partial x}) + \frac{\partial}{\partial y}(k\frac{\partial T}{\partial y}) \qquad (A.1)$$

where ρ is density, c is heat capacity, and k is thermal conductivity of material. Eq. (A.1) is put into the discrete form of a linear algebraic equation using a fully implicit

discretization scheme (Patanker, 1980). A typical internal control volume is shown in Figure A.4. In the formulation, the thermal properties and the distances between the

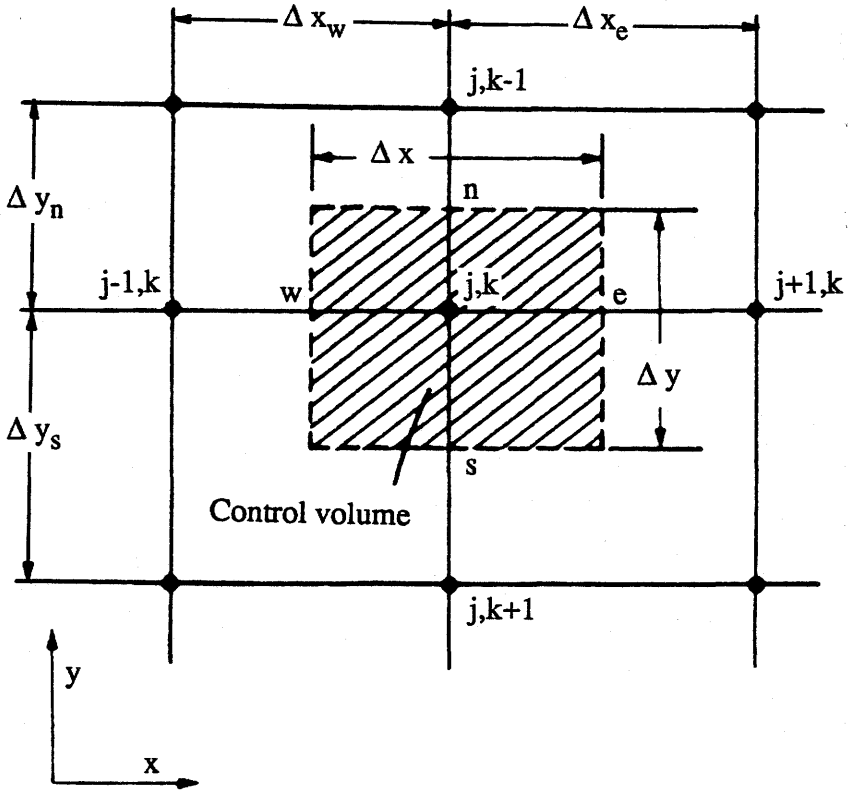

Figure A.4 Schematic diagram of control volume

elemental nodes are not necessary equal. This feature makes the discretization very simple for those plates having different thickness and different materials.

Eq. (A.1) written in the fully implicit scheme for temperature at the j,kth grid point is

$$B_{j,k}T_{j,k-1}+D_{j,k}T_{j-1,k}+E_{j,k}T_{j,k}+F_{j,k}T_{j+1,k}+H_{j,k}T_{j,k+1}=q_{j,k} \qquad (A.2)$$

where $B_{j,k}$; $D_{j,k}$; $E_{j,k}$; $F_{j,k}$; and $H_{j,k}$ are coefficients which can be calculated from the thermal properties, k_w, k_e, k_n, k_s, and from the dimensions of the elements, Δx_w, Δx_e, Δy_n, and Δy_s (Figure A.4). The thermal capacitance effect constant, $q_{j,k}$, is computed from the temperature at the last time step (Patanker, 1980).

Summarising all grid points yields a matrix equation:

$$[A][T]=[q] \qquad (A.3)$$

and the expression of simultaneous equations in matrix notation is shown in Figure A.5.

The solution to equation (A.3) was obtained directly by the standard Gaussian-elimination method using the IMSL (math/library) available from University of Saskatchewan.

A typical steady state simulation temperature distribution profile is shown as a three dimensional plot in Figure A.6 for the case of heat conduction perpendicular to the direction of airflow. For this case the temperature difference across the aluminium test plate is 0.01 ^{o}C and across the polyethylene heat-flux meter is 7.1 ^{o}C. The temperature drop on the plexiglas bar is 27.4 ^{o}C, which implies that the heat transfer from environment to the test plate through the plexiglas is small. The temperature distribution on both edges of the test plate is slightly higher than middle. The variation in temperature between the edges and center of the test plate is 0.6 ^{o}C. This is caused by the heat flux from the environment to the test surface through plexiglas bar.

A typical result for heat conduction along the test plate and heat-flux meter in the

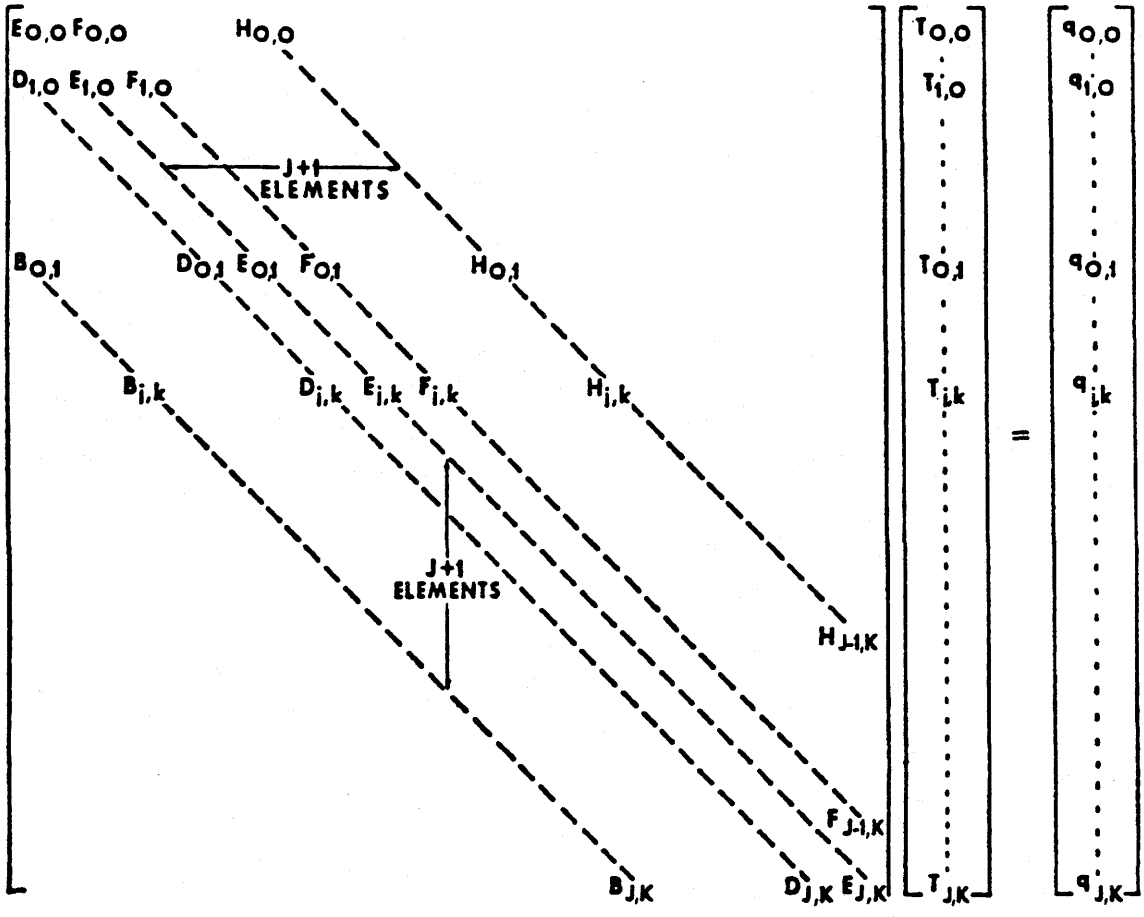

Figure A.5 The expression of simultaneous equations in matrix notation

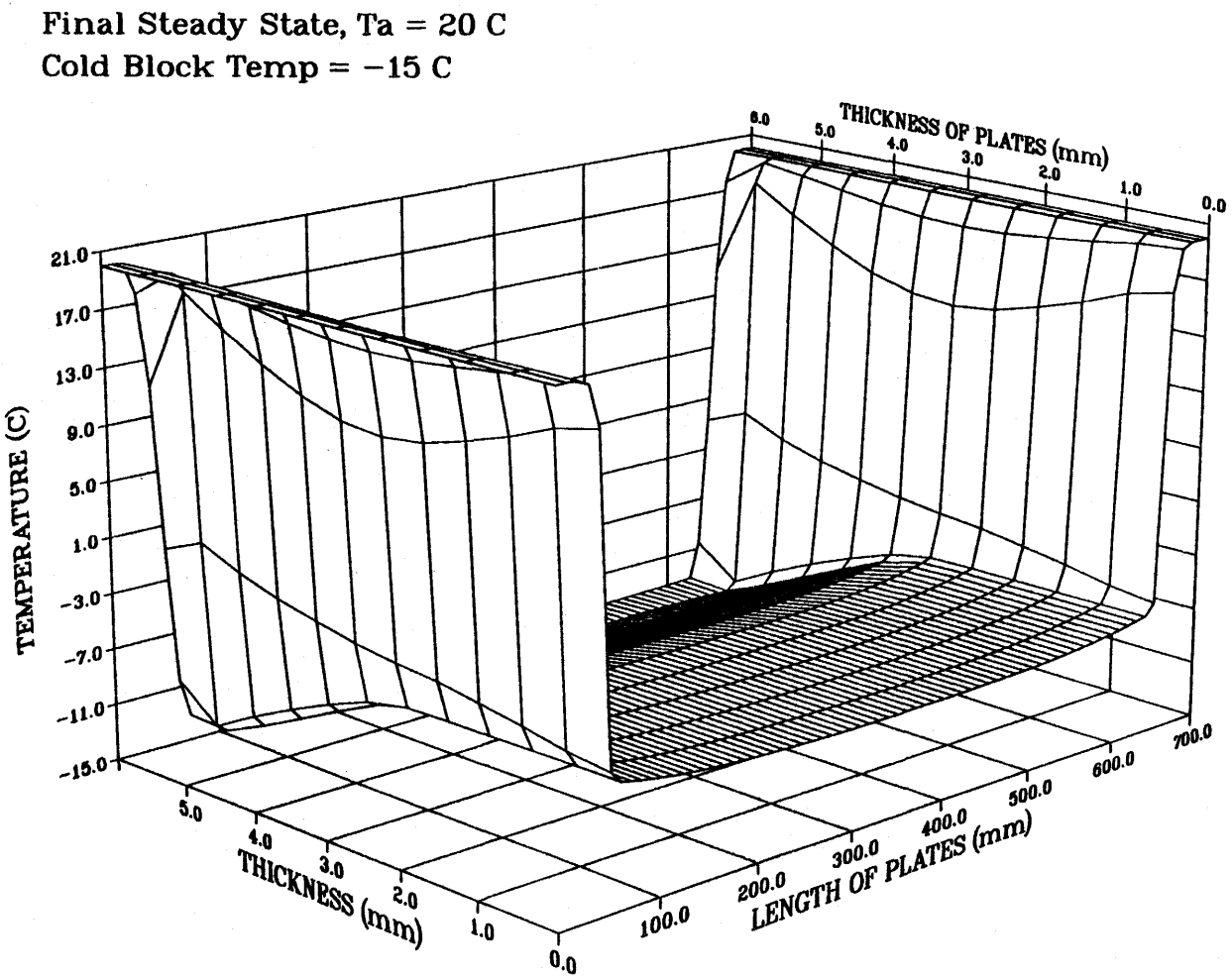

Figure A.6 Temperature distribution of simulation

direction of airflow is shown in Figure A.7. In this figure, the prediction is compared to the corresponding measured temperature distribution on the test surface. (It should be noted that the simulation predictions alone were used for the design.) The difference between the measured and simulated temperature profiles is less than 3 ^{o}C while the simulated temperature difference across the heat-flux meter is 6 ^{o}C. The temperature at the front edge of plate is 1.5 ^{o}C higher than the center. The differences between the measured and simulated temperatures are due to three reasons: (1), the test surface is assumed to be exposed to the airflow boundary layer without frosting in the simulation; however, for the measured data, a frost layer covered the test plate. The frost layer deposit on the test surface acts as a heat transfer resistor reducing the temperature of the test surface; (2), the actual local heat transfer coefficient for convection decreases from the leading edge, which means that the warm air heat flux is larger near the leading edge than downstream. In the simulation, the heat transfer coefficient was assumed as a constant over the entire test surface in simulation; and (3), the thermal conductivity value of polyethylene in the simulation was selected from the limited data in the literature (see Appendix B for the actual value).

The design studies included a number of parameter sensitivity investigations for the heat convection coefficient on the top surface and the thermal resistance of the heat-flux meter; but the most important unknowns were the thickness of the top plate and heat-flux meter. It was concluded from these sensitivity studies that the top aluminium test plate and polyethylene heat-flux meter should both be close to 3 mm in thickness. The final thicknesses selected were 3.00 mm and 3.25 mm for the aluminium test plate and polyethylene heat-flux meter respectively.

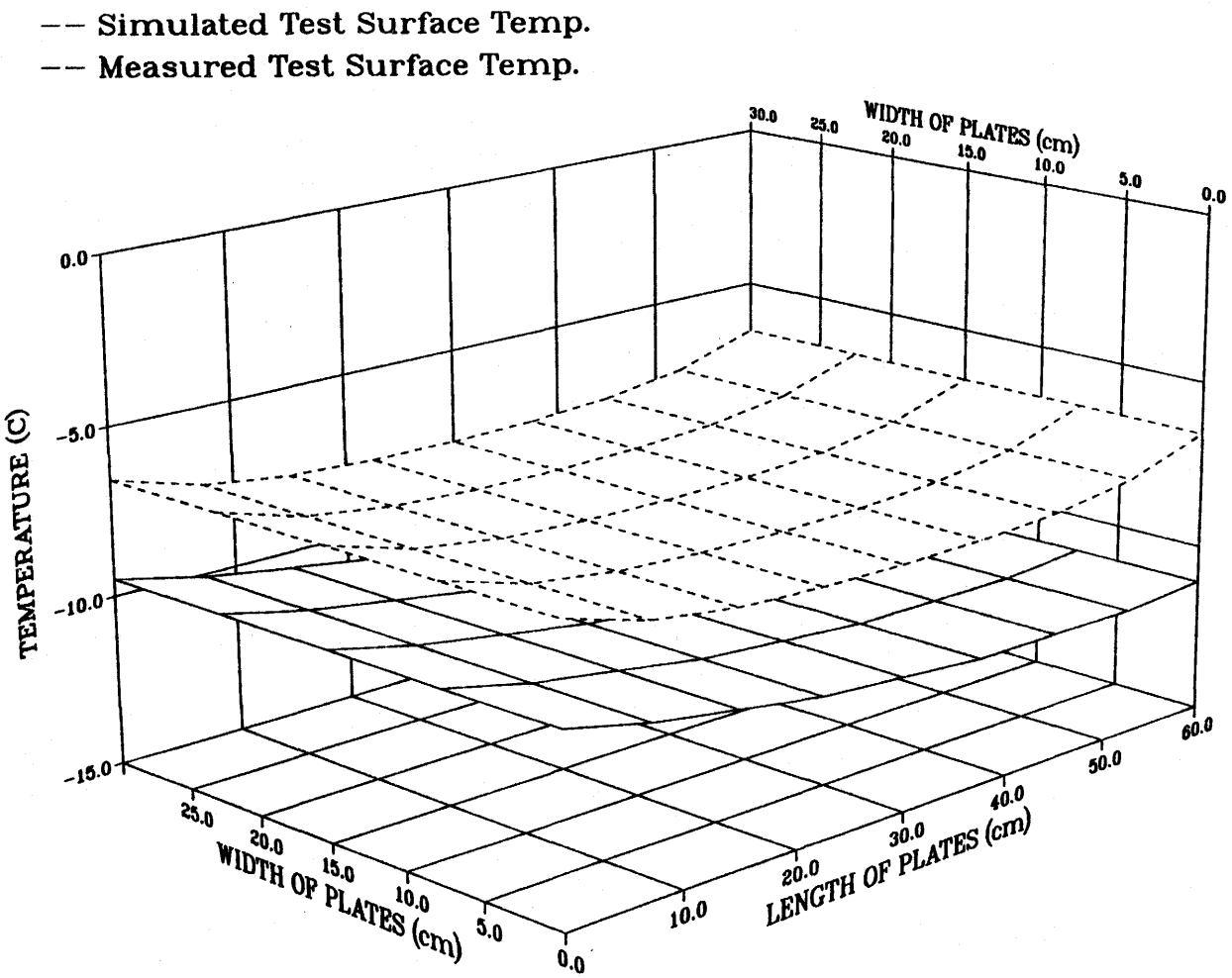

Figure A.7 Comparison of measured and simulated test surface temperature

Appendix B

CALIBRATION OF THE HEAT-FLUX METER

As mentioned in Chapter 3 and Appendix A, the heat-flux meter shown in Figure B.1 and used in the frost measurement apparatus, is composed of a polyethylene sheet between opposing pairs of thermocouples in the aluminium test plate and the aluminium heat exchanger block. The polyethylene sheet is sandwiched between the cold heat exchanger block and the test plate. Any air gaps between the aluminium and polyethylene were filled by first covering both sides of the polyethylene sheet with a thin layer of thermal paste before the aluminium test plate is clamped on top using 5 nylon screws on either side of the test plate. In experiments on frost growth rate, the top aluminium plate will have frost deposited on its surface while heat is transferred to the test plate and through the polyethylene sheet. The heat flux through the frost layer is expected to satisfy the equation

$$q'' = S \cdot \Delta T \qquad (B.1)$$

where Δ T is the average temperature difference across the polyethylene sheet, obtained from the thermocouple readings and S ($W/m^2 \cdot K$) is the thermal conductance of the heat-flux meter. S is expected to be a function of the average temperature of the polyethylene sheet.

The object of this study is to measure the value of S using a calibrated heat flow transducer.

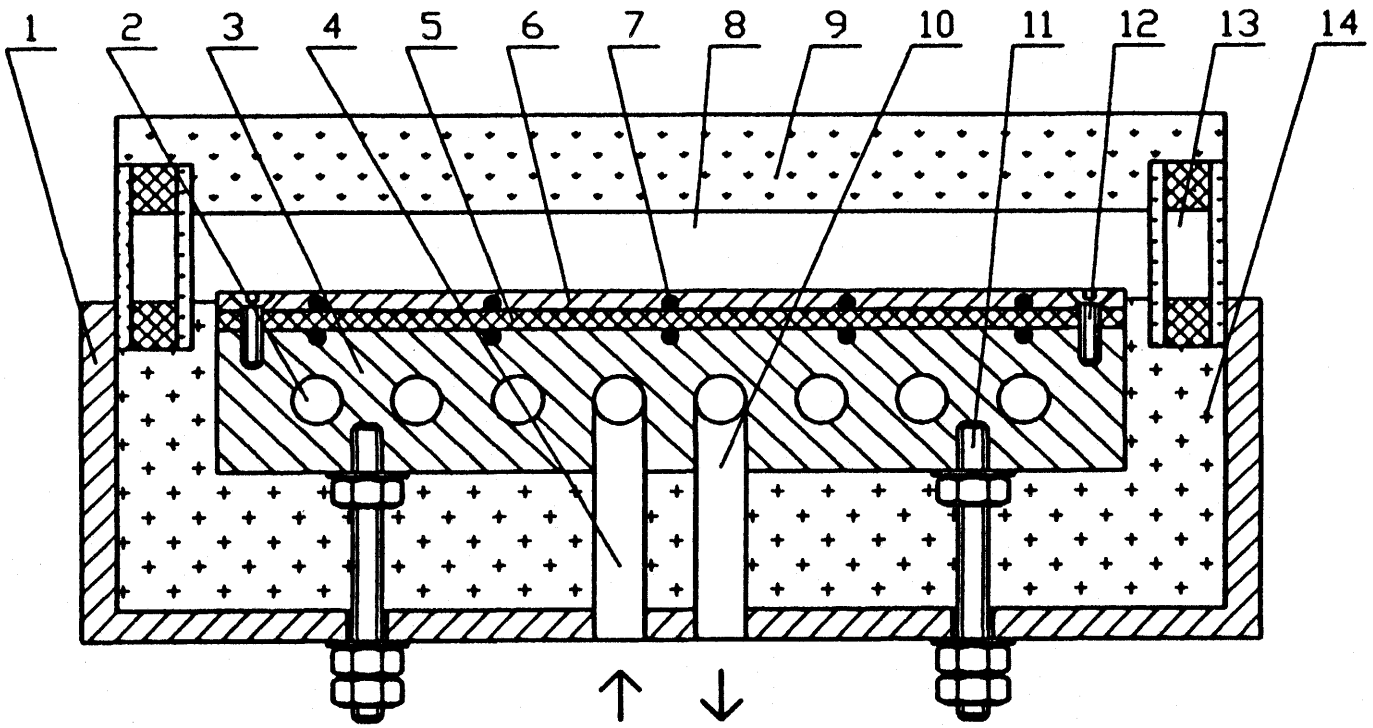

1, Aluminum Frame
2, Aqueous Glycol Coolant Passage
3, Aluminum Cooling Block
4, Coolant Inlet
5, Polyethylene Thermal Resistance Sheet
6, Aluminum Test Surface
7, Thermocouple Pair
8, Airflow Channel
9, Acrylic Plastic Cover Plate
10, Coolant Outlet
11, Nylon Bolt
12, Nylon Bolt
13, Glass Dual Paned Window
14, Extruded Polystyrene

Figure B.1 A cross section profile of the test section

B.1. Calibration Procedure

Calibration is done *in situ* using a heat flow transducer (4×4×1/8 inch), made of paper phenolic materials. The transducer has a thermal constant of 25.93 $W/m^2 \cdot mV$, which is calibrated at 20 °C using ASTM Standard C518. The correction factors for applications at temperature other than 20 °C are also provided. The transducer was thermally bonded onto the top aluminium test plate of the heat-flux meter using a thermal paste. To minimize any lateral heat flow near the transducer, a plastic sheet with a thermal conductance similar to the heat flow transducer, was cut to cover the entire test sheet surface with a hole to exactly fit the transducer. Another aluminium plate was placed on the top of the transducer and this added plastic sheet to insure a uniform temperature on the top surface of the transducer. All possible air gaps that might exist when the transducer and adjacent plates are in contact, were filled with the thermal paste. A schematic of this test arrangement for calibration of the thermal conductance is shown in Figure B.2.

Once the heat flow through the heat-flux meter (to be calibrated) and the heat flow transducer (the calibration element) becomes one-dimensional, i.e., their thermal resistances are in series, the following equation holds

$$q'' = S \cdot \Delta T = VCf \tag{B.2}$$

or

$$S = VCf/\Delta T \tag{B.3}$$

where V is the reading from the transducer (mv), C is the thermal constant of the transducer ($W/m^2 \cdot mV$), f is the temperature correction factor based on the average temperature of the transducer, and Δ T is the temperature difference obtained from the readings of the thermocouples of the heat-flux meter.

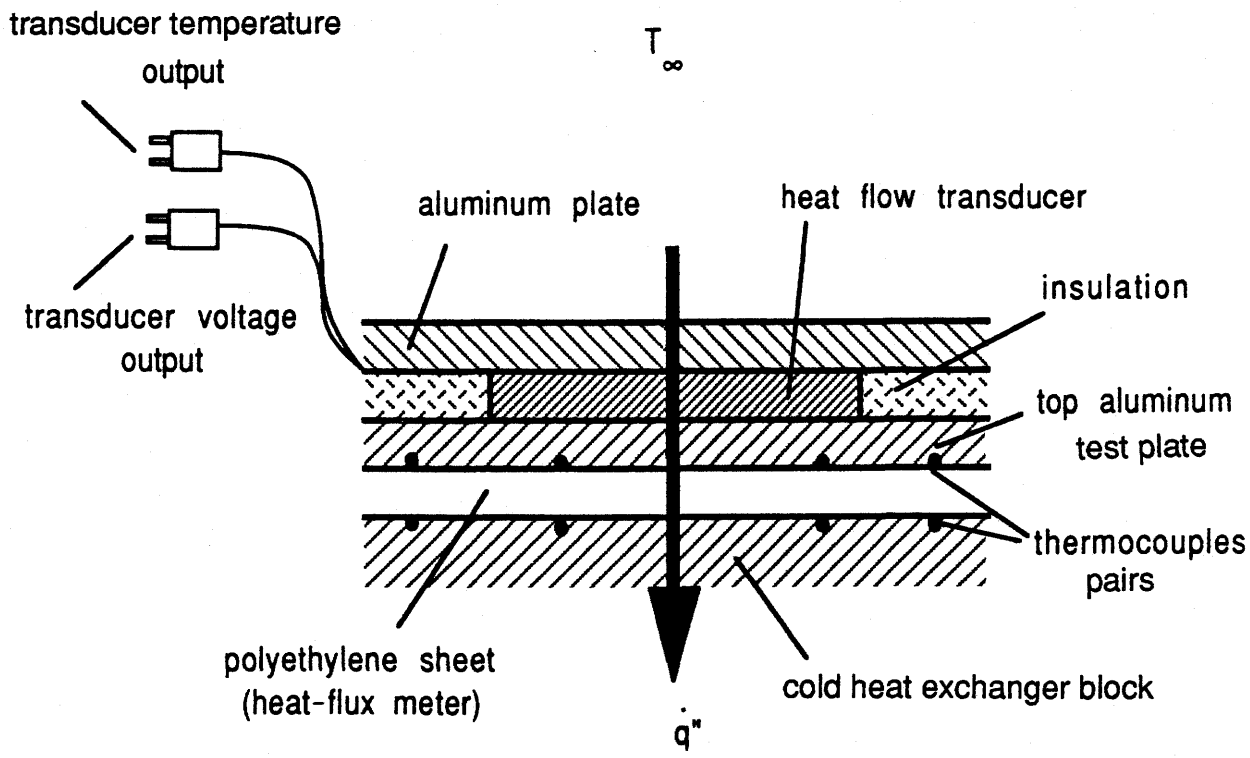

Figure B.2 A schematic of the surface transducer arrangement for calibration of the heat flux meter

Calibration was done at different cold plate temperature (-27 °C to 0 °C) with the transducer placed in the middle of the heat-flux meter top plate, upstream (20 mm from the leading edge) or downstream (30 mm from the trailing edge). The ambient air was kept quiescent at room temperature. The results are shown in Figure B.3 and the data is also tabulated in Table B.1. The thermal conductivity of the polyethylene heat-flux meter sheet can be calculated using the equation

$$k = SH \qquad (B.4)$$

where H is the average thickness of the polyethylene sheet (3.25 mm).

Table B.1 Calibration test data

X*	Test No	Poly. sheet Average Temp. T °C	Transducer Ave.Temp. °C	Transducer Correction Factor *f*	Transducer ΔT °C	V mV	S** W/m^2·K
C	1	0.35	1.24	1.025	0.61	0.94	43.46
	2	-2.13	-1.61	1.04	0.57	0.969	45.84
	3	-3.54	-2.26	1.04	0.71	1.234	46.93
	4	-5.93	-5.25	1.06	0.66	1.135	47.62
	5	-8.01	-6.24	1.05	0.90	1.678	50.71
	6	-9.12	-8.14	1.06	0.90	1.519	46.61
	7	-11.81	-9.67	1.06	1.04	1.921	50.71
	8	-14.72	-13.26	1.08	1.08	2.029	52.86
D	9	-0.70	-0.21	1.03	0.62	1.081	46.52
	10	-4.05	-3.67	1.05	0.71	1.256	48.16
	11	-4.43	-3.84	1.05	0.76	1.335	47.82
	12	-5.90	-5.44	1.06	0.88	1.481	45.99
	13	-6.30	-5.73	1.06	0.76	1.297	47.21
	14	-8.68	-8.18	1.065	0.88	1.584	49.48
	15	-10.71	-9.94	1.07	1.11	2.159	53.91
	16	-13.09	-12.04	1.08	1.19	2.28	53.96
	17	-15.76	-14.53	1.085	1.40	2.766	55.58
	18	-16.55	-15.34	1.085	1.53	2.884	52.92
	19	-20.20	-18.76	1.09	1.68	3.256	54.77
U	20	-0.66	-0.33	1.03	0.59	0.966	43.73
	21	-2.06	-1.76	1.04	0.62	1.003	43.98
	22	-4.40	-4.02	1.05	0.69	1.137	44.86
	23	-6.30	-5.87	1.06	0.75	1.251	45.66
	24	-7.79	-7.29	1.06	0.81	1.362	46.79
	25	-8.98	-8.38	1.065	1.06	1.983	51.76
	26	-11.75	-10.75	1.075	1.26	2.422	53.62
	27	-15.23	-14.41	1.085	1.24	2.201	49.81
	28	-17.98	-17.01	1.085	1.35	2.508	52.30
	29	-18.10	-17.25	1.09	1.38	2.617	53.56

* Transducer Position on the aluminium test plate: C=Center; D=Downstream (30 mm from trailing edge); and U=Upstream (20 mm from leading edge).

** Transducer Thermal Constant = 25.93 W/m^2·mV

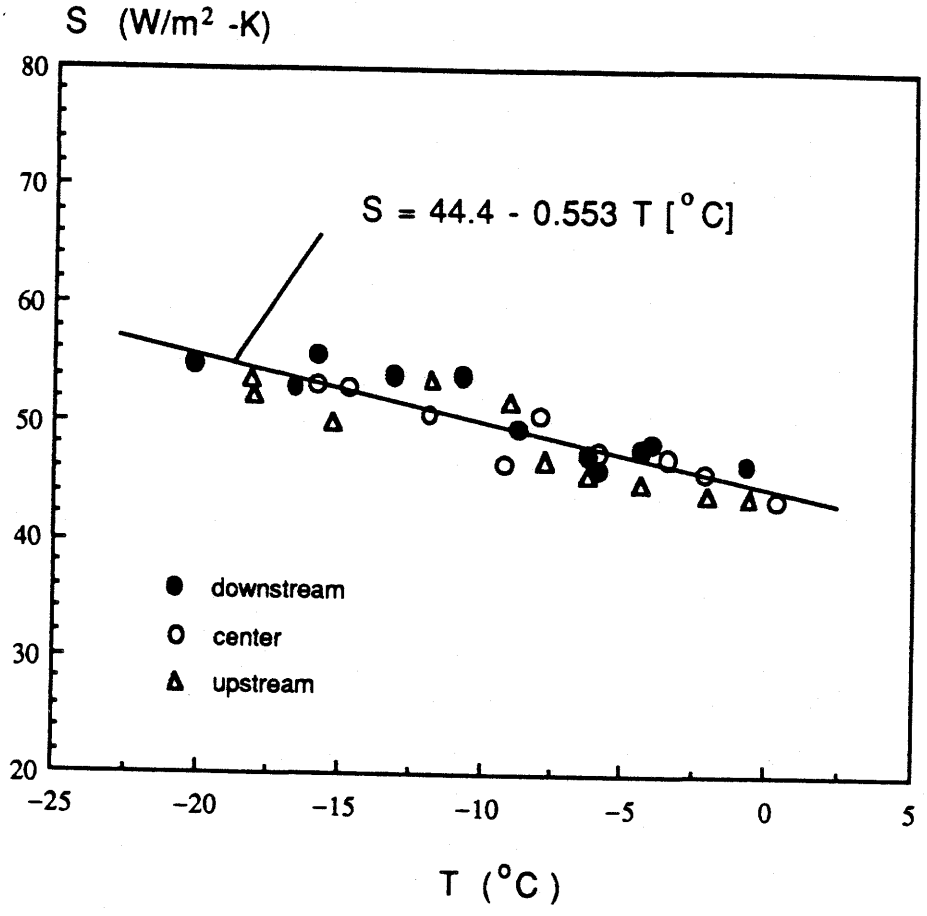

Figure B.3 Thermal conductance of the heat flux meter

B.2. Calibration Results

The advantage of the *in situ* calibration is that the influence of additional thermal resistance in the heat flux meter due to the contact resistance (to the heat flow) of the thermal paste is taken into account. The trend shown in Figure B.3 indicates that the thermal conductance increases as the average temperature decreases. Since there are no

existing data available to evaluate this trend at our calibration temperature range, the thermal conductivity data of polyethylene for the temperature range above 0 °C, reported by Touloukian et al. (1970), are referred here to compare with our data. Figure B.4 shows that our data fall into the range where the curve might be extrapolated. The specimen used for curve 4 has a molecular weight of 21,000 which is close to our specimen with a moderate molecular weight and high density (but not ultra-high molecular weight). The thermal conductivity of our specimen provided by the manufacturer is also shown in Figure B.4, and is consistent with our measured value. The trend that k increases with a decrease in temperature is observed in the reported data (curves 1 and 2), even though these data have different test conditions and are for high molecular weight specimens and a temperature range above 0 °C.

B.3. Uncertainty Analysis

The uncertainty for individual test points may be estimated using the following equation (see Eq. (B.3))

$$(\delta s)^2 = (\delta V/V)^2 + (\delta C/C)^2 + (\delta f/f)^2 + (\delta(\Delta T)/\Delta T)^2 \qquad (B.5)$$

where δC/C and δf/f are about 1%, and δV/V is also estimated as 1% based on the test data. The main source of uncertainty comes from the term δ(Δ T)/Δ T, which could reach 5% for small values of Δ T. Therefore, the maximum uncertainty in S is estimated as ±6%.

The linear curve fit of the calibration data gives the following equation

$$S = 44.4 - 0.553\,T\ [^oC] \qquad (B.6)$$

where T is the average temperature of the polyethylene sheet. Although the linear expression is not the best curve fit (the coefficient of determination R^2=0.78) the above

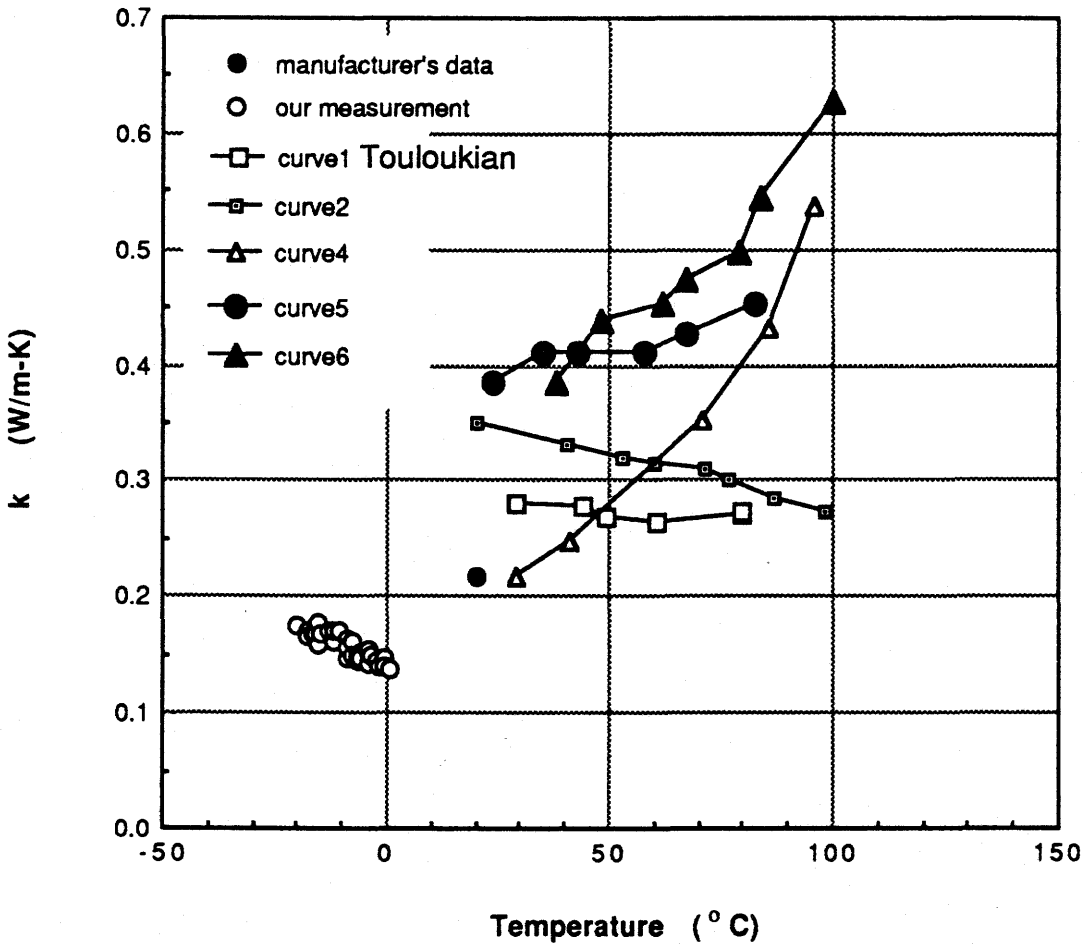

Figure B.4 Comparison of measured thermal conductivity with the data of Touloukian et al. (1970)

simple equation gives a good estimate of the temperature dependence of S, since the standard deviation of the data shown in Figure B.3 is 6% and within the experimental uncertainty.

Appendix C

TEST DATA

The recorded original test data from all the tests is presented in Table C.1.

Table C.1 Recorded Data

No. / t	X (mm)	m_f (kg/m^2)	δ_f (mm)	ρ_f (kg/m^3)	T_s (°C)	T_c (°C)	T_a (°C)	W (kg/kg)	V_a (m/s)
1.1/15	51	0.026	0.36	72.68	-9.9	-14.7	19	0.004	1.53
/15	150	0.024	0.2	103.04	-10.5	-14.7	19	0.004	1.53
/15	227.5	0.02	0.19	107.64	-10.9	-14.7	19	0.004	1.53
/15	303	0.019	0.1	188.6	-11.2	-14.7	19	0.004	1.53
/15	380	0.017	0.22	80.96	-11.3	-14.7	19	0.004	1.53
/15	456	0.017	0.18	98.44	-11.3	-14.7	19	0.004	1.53
/15	530	0.014	0.11	119.6	-11.3	-14.7	19	0.004	1.53
1.2/30	51	0.067	0.71	93.84	-9.9	-14.7	19	0.004	1.53
/30	150	0.051	0.46	110.4	-10.5	-14.7	19	0.004	1.53
/30	227.5	0.052	0.58	90.16	-10.9	-14.7	19	0.004	1.53
/30	303	0.044	0.33	131.56	-11.2	-14.7	19	0.004	1.53
/30	380	0.042	0.45	94.76	-11.3	-14.7	19	0.004	1.53
/30	456	0.041	0.28	147.2	-11.3	-14.7	19	0.004	1.53
/30	530	0.041	0.19	215.28	-11.3	-14.7	19	0.004	1.53

No.= Test number
X = Position on test plate
δ_f = Frost thickness
T_s = Test surface temperature
T_a = Air temperature
V_a = Air velocity
t = Time (min.)
m_f = Frost mass concentration
ρ_f = Frost density
T_c = Cold block temperature
W = Humidity ratio

No. / t	X (mm)	m_f (kg/m^2)	δ_f (mm)	ρ_f (kg/m^3)	T_s (°C)	T_c (°C)	T_a (°C)	W (kg/kg)	V_a (m/s)
1.3/45	51	0.09	0.81	111.32	-10.0	-14.9	18.4	0.004	1.53
/45	150	0.07	0.58	118.68	-10.7	-14.9	18.4	0.004	1.53
/45	227.5	0.062	0.66	93.84	-11.1	-14.9	18.4	0.004	1.53
/45	303	0.056	0.51	110.4	-11.4	-14.9	18.4	0.004	1.53
/45	380	0.052	0.65	80.04	-11.5	-14.9	18.4	0.004	1.53
/45	456	0.052	0.46	114.08	-11.6	-14.9	18.4	0.004	1.53
/45	530	0.05	0.44	113.16	-11.5	-14.9	18.4	0.004	1.53
1.4/60	51	0.116	0.94	123.28	-10.0	-14.9	18.4	0.004	1.53
/60	150	0.095	0.75	126.04	-10.7	-14.9	18.4	0.004	1.53
/60	227.5	0.088	0.81	108.56	-11.1	-14.9	18.4	0.004	1.53
/60	303	0.078	0.64	122.36	-11.4	-14.9	18.4	0.004	1.53
/60	380	0.077	0.81	94.76	-11.5	-14.9	18.4	0.004	1.53
/60	456	0.075	0.58	127.88	-11.6	-14.9	18.4	0.004	1.53
/60	530	0.075	0.55	137.08	-11.5	-14.9	18.4	0.004	1.53
1.5/75	51	0.137	1.02	134.32	-9.5	-14.5	18.8	0.004	1.53
/75	150	0.097	0.95	102.12	-10.2	-14.5	18.8	0.004	1.53
/75	227.5	0.091	0.88	103.04	-10.7	-14.5	18.8	0.004	1.53
/75	303	0.085	0.83	102.12	-11.0	-14.5	18.8	0.004	1.53
/75	380	0.078	0.85	92.00	-11.2	-14.5	18.8	0.004	1.53
/75	456	0.076	0.66	115.00	-11.2	-14.5	18.8	0.004	1.53
/75	530	0.073	0.58	126.96	-11.2	-14.5	18.8	0.004	1.53
1.6/90	51	0.162	1.04	156.4	-9.5	-14.5	18.8	0.004	1.53
/90	150	0.127	1.04	122.36	-10.2	-14.5	18.8	0.004	1.53
/90	227.5	0.117	0.94	124.2	-10.7	-14.5	18.8	0.004	1.53
/90	303	0.108	1.03	104.88	-11.0	-14.5	18.8	0.004	1.53
/90	380	0.1	1.0	100.28	-11.2	-14.5	18.8	0.004	1.53
/90	456	0.096	0.81	117.76	-11.2	-14.5	18.8	0.004	1.53
/90	530	0.097	0.71	137.08	-11.2	-14.5	18.8	0.004	1.53

No. / t	X (mm)	m_f (kg/m^2)	δ_f (mm)	ρ_f (kg/m^3)	T_s (°C)	T_c (°C)	T_a (°C)	W (kg/kg)	V_a (m/s)
1.7/105	51	0.211	1.23	172.04	-9.4	-14.4	20.8	0.004	1.53
/105	150	0.16	1.22	131.56	-10.1	-14.4	20.8	0.004	1.53
/105	227.5	0.138	1.22	113.16	-10.6	-14.4	20.8	0.004	1.53
/105	303	0.127	1.16	108.56	-10.9	-14.4	20.8	0.004	1.53
/105	380	0.121	1.14	105.8	-11.1	-14.4	20.8	0.004	1.53
/105	456	0.113	0.93	122.36	-11.2	-14.4	20.8	0.004	1.53
/105	530	0.107	0.89	119.6	-11.2	-14.4	20.8	0.004	1.53
1.8/120	51	0.234	1.33	175.72	-9.4	-14.4	20.8	0.004	1.53
/120	150	0.187	1.36	137.08	-10.1	-14.4	20.8	0.004	1.53
/120	227.5	0.172	1.37	125.12	-10.6	-14.4	20.8	0.004	1.53
/120	303	0.152	1.3	116.84	-10.9	-14.4	20.8	0.004	1.53
/120	380	0.142	1.24	114.08	-11.1	-14.4	20.8	0.004	1.53
/120	456	0.134	1.07	126.04	-11.2	-14.4	20.8	0.004	1.53
/120	530	0.134	1.07	126.04	-11.2	-14.4	20.8	0.004	1.53
2.1/15	51	0.066	0.74	89.24	-5.6	-10.1	17.5	0.007	1.53
/15	150	0.05	0.56	89.24	-6.1	-10.1	17.5	0.007	1.53
/15	227.5	0.046	0.75	59.8	-6.4	-10.1	17.5	0.007	1.53
/15	303	0.045	0.71	62.56	-6.7	-10.1	17.5	0.007	1.53
/15	380	0.041	0.83	48.76	-6.8	-10.1	17.5	0.007	1.53
/15	456	0.04	0.8	49.68	-6.9	-10.1	17.5	0.007	1.53
/15	530	0.04	0.77	52.44	-6.8	-10.1	17.5	0.007	1.53
2.2/30	51	0.117	1.09	106.72	-5.6	-10.1	17.5	0.007	1.53
/30	150	0.097	0.9	107.64	-6.1	-10.1	17.5	0.0073	1.53
/30	227.5	0.09	1.26	69.92	-6.4	-10.1	17.5	0.007	1.53
/30	303	0.081	0.94	85.56	-6.7	-10.1	17.5	0.007	1.53
/30	380	0.081	1.02	79.12	-6.8	-10.1	17.5	0.007	1.53
/30	456	0.077	0.85	90.16	-6.9	-10.1	17.5	0.007	1.53
/30	530	0.076	0.98	77.28	-6.8	-10.1	17.5	0.007	1.53

No. / t	X (mm)	m_f (kg/m^2)	δ_f (mm)	ρ_f (kg/m^3)	T_s (°C)	T_c (°C)	T_a (°C)	W (kg/kg)	V_a (m/s)
2.3/45	51	0.15	1.17	129.72	-5.3	-9.9	15.5	0.007	1.53
/45	150	0.119	0.95	126.04	-5.9	-9.9	15.5	0.007	1.53
/45	227.5	0.11	1.04	103.96	-6.2	-9.9	15.5	0.007	1.53
/45	303	0.098	1.03	94.76	-6.5	-9.9	15.5	0.007	1.53
/45	380	0.093	1.18	79.12	-6.6	-9.9	15.5	0.007	1.53
/45	456	0.091	1.21	75.44	-6.7	-9.9	15.5	0.007	1.53
/45	530	0.086	1.05	81.88	-6.6	-9.9	15.5	0.007	1.53
2.4/60	51	0.197	1.32	149.96	-5.3	-9.9	15.5	0.007	1.53
/60	150	0.16	1.17	138	-5.9	-9.9	15.5	0.007	1.53
/60	227.5	0.145	1.27	115	-6.2	-9.9	15.5	0.007	1.53
/60	303	0.133	1.27	104.88	-6.5	-9.9	15.5	0.007	1.53
/60	380	0.129	1.42	91.08	-6.6	-9.9	15.5	0.007	1.53
/60	456	0.122	1.21	101.2	-6.7	-9.9	15.5	0.007	1.53
/60	530	0.122	1.24	98.44	-6.6	-9.9	15.5	0.007	1.53
2.5/75	51	0.234	1.78	130.64	-4.9	-9.6	15.1	0.007	1.53
/75	150	0.188	1.56	119.6	-5.5	-9.6	15.1	0.007	1.53
/75	227.5	0.162	1.63	99.36	-5.9	-9.6	15.1	0.007	1.53
/75	303	0.153	1.73	88.32	-6.1	-9.6	15.1	0.007	1.53
/75	380	0.144	1.88	77.28	-6.3	-9.6	15.1	0.007	1.53
/75	456	0.142	1.6	89.24	-6.3	-9.6	15.1	0.007	1.53
/75	530	0.137	1.6	75.44	-6.3	-9.6	15.1	0.007	1.53
2.6/90	51	0.279	1.8	154.56	-4.9	-9.6	15.1	0.007	1.53
/90	150	0.235	1.7	138	-5.5	-9.6	15.1	0.007	1.53
/90	227.5	0.216	1.85	116.84	-5.9	-9.6	15.1	0.007	1.53
/90	303	0.203	1.85	110.4	-6.1	-9.6	15.1	0.007	1.53
/90	380	0.192	2.1	91.08	-6.3	-9.6	15.1	0.007	1.53
/90	456	0.187	1.68	111.32	-6.3	-9.6	15.1	0.007	1.53
/90	530	0.187	1.73	107.64	-6.3	-9.6	15.1	0.007	1.53

No. / t	X (mm)	m_f (kg/m^2)	δ_f (mm)	ρ_f (kg/m^3)	T_s (°C)	T_c (°C)	T_a (°C)	W (kg/kg)	V_a (m/s)
2.7/105	51	0.327	2.13	153.64	-5.3	-9.8	14.7	0.007	1.53
/105	150	0.265	2.13	124.2	-5.9	-9.8	14.7	0.007	1.53
/105	227.5	0.233	2.3	101.2	-6.3	-9.8	14.7	0.007	1.53
/105	303	0.213	2.26	93.84	-6.5	-9.8	14.7	0.007	1.53
/105	380	0.2	2.31	87.4	-6.7	-9.8	14.7	0.007	1.53
/105	456	0.192	2.16	89.24	-6.7	-9.8	14.7	0.007	1.53
/105	530	0.19	2.26	80.04	-6.7	-9.8	14.7	0.007	1.53
2.8/120	51	0.369	2.21	167.44	-5.3	-9.8	14.7	0.007	1.53
/120	150	0.305	2.3	133.4	-5.9	-9.8	14.7	0.007	1.53
/120	227.5	0.276	2.49	111.32	-6.3	-9.8	14.7	0.007	1.53
/120	303	0.251	2.46	102.12	-6.5	-9.8	14.7	0.007	1.53
/120	380	0.234	2.64	89.24	-6.7	-9.8	14.7	0.007	1.53
/120	456	0.23	2.29	101.2	-6.7	-9.8	14.7	0.007	1.53
/120	530	0.23	2.35	98.44	-6.7	-9.8	14.7	0.007	1.53
3.1/15	51	0.06	0.71	83.72	-8.4	-14.6	22	0.007	1.53
/15	150	0.05	0.56	89.24	-9.3	-14.6	22.0	0.007	1.53
/15	227.5	0.045	0.58	77.28	-9.9	-14.6	22.0	0.007	1.53
/15	303	0.042	0.64	67.16	-10.2	-14.6	22.0	0.007	1.53
/15	380	0.042	0.67	62.56	-10.4	-14.6	22.0	0.007	1.53
/15	456	0.04	0.56	70.84	-10.4	-14.6	22.0	0.007	1.53
/15	530	0.041	0.56	72.68	-10.3	-14.6	22.0	0.007	1.53
3.2/30	51	0.121	1.17	103.04	-8.4	-14.6	22.0	0.007	1.53
/30	150	0.1	1.00	100.28	-9.3	-14.6	22.0	0.007	1.53
/30	227	0.091	1.09	82.8	-9.9	-14.6	22.0	0.007	1.53
/30	303	0.086	1.13	76.36	-10.2	-14.6	22.0	0.007	1.53
/30	380	0.087	1.17	73.6	-10.4	-14.6	22.0	0.007	1.53
/30	456	0.088	1.14	77.28	-10.4	-14.6	22.0	0.007	1.53
/30	530	0.09	1.07	83.72	-10.3	-14.6	22.0	0.007	1.53

No. / t	X (mm)	m_f (kg/m^2)	δ_f (mm)	ρ_f (kg/m^3)	T_s (°C)	T_c (°C)	T_a (°C)	W (kg/kg)	V_a (m/s)
3.3/45	51	0.169	2.00	84.64	-9.5	-14.6	13.4	0.007	1.53
/45	150	0.134	1.78	76.36	-10.1	-14.6	13.4	0.007	1.53
/45	227.5	0.112	1.97	57.04	-10.5	-14.6	13.4	0.007	1.53
/45	303	0.106	1.77	59.8	-10.8	-14.6	13.4	0.007	1.53
/45	380	0.092	2.01	46.0	-10.9	-14.6	13.4	0.007	1.53
/45	456	0.093	1.75	53.36	-11.0	-14.6	13.4	0.007	1.53
/45	530	0.093	1.52	60.72	-11.0	-14.6	13.4	0.007	1.53
3.4/60	51	0.228	2.2	102.12	-9.5	-14.6	13.4	0.007	1.53
/60	150	0.187	2.16	85.56	-10.1	-14.6	13.4	0.007	1.53
/60	227.5	0.162	2.3	69.92	-10.5	-14.6	13.4	0.007	1.53
/60	303	0.158	2.25	78.2	-10.8	-14.6	13.4	0.007	1.53
/60	380	0.14	2.2	64.4	-10.9	-14.6	13.4	0.007	1.53
/60	456	0.136	1.98	69.0	-11.0	-14.6	13.4	0.007	1.53
/60	530	0.143	1.82	79.12	-11.0	-14.6	13.4	0.007	1.53
3.5/75	51	0.296	2.16	137.08	-8.5	-14.5	22.0	0.007	1.53
/75	150	0.219	2.1	103.96	-9.4	-14.5	22.0	0.007	1.53
/75	227.5	0.2	2.31	87.4	-9.9	-14.5	22.0	0.007	1.53
/75	303	0.186	2.26	82.8	-10.3	-14.5	22.0	0.007	1.53
/75	380	0.188	2.36	80.04	-10.5	-14.5	22.0	0.007	1.53
/75	456	0.164	2.29	71.76	-10.6	-14.5	22.0	0.007	1.53
/75	530	0.171	2.18	79.12	-10.5	-14.5	22.0	0.007	1.53
3.6/90	51	0.323	2.41	134.32	-8.2	-14.3	19.6	0.007	1.53
/90	150	0.267	2.4	111.32	-9.1	-14.3	19.6	0.007	1.53
/90	227.5	0.225	2.37	94.76	-9.7	-14.3	19.6	0.007	1.53
/90	303	0.221	2.41	92.0	-10.1	-14.3	19.6	0.007	1.53
/90	380	0.220	2.51	88.32	-10.4	-14.3	19.6	0.007	1.53
/90	456	0.201	2.33	87.40	-10.4	-14.3	19.6	0.007	1.53
/90	530	0.198	2.41	81.88	-10.4	-14.3	19.6	0.007	1.53

No. / t	X (mm)	m_f (kg/m^2)	δ_f (mm)	ρ_f (kg/m^3)	T_s (°C)	T_c (°C)	T_a (°C)	W (kg/kg)	V_a (m/s)
3.7/105	51	0.384	2.62	147.2	-8.2	-14.3	19.6	0.007	1.53
/105	150	0.309	2.62	117.76	-9.1	-14.3	19.6	0.007	1.53
/105	227.5	0.278	2.72	102.12	-9.7	-14.3	19.6	0.007	1.53
/105	303	0.259	2.65	98.44	-10.1	-14.3	19.6	0.007	1.53
/105	380	0.246	2.69	92.0	-10.4	-14.3	19.6	0.007	1.53
/105	456	0.250	2.57	96.6	-10.4	-14.3	19.6	0.007	1.53
/105	530	0.249	2.64	93.84	-10.4	-14.3	19.6	0.007	1.53
3.8/120	51	0.45	2.83	159.16	-8.4	-14.7	19.0	0.007	1.53
/120	150	0.36	3.02	118.68	-9.3	-14.7	19.0	0.007	1.53
/120	227.5	0.32	3.14	104.88	-9.9	-14.7	19.0	0.007	1.53
/120	303	0.31	3.07	102.12	-10.2	-14.7	19.0	0.007	1.53
/120	380	0.3	3.09	98.44	-10.4	-14.7	19.0	0.007	1.53
/120	456	0.29	3.21	89.24	-10.4	-14.7	19.0	0.007	1.53
/120	530	0.3	2.98	99.36	-10.3	-14.7	19.0	0.007	1.53
4.1/15	51	0.076	1.35	55.20	-13.7	-20.7	18.6	0.007	1.53
/15	150	0.057	1.32	42.32	-15.0	-20.7	18.6	0.007	1.53
/15	227.5	0.044	1.52	29.44	-15.7	-20.7	18.6	0.007	1.53
/15	303	0.041	1.59	25.76	-16.2	-20.7	18.6	0.007	1.53
/15	380	0.044	1.65	25.76	-16.4	-20.7	18.6	0.007	1.53
/15	456	0.039	1.68	23.0	-16.5	-20.7	18.6	0.007	1.53
/15	530	0.037	1.5	24.84	-16.3	-20.7	18.6	0.007	1.53
4.2/30	51	0.139	2.16	65.32	-13.7	-20.7	18.6	0.007	1.53
/30	150	0.109	1.94	56.12	-15.0	-20.7	18.6	0.007	1.53
/30	227.5	0.095	2.07	46.0	-15.7	-20.7	18.6	0.007	1.53
/30	303	0.088	2.15	41.4	-16.2	-20.7	18.6	0.007	1.53
/30	380	0.085	2.26	36.8	-16.4	-20.7	18.6	0.007	1.53
/30	456	0.085	2.16	38.64	-16.5	-20.7	18.6	0.007	1.53
/30	530	0.09	2.00	45.08	-16.3	-20.7	18.6	0.007	1.53

No. / t	X (mm)	m_f (kg/m^2)	δ_f (mm)	ρ_f (kg/m^3)	T_s (°C)	T_c (°C)	T_a (°C)	W (kg/kg)	V_a (m/s)
4.3/45	51	0.182	2.41	75.44	-14.4	-20.5	15.6	0.007	1.53
/45	150	0.137	2.31	58.88	-15.2	-20.5	15.6	0.007	1.53
/45	227.5	0.118	2.5	46.92	-15.7	-20.5	15.6	0.007	1.53
/45	303	0.114	2.48	46.0	-16.0	-20.5	15.6	0.007	1.53
/45	380	0.107	2.54	42.32	-16.2	-20.5	15.6	0.007	1.53
/45	456	0.103	2.31	45.08	-16.2	-20.5	15.6	0.007	1.53
/45	530	0.102	2.39	42.32	-16.1	-20.5	15.6	0.007	1.53
4.4/60	51	0.233	2.79	82.8	-14.4	-20.5	15.6	0.007	1.53
/60	150	0.187	2.72	69.0	-15.2	-20.5	15.6	0.007	1.53
/60	227.5	0.163	2.79	57.96	-15.7	-20.5	15.6	0.007	1.53
/60	303	0.158	2.87	55.2	-16.0	-20.5	15.6	0.007	1.53
/60	380	0.149	2.82	53.36	-16.2	-20.5	15.6	0.007	1.53
/60	456	0.143	2.57	56.12	-16.2	-20.5	15.6	0.007	1.53
/60	530	0.148	2.72	54.28	-16.1	-20.5	15.6	0.007	1.53
4.5/75	51	0.262	2.82	92.92	-14.2	-20.3	15.7	0.007	1.53
/75	150	0.21	2.67	79.12	-15.0	-20.3	15.7	0.007	1.53
/75	227.5	0.174	2.74	64.4	-15.5	-20.3	15.7	0.007	1.53
/75	303	0.167	2.87	57.96	-15.9	-20.3	15.7	0.007	1.53
/75	380	0.169	2.97	57.04	-16.1	-20.3	15.7	0.007	1.53
/75	456	0.158	2.82	56.12	-16.1	-20.3	15.7	0.007	1.53
/75	530	0.148	2.64	56.12	-16.1	-20.3	15.7	0.007	1.53
4.6/90	51	0.338	3.23	104.88	-14.2	-20.3	15.7	0.007	1.53
/90	150	0.264	3.25	80.96	-15.0	-20.3	15.7	0.007	1.53
/90	227.5	0.236	3.33	70.84	-15.5	-20.3	15.7	0.007	1.53
/90	303	0.220	3.29	67.16	-15.9	-20.3	15.7	0.007	1.53
/90	380	0.217	3.38	64.4	-16.1	-20.3	15.7	0.007	1.53
/90	456	0.213	3.1	69.0	-16.1	-20.3	15.7	0.007	1.53
/90	530	0.217	3.1	70.84	-16.1	-20.3	15.7	0.007	1.53

No. / t	X (mm)	m_f (kg/m^2)	δ_f (mm)	ρ_f (kg/m^3)	T_s (°C)	T_c (°C)	T_a (°C)	W (kg/kg)	V_a (m/s)
4.7/105	51	0.4	3.3	121.44	-13.4	-19.4	15.6	0.007	1.53
/105	150	0.295	3.3	89.24	-14.2	-19.4	15.6	0.007	1.53
/105	227.5	0.244	3.53	69.0	-14.7	-19.4	15.6	0.007	1.53
/105	303	0.25	3.64	69.0	-15.0	-19.4	15.6	0.007	1.53
/105	380	0.231	3.68	62.56	-15.2	-19.4	15.6	0.007	1.53
/105	456	0.226	3.61	62.56	-15.3	-19.4	15.6	0.007	1.53
/105	530	0.23	3.28	70.84	-15.2	-19.4	15.6	0.007	1.53
4.8/120	51	0.45	3.6	125.12	-13.4	-19.4	15.6	0.007	1.53
/120	150	0.353	3.7	95.68	-14.2	-19.4	15.6	0.007	1.53
/120	227.5	0.321	3.8	83.72	-14.7	-19.4	15.6	0.007	1.53
/120	303	0.285	3.9	72.68	-15.0	-19.4	15.6	0.007	1.53
/120	380	0.28	3.9	72.68	-15.2	-19.4	15.6	0.007	1.53
/120	456	0.28	3.6	77.28	-15.3	-19.4	15.6	0.007	1.53
/120	530	0.27	3.5	78.2	-15.2	-19.4	15.6	0.007	1.53
5.1/15	51	0.086	1.3	66.24	-9.7	-15.9	21.3	0.010	1.53
/15	150	0.067	1.2	56.12	-10.3	-15.9	21.3	0.010	1.53
/15	227.5	0.058	1.18	49.68	-10.6	-15.9	21.3	0.010	1.53
/15	303	0.055	1.19	46.0	-10.9	-15.9	21.3	0.010	1.53
/15	380	0.053	1.35	40.48	-11.1	-15.9	21.3	0.010	1.53
/15	456	0.05	1.32	37.72	-11.3	-15.9	21.3	0.010	1.53
/15	530	0.05	1.22	41.4	-11.5	-15.9	21.3	0.010	1.53
5.2/30	51	0.21	1.35	156.4	-9.7	-15.9	21.3	0.010	1.53
/30	150	0.174	1.42	123.28	-10.3	-15.9	21.3	0.010	1.53
/30	227.5	0.156	1.56	99.36	-10.6	-15.9	21.3	0.010	1.53
/30	303	0.138	1.63	84.64	-10.9	-15.9	21.3	0.010	1.53
/30	380	0.132	1.76	75.44	-11.1	-15.9	21.3	0.010	1.53
/30	456	0.121	1.75	69.0	-11.3	-15.9	21.3	0.010	1.53
/30	530	0.121	1.78	68.08	-11.5	-15.9	21.3	0.010	1.53

No. / t	X (mm)	m_f (kg/m^2)	δ_f (mm)	ρ_f (kg/m^3)	T_s (°C)	T_c (°C)	T_a (°C)	W (kg/kg)	V_a (m/s)
5.3/45	51	0.410	2.07	197.8	-9.1	-16.0	22.3	0.010	1.53
/45	150	0.35	2.06	170.2	-9.9	-16.0	22.3	0.010	1.53
/45	227.5	0.31	2.15	142.6	-10.5	-16.0	22.3	0.010	1.53
/45	303	0.29	2.24	127.88	-10.9	-16.0	22.3	0.010	1.53
/45	380	0.26	2.41	108.56	-11.4	-16.0	22.3	0.010	1.53
/45	456	0.26	2.37	107.64	-11.7	-16.0	22.3	0.010	1.53
/45	530	0.23	2.36	96.6	-11.9	-16.0	22.3	0.010	1.53
5.4/60	51	0.55	2.82	194.12	-9.1	-16.0	22.3	0.010	1.53
/60	150	0.43	2.77	153.64	-9.9	-16.0	22.3	0.010	1.53
/60	227.5	0.37	2.82	129.72	-10.5	-16.0	22.3	0.010	1.53
/60	303	0.33	2.74	121.44	-10.9	-16.0	22.3	0.010	1.53
/60	380	0.3	2.91	103.04	-11.4	-16.0	22.3	0.010	1.53
/60	456	0.3	2.7	102.12	-11.7	-16.0	22.3	0.010	1.53
/60	530	0.28	2.84	96.6	-11.9	-16.0	22.3	0.010	1.53
6.1/15	51	0.076	1.23	61.64	-10.1	-15.0	23.2	0.0096	1.15
/15	150	0.06	0.97	61.64	-10.5	-15.0	23.2	0.0096	1.15
/15	227.5	0.053	1.11	47.84	-10.7	-15.0	23.2	0.0096	1.15
/15	303	0.049	1.1	44.16	-11.0	-15.0	23.2	0.0096	1.15
/15	380	0.047	1.12	42.32	-11.3	-15.0	23.2	0.0096	1.15
/15	456	0.044	0.98	44.16	-11.5	-15.0	23.2	0.0096	1.15
/15	530	0.041	0.91	45.08	-11.8	-15.0	23.2	0.0096	1.15
6.2/30	51	0.138	1.65	83.72	-10.1	-15.0	23.2	0.0096	1.15
/30	150	0.117	1.4	83.72	-10.5	-15.0	23.2	0.0096	1.15
/30	227.5	0.107	1.5	70.84	-10.7	-15.0	23.2	0.0096	1.15
/30	303	0.1	1.65	59.8	-11.0	-15.0	23.2	0.0096	1.15
/30	380	0.09	1.52	58.88	-11.3	-15.0	23.2	0.0096	1.15
/30	456	0.08	1.45	55.2	-11.5	-15.0	23.2	0.0096	1.15
/30	530	0.083	1.6	52.44	-11.8	-15.0	23.2	0.0096	1.15

No. / t	X (mm)	m_f (kg/m^2)	δ_f (mm)	ρ_f (kg/m^3)	T_s (°C)	T_c (°C)	T_a (°C)	W (kg/kg)	V_a (m/s)
6.3/45	51	0.183	1.98	92.0	-10.4	-15.1	23.4	0.0096	1.15
/45	150	0.146	2.1	69.0	-10.9	-15.1	23.4	0.0096	1.15
/45	227.5	0.128	2.2	57.96	-11.3	-15.1	23.4	0.0096	1.15
/45	303	0.116	2.3	49.68	-11.5	-15.1	23.4	0.0096	1.15
/45	380	0.107	2.4	44.16	-11.7	-15.1	23.4	0.0096	1.15
/45	456	0.1	2.2	44.16	-11.9	-15.1	23.4	0.0096	1.15
/45	530	0.091	2.0	45.08	-11.9	-15.1	23.4	0.0096	1.15
6.4/60	51	0.24	2.37	101.2	-10.4	-15.1	23.4	0.0096	1.15
/60	150	0.19	2.39	80.04	-10.9	-15.1	23.4	0.0096	1.15
/60	227.5	0.167	2.36	70.84	-11.3	-15.1	23.4	0.0096	1.15
/60	303	0.149	2.44	60.72	-11.5	-15.1	23.4	0.0096	1.15
/60	380	0.136	2.41	56.12	-11.7	-15.1	23.4	0.0096	1.15
/60	456	0.126	2.29	55.2	-11.9	-15.1	23.4	0.0096	1.15
/60	530	0.126	2.08	59.8	-11.9	-15.1	23.4	0.0096	1.15
7.1/15	51	0.1	0.85	116.84	-9.6	-16.2	16.8	0.0065	2.67
/15	150	0.086	0.81	105.8	-9.8	-16.2	16.8	0.0065	2.67
/15	227.5	0.08	0.81	98.44	-9.9	-16.2	16.8	0.0065	2.67
/15	303	0.075	0.74	101.2	-10.1	-16.2	16.8	0.0065	2.67
/15	380	0.071	0.74	95.68	-10.2	-16.2	16.8	0.0065	2.67
/15	456	0.067	0.7	95.68	-10.4	-16.2	16.8	0.0065	2.67
/15	530	0.063	0.81	78.2	-10.5	-16.2	16.8	0.0065	2.67
7.2/30	51	0.168	1.3	128.8	-9.6	-16.2	16.8	0.0065	2.67
/30	150	0.154	1.35	114.08	-9.8	-16.2	16.8	0.0065	2.67
/30	227.5	0.147	1.37	106.72	-9.9	-16.2	16.8	0.0065	2.67
/30	303	0.132	1.3	101.2	-10.1	-16.2	16.8	0.0065	2.67
/30	380	0.133	1.25	105.8	-10.2	-16.2	16.8	0.0065	2.67
/30	456	0.124	1.1	113.16	-10.4	-16.2	16.8	0.0065	2.67
/30	530	0.126	1.37	92.0	-10.5	-16.2	16.8	0.0065	2.67

No. / t	X (mm)	m_f (kg/m^2)	δ_f (mm)	ρ_f (kg/m^3)	T_s (°C)	T_c (°C)	T_a (°C)	W (kg/kg)	V_a (m/s)
7.3/45	51	0.245	1.73	141.68	-9.9	-16.2	18.0	0.0065	2.67
/45	150	0.211	1.74	122.36	-10.1	-16.2	18.0	0.0065	2.67
/45	227.5	0.2	1.79	112.24	-10.3	-16.2	18.0	0.0065	2.67
/45	303	0.189	1.71	111.32	-10.5	-16.2	18.0	0.0065	2.67
/45	380	0.187	1.82	103.04	-10.7	-16.2	18.0	0.0065	2.67
/45	456	0.17	1.74	98.44	-10.8	-16.2	18.0	0.0065	2.67
/45	530	0.169	1.85	91.08	-11.0	-16.2	18.0	0.0065	2.67
7.4/75	51	0.361	2.21	162.84	-9.9	-16.2	18.0	0.0065	2.67
/75	150	0.328	2.22	148.12	-10.1	-16.2	18.0	0.0065	2.67
/75	227.5	0.306	2.3	133.4	-10.3	-16.2	18.0	0.0065	2.67
/75	303	0.3	2.17	138.0	-10.5	-16.2	18.0	0.0065	2.67
/75	380	0.282	2.28	124.2	-10.7	-16.2	18.0	0.0065	2.67
/75	456	0.266	2.1	126.96	-10.8	-16.2	18.0	0.0065	2.67
/75	530	0.264	2.34	113.16	-11.0	-16.2	18.0	0.0065	2.67